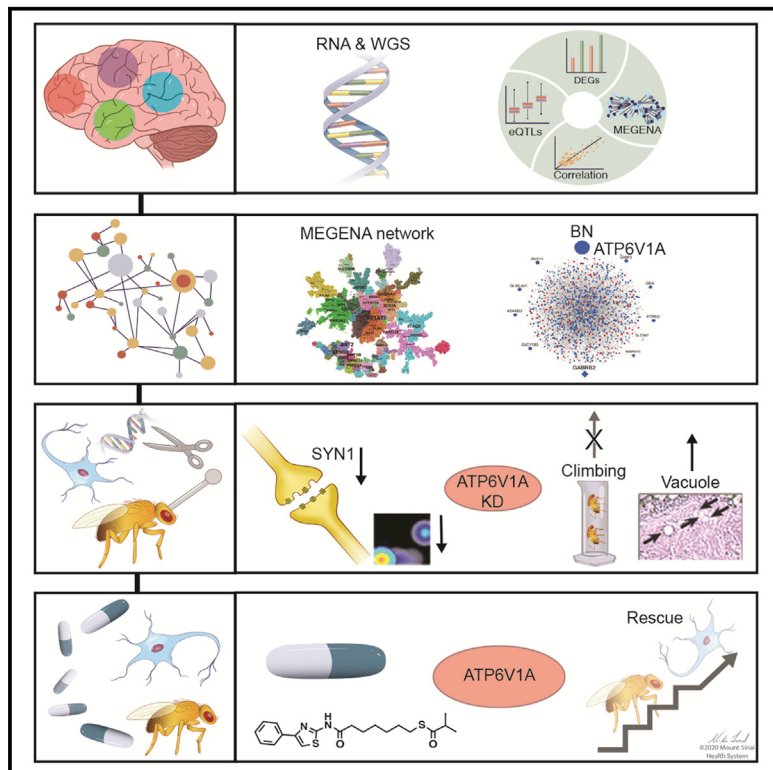


# Transformative Network Modeling of Multi-omics Data Reveals Detailed Circuits, Key Regulators, and Potential Therapeutics for Alzheimer's Disease

## Graphical Abstract



## Authors

Minghui Wang, Aiqun Li,  
Michiko Sekiya, ..., Eric Schadt,  
Kristen J. Brennand, Bin Zhang

## Correspondence

bin.zhang@mssm.edu

## In Brief

Employing an integrative network biology approach, Wang et al. identify critical gene subnetworks associated with late-onset Alzheimer's disease (LOAD) and predict ATP6V1A as a key regulator of a neuron-specific subnetwork most affected by LOAD. ATP6V1A deficit causes neuronal impairment and neurodegeneration, which are normalized by a predicted compound, NCH-51.

## Highlights

- Development of gene network models of four cortical areas affected by LOAD
- Identification of region-specific molecular changes and gene subnetworks in LOAD
- ATP6V1A is a top key regulator of a neuronal subnetwork most disrupted in LOAD
- NCH-51 normalizes neuronal impairment and neurodegeneration caused by *ATP6V1A* deficit



## Article

# Transformative Network Modeling of Multi-omics Data Reveals Detailed Circuits, Key Regulators, and Potential Therapeutics for Alzheimer's Disease

Minghui Wang,<sup>1,2,3,19</sup> Aiqun Li,<sup>1,3,4,5,6,19</sup> Michiko Sekiya,<sup>7,18,19</sup> Noam D. Beckmann,<sup>1,2,19</sup> Xiuming Quan,<sup>7,19</sup> Nadine Schröde,<sup>3,4,5,6</sup> Michael B. Fernando,<sup>3,4,5,6</sup> Alex Yu,<sup>3,4,5,6</sup> Li Zhu,<sup>12,13,16</sup> Jiqing Cao,<sup>12,13,16</sup> Liwei Lyu,<sup>3,4,5,6</sup> Emrin Horgusluoglu,<sup>1,2,3</sup> Qian Wang,<sup>1,2,3</sup> Lei Guo,<sup>1,2,3</sup> Yuan-shuo Wang,<sup>1,2,3</sup> Ryan Neff,<sup>1,2,3</sup> Won-min Song,<sup>1,2,3</sup> Ermeng Wang,<sup>1,2,3</sup> Qi Shen,<sup>1,2,3</sup> Xianxiao Zhou,<sup>1,2,3</sup> Chen Ming,<sup>1,2,3</sup> Seok-Man Ho,<sup>3,4,5,6</sup> Sezen Vatansever,<sup>1,2,3</sup> H. Ümit Kaniskan,<sup>8,9</sup> Jian Jin,<sup>8,9,10</sup> Ming-Ming Zhou,<sup>8</sup> Kanae Ando,<sup>11</sup> Lap Ho,<sup>1,2,3</sup> Paul A. Slesinger,<sup>4,5</sup> Zhenyu Yue,<sup>12</sup> Jun Zhu,<sup>1,3</sup> Pavel Katsel,<sup>6,17</sup> Sam Gandy,<sup>6,12,13</sup> Michelle E. Ehrlich,<sup>12,14</sup> Valentina Fossati,<sup>15</sup> Scott Noggle,<sup>15</sup> Dongming Cai,<sup>12,13,16</sup> Vahram Haroutunian,<sup>4,6,13,17</sup> Koichi M. Iijima,<sup>7,18,20</sup> Eric Schadt,<sup>1,2,20</sup> Kristen J. Brennand,<sup>3,4,5,6,20</sup> and Bin Zhang<sup>1,2,3,20,21,\*</sup>

<sup>1</sup>Department of Genetics and Genomic Sciences, Icahn School of Medicine at Mount Sinai, One Gustave L. Levy Place, New York, NY 10029, USA

<sup>2</sup>Mount Sinai Center for Transformative Disease Modeling, Icahn School of Medicine at Mount Sinai, One Gustave L. Levy Place, New York, NY 10029, USA

<sup>3</sup>Icahn Institute for Data Science and Genomic Technology, Icahn School of Medicine at Mount Sinai, One Gustave L. Levy Place, New York, NY 10029, USA

<sup>4</sup>Nash Family Department of Neuroscience, Icahn School of Medicine at Mount Sinai, 1425 Madison Avenue, New York, NY 10029, USA

<sup>5</sup>Friedman Brain Institute, Icahn School of Medicine at Mount Sinai, 1425 Madison Avenue, New York, NY 10029, USA

<sup>6</sup>Department of Psychiatry, Icahn School of Medicine at Mount Sinai, 1425 Madison Avenue, New York, NY 10029, USA

<sup>7</sup>Department of Alzheimer's Disease Research, Center for Development of Advanced Medicine for Dementia, National Center for Geriatrics and Gerontology, Obu, Aichi 474-8511, Japan

<sup>8</sup>Department of Pharmacological Sciences and Oncological Sciences, Icahn School of Medicine at Mount Sinai, 1425 Madison Avenue, New York, NY 10029, USA

<sup>9</sup>Mount Sinai Center for Therapeutics Discovery, Icahn School of Medicine at Mount Sinai, New York, NY 10029, USA

<sup>10</sup>Tisch Cancer Institute, Icahn School of Medicine at Mount Sinai, New York, NY 10029, USA

<sup>11</sup>Department of Biological Sciences, Graduate School of Science, Tokyo Metropolitan University, Tokyo 192-0397, Japan

<sup>12</sup>Department of Neurology, Icahn School of Medicine at Mount Sinai, New York, NY 10029, USA

<sup>13</sup>Alzheimer's Disease Research Center, Icahn School of Medicine at Mount Sinai, New York, NY 10029, USA

<sup>14</sup>Department of Pediatrics, Icahn School of Medicine at Mount Sinai, New York, NY 10029, USA

<sup>15</sup>The New York Stem Cell Foundation Research Institute, New York, NY 10019, USA

<sup>16</sup>Neurology, JJ Peters VA Medical Center, 130 West Kingsbridge Road, Bronx, NY 10468, USA

<sup>17</sup>Psychiatry, JJ Peters VA Medical Center, 130 West Kingsbridge Road, Bronx, NY 10468, USA

<sup>18</sup>Department of Experimental Gerontology, Graduate School of Pharmaceutical Sciences, Nagoya City University, Nagoya 467-8603, Japan

<sup>19</sup>These authors contributed equally

<sup>20</sup>Senior author

<sup>21</sup>Lead Contact

\*Correspondence: bin.zhang@mssm.edu

<https://doi.org/10.1016/j.neuron.2020.11.002>

## SUMMARY

To identify the molecular mechanisms and novel therapeutic targets of late-onset Alzheimer's Disease (LOAD), we performed an integrative network analysis of multi-omics profiling of four cortical areas across 364 donors with varying cognitive and neuropathological phenotypes. Our analyses revealed thousands of molecular changes and uncovered neuronal gene subnetworks as the most dysregulated in LOAD. *ATP6V1A* was identified as a key regulator of a top-ranked neuronal subnetwork, and its role in disease-related processes was evaluated through CRISPR-based manipulation in human induced pluripotent stem cell-derived neurons and RNAi-based knockdown in *Drosophila* models. Neuronal impairment and neurodegeneration caused by *ATP6V1A* deficit were improved by a repositioned compound, NCH-51. This study provides not only a global landscape but also detailed signaling circuits of complex molecular interactions in key brain regions affected by LOAD, and the resulting network models will serve as a blueprint for developing next-generation therapeutic agents against LOAD.



## INTRODUCTION

Sporadic late-onset Alzheimer's disease (LOAD), the most prevalent form of dementia among people over the age of 65, is a progressive and irreversible brain disorder. Over 5.5 million people in the United States are affected by LOAD, which is currently the sixth leading cause of death in the United States and costs more than \$200 billion annually (Alzheimer's Association, 2018). There is an urgent need to develop effective methods to prevent, treat, or delay the onset or progression of LOAD. Conventional genome-wide association studies (GWASs) have revealed ~30 loci associated with LOAD (Jansen et al., 2019; Kunkle et al., 2019; Lambert et al., 2013; Marioni et al., 2018), with ~40% of the total phenotypic variance explained by these common variants (Ridge et al., 2013). However, the genuine causal variants responsible for the functional effect on the disease are still uncharacterized. Translating these genetic associations into biological mechanisms of disease pathogenesis and therapeutic interventions remains a huge challenge.

We previously pioneered a systems biology approach to integrate genotyping and microarray transcriptomic data from over 500 brains of LOAD and control subjects from the Harvard Brain Tissue Resource Center (HBTRC) (Zhang et al., 2013a), where we analyzed transcriptomic networks in 3 brain regions, including the dorsolateral prefrontal cortex (DLPFC), visual cortex (VC), and cerebellum (CB), and highlighted an immune-microglia network module and its network key driver *TYROBP* for relevance to LOAD pathology. Similar systems approaches have been performed recently on a number of large-scale omics studies of LOAD (Allen et al., 2016; De Jager et al., 2018; Johnson et al., 2020; Mostafavi et al., 2018; Ping et al., 2018), illuminating new biological pathways and targets. Although those existing studies nominated various dysfunctional subnetworks and genes in association with LOAD, little progress has been achieved regarding therapeutic agents targeting those dysfunctional components.

In this study, we describe a new multi-omics dataset generated from multiple brain regions in a large collection of LOAD brains. Application of a network analysis-based discovery platform to this dataset identified multiple neuron-specific gene subnetworks most dysregulated in LOAD in addition to a number of other pathways, such as immune response implicated previously in LOAD. *ATP6V1A*, a top predicted driver of the neuronal subnetworks, was validated *in vitro* and *in vivo*. More importantly, a compound targeting *ATP6V1A* and its regulated subnetwork was predicted and then validated experimentally to improve neuronal and neurodegenerative phenotypes induced by *ATP6V1A* deficit.

## RESULTS

### A Transformative Network Modeling Platform for Mechanism Discovery, Target Identification, and Therapeutic Agent Development for Alzheimer's Disease (AD)

We recently generated matched whole-genome sequencing (WGS) and RNA sequencing (RNA-seq) data from a cohort of 364 brains spanning the full spectrum of LOAD-related cognitive

and neuropathological disease severities represented in the Mount Sinai Brain Bank (MSBB) (Table S1; Haroutunian et al., 2009; Wang et al., 2016, 2018). Specifically, RNA-seq was performed in 4 brain regions: Brodmann area 10 frontal pole (BM10-FP), Brodmann area 22 superior temporal gyrus (BM22-STG), Brodmann area 36 parahippocampal gyrus (BM36-PHG), and Brodmann area 44 inferior frontal gyrus (BM44-IFG) (Figure 1). To integrate omics and disease trait data, we employed a transformative network modeling platform (Figure 1) that includes gene signature identification, co-expression network analysis (Song and Zhang, 2015), causal network inference (Schadt et al., 2005; Zhu et al., 2007), drug repositioning (Zhou et al., 2018), and *in vitro* and *in vivo* functional validations. A unique feature of our platform is using gene-regulatory networks as a target-rich environment for integrating multiple levels of data to identify key pathways and driver genes whose perturbation responses can recapitulate predicted network structures through systems like human induced pluripotent stem cell (hiPSC)-derived neurons and fly models of  $\beta$ -amyloid (A $\beta$ ) toxicity (Figure 1).

### BM36-PHG Shows the Most Expression Change in LOAD

After data preprocessing (Figure S1), differentially expressed genes (DEGs) were called with respect to 4 LOAD-related semi-quantitative traits (Table S2; Figure S2A). BM36-PHG had the largest number of DEGs, followed by BM22-STG, BM10-FP, and BM44-IFG (Figure S2B), consistent with our previous pan-cortical transcriptomic analysis of LOAD brains (independent of the dataset described here), in which BM36-PHG was the most affected region transcriptionally (Wang et al., 2016). As expected, neuronal system, transmission across chemical synapses, and neuroactive ligand receptor interaction were enriched for downregulated genes (Figure S3; Table S3). Our DEG signatures were preserved (adjusted Fisher's exact test [FET] p value up to 1.0E–100) in 10 publicly available AD transcriptomic studies (STAR Methods; Figure S4). Moreover, our downregulated genes were primarily preserved in the downregulated genes in astrocytes, neurons, oligodendrocytes, and oligodendrocyte progenitor cells from recent single-nucleus RNA-seq (snRNA-seq) of LOAD brains (Mathys et al., 2019; Figure S5). Our upregulated genes were primarily preserved in the upregulated genes in astrocytes and oligodendrocytes (adjusted FET p value up to 6.5E–45).

### Networks of LOAD Brains Highlight Multiple Neuronal Modules

To elucidate the interactions among genome-wide gene expression traits of LOAD, we constructed gene coexpression networks to identify gene modules using multiscale embedded gene coexpression network analysis (MEGENA) (Song and Zhang, 2015; Figure 2A; Tables S4 and S5). Distinct from our previous transcriptomics analysis of the DLPFC in the HBTRC cohort, which prioritized an immune-microglial module (Zhang et al., 2013a), the current study highlights the significance of multiple neuronal modules (Figure 2B; Table S6). Nine of the top 25 modules were enriched for neuron cell markers, correlated negatively with disease traits, and enriched for DEGs downregulated in LOAD, including M62, M65, M6, M236, M64, M252, M385,

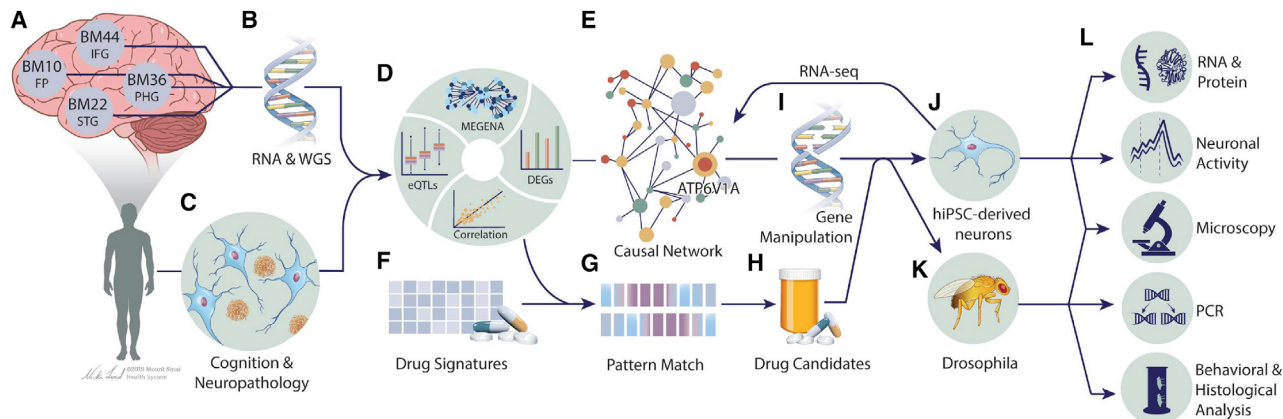


**Figure 1. A Transformative Network Modeling Platform for Mechanism Discovery, Target Identification, and Therapeutic Agent Development for AD**

(A–C) Functional genomics data from disease-modified brains and AD-related clinical and pathological phenotypes are collected.

(D) The input data are integrated to identify disease gene signatures and co-expressed gene modules using MEGENA.

(E) The top modules are projected onto causal networks to identify key driver genes of the disease.

(F–H) Candidate drugs that can reverse the disease gene signatures and driver genes are predicted by an advanced pattern-matching algorithm.

(I–L) The disease relevance of key drivers (e.g., *ATP6V1A*) is tested in model systems like hiPSC-derived brain cells and *Drosophila* through (1) gene perturbations and (2) drug rescue experiments.

M87, and M243 (Figure 2C). M64 was overrepresented with inhibitory neuron-enriched genes, whereas 6 others (M6, M87, M65, M236, M62, and M252) were overrepresented with excitatory neuron-enriched genes (Lake et al., 2016; Table S7). Topological structures of 4 of the top-ranked neuronal modules (i.e., M6, M62, M64, and M65) are shown in Figure 2D. All 4 modules were enriched in synaptic signaling to different degrees, but M6 and M64 were also enriched in regulation of long-term synaptic potentiation, synaptic vesicle trafficking, and localization (Figures 2E; Figure S6).

We validated the biological coherence of our network modules in previous transcriptomic network studies of LOAD. As shown in Table S6, more than 46.2% of the modules were strongly preserved (preservation statistics  $> 10$ ) in the Religious Orders Study and Rush Memory and Aging Project (ROSMAP) data (Mostafavi et al., 2018). Specifically, the top 25 modules showed strong preservation, except M74, which was moderately preserved. In the ROSMAP data (Mostafavi et al., 2018), there were 4 neuronal modules (m16, m21, m22, and m23) in which all but m16 were associated with cognitive decline or A $\beta$  burden ( $p < 0.05$ ). m21 and m23 significantly overlapped all current 9 top-ranked neuronal modules, whereas m16 and m22 were enriched in 3 and 7 of the current top-ranked neuronal modules, respectively (fold enrichment [FE] = 1.4~14.1, false discovery rate (FDR) up to 2.2E-39; Table S8).

#### Bayesian Network Analysis Predicts Novel Key Drivers of Top-Ranked Neuronal Modules

To determine potential network regulators (called key drivers) in the top-ranked modules, we constructed Bayesian probabilistic causal networks (BNs) (Figure 3A) using structural priors from expression quantitative trait loci (eQTLs) and transcription factor-target relationships (Tables S9–S13; Figures S7–S12). Figures S10 and S11 show a fine mapping of AD GWAS causal genes by

integrating eQTLs and GWAS statistics that led to marginally significant gene prioritization at two GWAS loci. We examined whether our BNs could predict publicly available gene perturbation signatures of the inferred key drivers. As illustrated in Figure 3B, ~50%–60% of the key driver perturbation signatures were enriched (i.e., significantly predicted) in the network neighborhoods of the corresponding key drivers. In contrast, the proportion of enriched perturbation signatures decreased to ~20%–30% in the network neighborhood of non-driver genes, suggesting the predictive power of the gene regulatory networks.

Next we projected each of the 9 top-ranked neuronal modules (Figure 2B) onto the BM36-PHG BN and identified 48 key drivers (42 unique genes) (Table S14), 10 of which were root nodes (without parental nodes) (Table S15). The key drivers *ATP6V1A* in M64 and *GABRB2* in M62 remained as root nodes in a union BN that combined directed edges from 4 region-wide BNs (Figure 3C; Figure S13). Only one prioritized key driver, *ATP6V1A*, was consistently downregulated across brain regions and disease stages in LOAD. This gene encodes a component (V1 subunit A) of vacuolar- or vesicular-type ATPase (v-ATPase), a multi-subunit enzyme that mediates lysosomal acidification (Chung et al., 2019; Zoncu et al., 2011) and energizes synaptic membranes in neurons (Abbas et al., 2020; Forgac, 2007). *ATP6V1A* was significantly downregulated in the BM36-PHG (~1.43-fold,  $p = 1.5\text{E}-6$ ) and BM22-STG (~1.25-fold,  $p = 2.1\text{E}-3$ ) regions of persons with dementia (clinical dementia rating [CDR]  $\geq 1$ ) and marginally downregulated in the BM10-FP region of persons with mild cognitive impairment (MCI) and frank dementia (CDR = 0.5) (~1.11-fold,  $p < 0.098$ ) (Figure 3D; Figure S14). In addition, *ATP6V1A* expression was negatively correlated with clinical and pathological traits in BM22-STG and BM36-PHG (Spearman correlation coefficients between -0.21 and -0.44,  $p$  values between 5.9E-11 and 3.3E-4), suggesting consistent downregulation of *ATP6V1A* at early and late stages

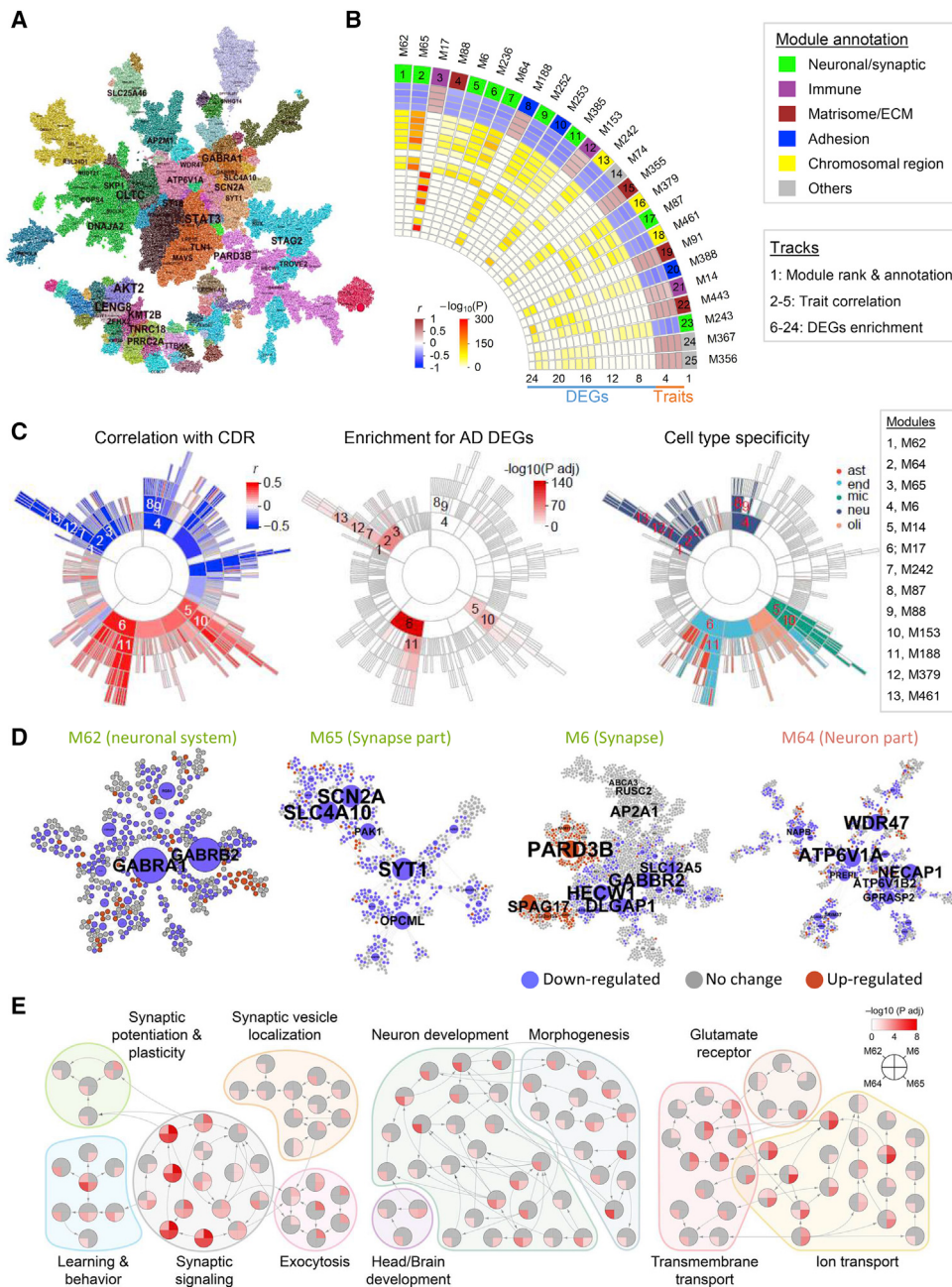


**Figure 2. Gene Coexpression Network Analysis Prioritizes Neuronal Modules Associated with LOAD**

(A) The MEGENA network in BM36-PHG. Node color denotes module membership. The font size of a gene name is proportional to the degree of connectivity.

(B) The 25 top-ranked modules. The heatmap shows the module ranking (number) and functional annotation (color) in track 1, the correlations ( $r$ ) with the traits (including bbscore, CDR, CERAD, and PlaqueMean) in tracks 2–5, and adjusted p values of enrichment for downregulated (tracks 6–14) and upregulated (tracks 15–24) DEGs.

(C) Sunburst plots showing the module hierarchy and correlation with CDR, enrichment for CDR demented versus nondemented DEGs, and enrichment for cell type markers. 1–13 denote the 13 top-ranked modules as listed on the right. ast, astrocytes; end, endothelial; mic, microglia; neu, neurons; oli, oligodendrocytes.

(D) Networks of the top-ranked neuronal modules M62, M65, M6, and M64. Node color denotes expression change in demented brains. Node size is proportional to node connectivity.

(E) Top-ranked neuronal modules enriched for Gene Ontology (GO) biological process (BP) hierarchy in relation to synaptic function, neuronal development, and transportation. Each node denotes a GO/BP term, with a pie chart displaying the significance of enrichment for the 4 neuronal modules in (D).

Enrichment p values are calculated from Fisher's exact test and adjusted by FDR. See also Figure S6 and Tables S5–S7.

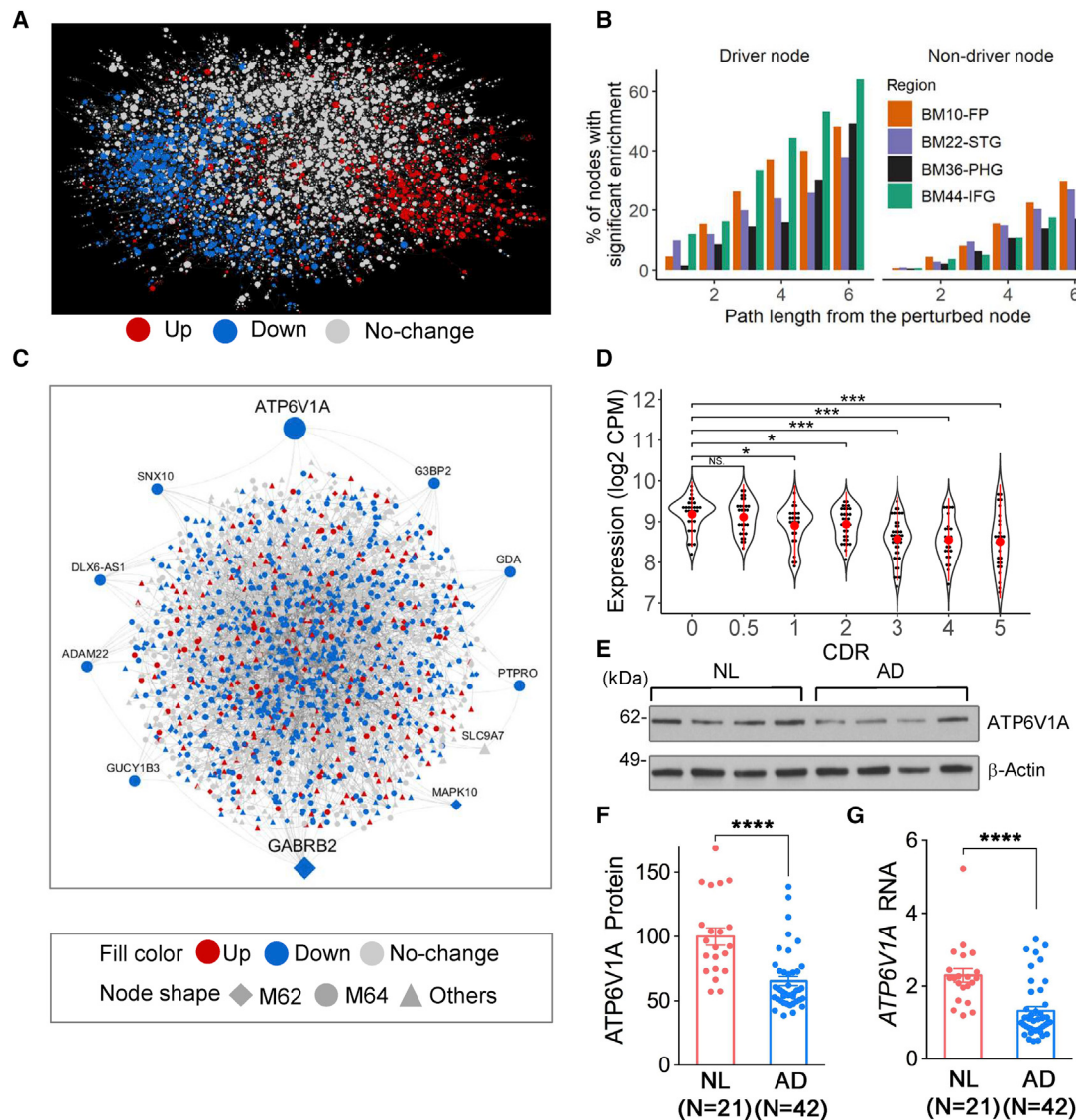


**Figure 3. Bayesian Probabilistic Causal Network (BN) Analysis Predicts Novel Key Drivers of LOAD**

(A) BN in the BM36-PHG.  
 (B) Validation of the BN structure. The left panel shows the percentage of the global BN key drivers whose network neighborhoods are enriched for the perturbation signature. The right panel shows the same analysis for the non-driver nodes.  
 (C) Projection of the modules M62 and M64 onto the BM36-PHG BN. Node labels are shown for the module key drivers.  
 (D–G) A novel network key driver, ATP6V1A, is downregulated in LOAD.  
 (D) ATP6V1A expression in the RNA-seq data of the BM36-PHG region as stratified by CDR.  
 (E–G) Validation of ATP6V1A expression change in MSBB BM36-PHG samples using western blot (WB; E and F) and qRT-PCR (G) analyses.  
 (E) Representative WB of ATP6V1A level.

t test or ANOVA with Dunnett's test; error bars represent SE; \* $p < 0.05$ , \*\* $p < 0.01$ , \*\*\* $p < 0.001$ , \*\*\*\* $p < 0.0001$ ; NS, no significance; NL, normal control. See also Figures S12–S14 and Tables S14 and S15.

of the disease. We validated the reduced expression of ATP6V1A in LOAD brains (Figures 3E–3G; 42% decrease at the mRNA level and 35% decrease at the protein level,  $p < 1.0E-4$ ). Downregulation of ATP6V1A has also been identified previously in cortical neurons of the superior frontal gyrus (Satoh et al., 2014) and the hippocampus CA1 area (Blalock et al., 2004) of LOAD brains. In addition, it was downregulated in the excit-

atory (0.8-fold, adjusted  $p = 2.6E-117$ ) and inhibitory (0.83-fold, adjusted  $p = 6.7E-22$ ) neurons in brains with early pathology of LOAD compared with no-pathology brains in the ROSMAP cohort (Mathys et al., 2019). To validate the functional role of ATP6V1A in LOAD, we performed gene perturbation experiments in *in vitro* (neurons) and *in vivo* (transgenic flies) models.

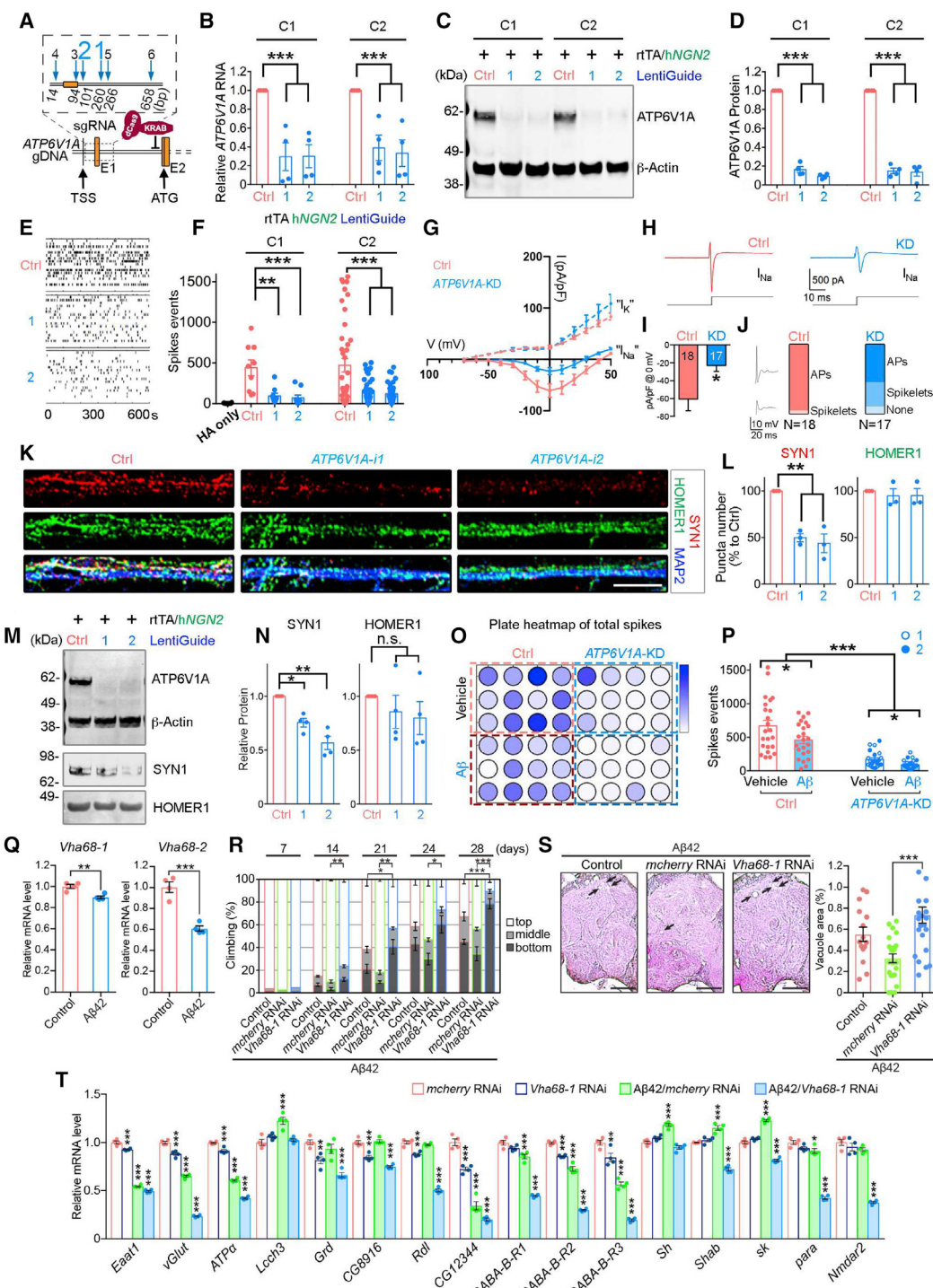


**Figure 4. Repression of *ATP6V1A* Leads to Neuronal Malfunction in Human NGN2 Neurons and  $\text{A}\beta42$  Transgenic Flies**

(A) *ATP6V1A* gene editing by the CRISPR/dCas9-KRAB system. 6 different gRNAs are designed for targeting the *ATP6V1A* promoter. TSS, transcription start site. The ATG translation initiation codon is in exon 2.

(B) qRT-PCR analysis (n = 4) confirms the decreased *ATP6V1A* RNA by gRNA candidates 1 and 2 (i1 and i2) in 2 independent cell lines of iNs (i.e., C1 and C2).

(C and D) Representative WB and quantitative analysis (n = 4) of *ATP6V1A* protein levels in iNs.  $\beta$ -Actin is a loading control.

(E and F) Representative raster plots of spike events over 10 min and analysis (n = ~6–45 wells) of day 21 iNs.

(G) Current-voltage (I-V) plot for inward sodium currents ( $I_{Na}$ ) and outward potassium currents ( $I_K$ ). Current density (picoamperes/picofarads) is shown. The holding potential was  $-80$  mV.

(legend continued on next page)

## Functional Validation Confirms Decreased Neuronal Activity in ATP6V1A-Deficient NGN2-Neurons

Because *ATP6V1A* was downregulated in LOAD brains and enriched for neuronal expression (Figure S15), we developed a model of hiPSC-derived *NGN2* neurons (iNs) with reduced expression of *ATP6V1A*. To repress endogenous *ATP6V1A*, we utilized CRISPR inhibition (CRISPRi) (Ho et al., 2017), in which dCas9 (dead Cas9) is fused to the Krüppel-associated box (KRAB) transcriptional repressor (Gilbert et al., 2014). We designed 6 gRNAs to target the promoter region for knockdown (KD) of *ATP6V1A* (Figure 4A), and identified 2 gRNAs (*ATP6V1A*-i1 and -i2) that efficiently repressed *ATP6V1A* in neural progenitor cells (NPCs) from 2 donors stably expressing dCas9-KRAB (Figures S16A–S16C). In post-mitotic day 21 (D21) *NGN2*-induced excitatory neurons well characterized by electrophysiological properties and neuronal morphology (Figure S16D; Ho et al., 2016), the *ATP6V1A* RNA (~60%–70% repression, p < 0.001; Figure 4B) and protein levels (~80%–90% repression, p < 0.001; Figures 4C and 4D) were reduced significantly.

Because v-ATPase activity facilitates transporters to load vesicles with neurotransmitters (Abbas et al., 2020; Forgac, 2007), we determined whether *ATP6V1A* KD influenced spontaneous neuronal electric activity. Isogenic pairs of control and *ATP6V1A* CRISPRi iNs (co-cultured with human fetal astrocytes to enhance neuronal maturation) were evaluated across a panel of assays. We applied an Axion multi-electrode array (MEA) to assess the effect of *ATP6V1A* repression on population-wide neuronal activity, including frequency and coordination of network firing. Significantly reduced neuronal activity was observed following perturbations with gRNA (average 4.3-fold down in D21 iNs, p < 0.01; Figures 4E and 4F). We further measured the amplitude of voltage-gated potassium current ( $I_K$ ) and sodium current ( $I_{Na}$ ) using whole-cell patch-clamp recordings (Figures 4G–4I). *ATP6V1A* KD neurons exhibited significantly smaller  $I_{Na}$  density (p = 0.015) but no significant change in  $I_K$  (Figures 4G–4I). Consistent with a decrease in  $I_{Na}$ , RNA-seq of D21 iNs (detailed below) revealed significantly reduced mRNA expression of different voltage-gated sodium channel subunits, such as *SCN3A*, *SCN2A*, and *SCN4B* (Figure S17). Last, we observed a decrease in the number of full action potentials and an increase in immature spikes (e.g., spikelets) in the *ATP6V1A* CRISPRi group (Figure 4J).

To explore the effect of *ATP6V1A* on synaptic components, iNs were immunostained against the presynaptic *SYN1* and the postsynaptic *HOMER1* and analyzed by confocal imaging (Figure 4K). A significant reduction in *SYN1*<sup>+</sup> punctum number following *ATP6V1A* CRISPRi was observed (1.1-fold down, p < 0.001; Figures 4K and 4L), whereas CRISPRi had a limited effect on *HOMER1* (Figure 4L). A western blot showed similar results. A 25%–45% reduction of *SYN1* (p < 0.05) was observed, whereas *HOMER1* was expressed at comparable levels regardless of CRISPRi (Figures 4M and 4N). In *ATP6V1A*-deficient iNs, only presynaptic components (*SYN1* and *vGLUT1*) were decreased significantly in RNA (~20% down, p < 0.05, and ~38% down, p < 0.01, respectively; Figure S17A). Postsynaptic components (*HOMER1* and *PSD95*) showed no significant change, but *vGLUT1* protein levels decreased by ~22% (p < 0.05; Figures S18A–S18C).

AD neuronal pathology is associated with extracellular A $\beta$  aggregates (Murphy and LeVine, 2010). A $\beta$  administration (24 h, 5  $\mu$ M) significantly decreased spontaneous neuronal activity (p < 0.05; Figures 4O and 4P) with a slight but insignificant decrease in *ATP6V1A* expression (14.4% down in wild-type [WT] neurons and 35.5% down in *ATP6V1A* CRISPRi neurons, respectively; Figures S19A–S19C). Moreover, *ATP6V1A* repression in combination with A $\beta$ 42 exposure further impaired neuronal activity (p < 0.05; Figures 4O, 4P, S19B, and S19C).

## Neuronal KD of *Vha68-1*, a Fly Ortholog of *ATP6V1A*, Worsens Behavioral Deficits and Neurodegeneration in A $\beta$ 42 Flies

We also examined the effects of knocking down the fly ortholog of *ATP6V1A* on neuronal integrity in *Drosophila*. According to the DRSC Integrative Ortholog Prediction Tool, *Drosophila* vacuolar H $^{+}$  ATPase 68-kD subunit 1 (*Vha68-1*, CG12403) and *Vha68-2* (CG3762) are the best orthologs of human *ATP6V1A* protein. Using the GAL4-upstream activating sequence (UAS) system, several shRNAi constructs targeting different regions of *Vha68-1* or *Vha68-2* were expressed in neurons by the pan-neuronal *elav*-GAL4 driver. Because *Vha68-1* and *Vha68-2* are essential genes and their strong KD caused lethality, we selected an RNAi line that modestly reduced *Vha68-1* levels (Figure S20A). The forced climbing assay, a quantitative way to assess neuronal dysfunction (Iijima et al., 2004), revealed that neuronal KD of

(H) Representative examples of putative inward voltage-gated sodium current at 0 mV.

(I) Bar plot showing mean inward sodium current densities at 0 mV for *ATP6V1A* KD (n = 17) and control neurons (n = 18) (p = 0.015).

(J) Boxplots showing the fraction of neurons that displayed a full action potential (AP), spikelets, or no events with a current injection step (0.1 nA) positive to the threshold for control and KD neurons. The inset shows representative examples of APs and spikelets.

(K) Representative confocal images of synaptic proteins (*SYN1*, red; *HOMER1*, green) and the pan-neuronal marker *MAP2* (blue). Scale bar, 20  $\mu$ m.

(L) Analysis of *SYN1*- and *HOMER1*-immunoreactive punctum numbers (n = 3).

(M and N) Representative WB and quantitative analysis (n = 4) of *SYN1* and *HOMER1* levels.

(O and P) MEA after exposure to 5  $\mu$ M A $\beta$  at 24 h.

(Q) Plate map of total spike events.

(P) Analysis of spike events (n = 12 wells).

(Q) mRNA levels of *Vha68-1* and *Vha68-2* were decreased in A $\beta$ 42 fly heads (n = 4).

(R) *Vha68-1* KD in neurons exacerbated locomotor deficits caused by A $\beta$ 42, as revealed by climbing assay. n = 5 except for day 7 (n = 2).

(S) Neuronal KD of *Vha68-1* significantly worsened neurodegeneration in A $\beta$ 42 fly brains. Representative images show the central neuropil of 33-day-old fly brains. Scale bars, 50  $\mu$ m. Percentages of vacuole areas (indicated by arrows) were analyzed. n = 12–24 hemispheres.

(T) mRNA levels of genes related to synapse biology were significantly reduced in A $\beta$ 42-expressing flies with neuronal KD of *ATP6V1A/Vha68-1* (n = 4).

See also Figures S16–S21. See Figure 3 for statistical test and p value annotations.

*Vha68-1* by itself caused a modest decline in climbing ability in aged flies (Figure S20B).

A transgenic *Drosophila* expressing human A $\beta$ 42 showed age-dependent locomotor deficits and neurodegeneration in the brain (Iijima et al., 2004). Interestingly, the mRNA expression levels of *Vha68-1* and *Vha68-2* were significantly reduced in A $\beta$ 42 flies (Figure 4Q), suggesting that their reduction may play a role in A $\beta$ 42-mediated toxicity. We found locomotor deficits to be exacerbated significantly by neuronal KD of *Vha68-1* (Figure 4R). To minimize potential off-target effects, the experiment was repeated with shRNA targeting a different region of *Vha68-1*, and similar results were obtained (Figures S20C–S20E). As further validation, we utilized a mutant allele of *Vha68-1* (*Vha68-1*<sup>1</sup>) with a loss-of-function single-nucleotide mutation (Q519L) caused by mutagenesis (Zhao et al., 2018). Locomotor deficits were worsened significantly in A $\beta$ 42 flies with a heterozygous mutation of *Vha68-1*<sup>1</sup>, whereas a heterozygous *Vha68-1*<sup>1</sup> by itself did not cause climbing defects (Figures S21A and S21B).

In *Drosophila*, brain vacuolation is a morphological hallmark of neurodegeneration that can be assessed quantitatively. Neuronal expression of A $\beta$ 42 causes an age-dependent appearance of vacuoles in the fly brains (Iijima et al., 2004). RNAi-mediated KD of *Vha68-1* significantly worsened this neurodegeneration (Figure 4S). Neurodegeneration was worsened slightly in flies with heterozygous *Vha68-1*<sup>1</sup>, with no statistically significant difference (Figure S21C).

To assess whether altered neuronal activity underlies toxic interactions between *Vha68-1* deficiency and A $\beta$ 42 in flies, we examined the mRNA levels of 16 genes related to synaptic biology, focusing on GABAergic/glutamatergic systems and ion channels (Figure 4T). Compared with control flies, the mRNA levels of 9 genes were significantly reduced by neuronal KD of *Vha68-1*, whereas 8 genes were reduced significantly by A $\beta$ 42 (Figure 4T). 6 genes (*SLC1A2/Eaat1*, *SLC17A6-8/vGlut*, *ATP1A1-3/ATP $\alpha$* , *GLRA2/CG12344*, *GABBR2/GABA-B-R2*, and *GABBR2/GABA-B-R3*) were commonly reduced under both conditions (Figure 4T). In contrast, neuronal KD of *Vha68-1* in A $\beta$ 42 flies dramatically reduced the mRNA levels of 14 of 16 genes compared with control flies (Figure 4T). Key driver genes, including *GABA1/Grd* in M62, *SCN2A/para* in M65, and *GABBR2/GABA-B-R2,3* in M6 (Figure 2D) were downregulated in these fly brains, suggesting functional links between these networks and *ATP6V1A/Vha68-1* in the M64 module.

In summary, these results suggest that *ATP6V1A/Vha68-1* deficiency and A $\beta$ 42 synergistically downregulate key regulator genes of neuronal activity and exaggerate A $\beta$ 42-induced toxicities in flies.

#### ATP6V1A KD Signatures Are Enriched in ATP6V1A-Regulated Networks in Human LOAD Brains

To characterize the molecular changes and validate the sub-network regulated by *ATP6V1A*, we performed RNA-seq on 4 groups of iNs (designated WT-V and WT-A $\beta$  for vehicle-treated and A $\beta$ -treated *ATP6V1A* WT neurons, respectively, and KD-V and KD-A $\beta$  for vehicle-treated and A $\beta$ -treated *ATP6V1A* KD neurons, respectively). No gene shows significant changes between

A $\beta$ -treated and vehicle-treated cells in the *ATP6V1A* KD or WT genotype. In contrast, there were 3 DEGs from KD-V versus WT-V, 55 DEGs from KD-A $\beta$  versus WT-A $\beta$ , and 326 DEGs from KD-A $\beta$  versus WT-V (Table S16; Figure S22). By employing a gene set enrichment analysis (GSEA) (Subramanian et al., 2005), we found V-ATPase transport and phagosome maturation/acidification to be downregulated in KD-V versus WT-V (Figure 5A; Table S17). Consistent with the functional assay above, KD-V versus WT-V led to downregulation of multiple synapse biology pathways, with greater downregulation after exposure to A $\beta$  treatment in KD-A $\beta$  versus WT-A $\beta$ .

Because a combination of *ATP6V1A* KD and A $\beta$  treatment led to more molecular changes than individual factor perturbation, we explored potential synergistic effects between the two factors (Schrode et al., 2019). The hierarchical clustering of the log fold changes (FCs) of all genes for each contrast showed differences between the predicted and observed cumulative effects (Figure S23). There was strong enrichment of disorder and cellular stress gene sets after individual KD or A $\beta$  treatment, whereas KD showed further associations with cell death and negative correlation with neuronal function signatures. The latter was amplified markedly in the combinatorial modulation (Figure 5B). We grouped genes into synergism categories based on differential expression between the additive model and the combinatorial modulation. Most genes were altered as predicted, but with 6% (1,152 genes) more downregulated and 9% (1,773 genes) more upregulated than expected (Figure 5C). Genes more upregulated than expected from an additive model were enriched significantly for cell death and cellular stress gene sets (Figure 5C).

The genes affected by *ATP6V1A* KD or A $\beta$  perturbation were significantly enriched in the LOAD DEG signatures identified from the current study and 10 published datasets (Figure 5A; Table S18). By GSEA, we noted that the top-ranked neuronal modules (M64, which contains *ATP6V1A*, M62, M65, M6, M236, M252, M385, M87, and M243) were downregulated in KD-A $\beta$  cells compared with WT-V cells (Table S19). Several immune response modules (M14, M153, M366, and M428) were upregulated in KD-A $\beta$  cells compared with WT-V cells. As summarized in Table S20 and exemplified in Figure 5D, the genes surrounding *ATP6V1A* on the BM36-PHG BN were enriched for downregulation signals of *ATP6V1A* KD, with the most significant enrichment from KD-A $\beta$  versus WT-V (FDR = 4.1E-6). In summary, the *ATP6V1A*-deficit signature in iNs mirrors the prediction in the human LOAD gene networks.

#### A Novel Drug, NCH-51, Improves ATP6V1A Levels and Neuronal Activity

We further explored potential drugs that can rescue the *in vitro* and *in vivo* phenotypes arising from *ATP6V1A* deficits. With our drug repositioning tool, Ensemble of Multiple Drug Repositioning Approaches (EMUDRA) (Zhou et al., 2018), we matched the disease signature from the BM36-PHG region and the signatures of 3,629 drugs tested in NPCs in the Library of Integrated Network-based Cellular Signatures (LINCS) project (Keenan et al., 2018; Figure 6A). Candidate drugs were further prioritized by their

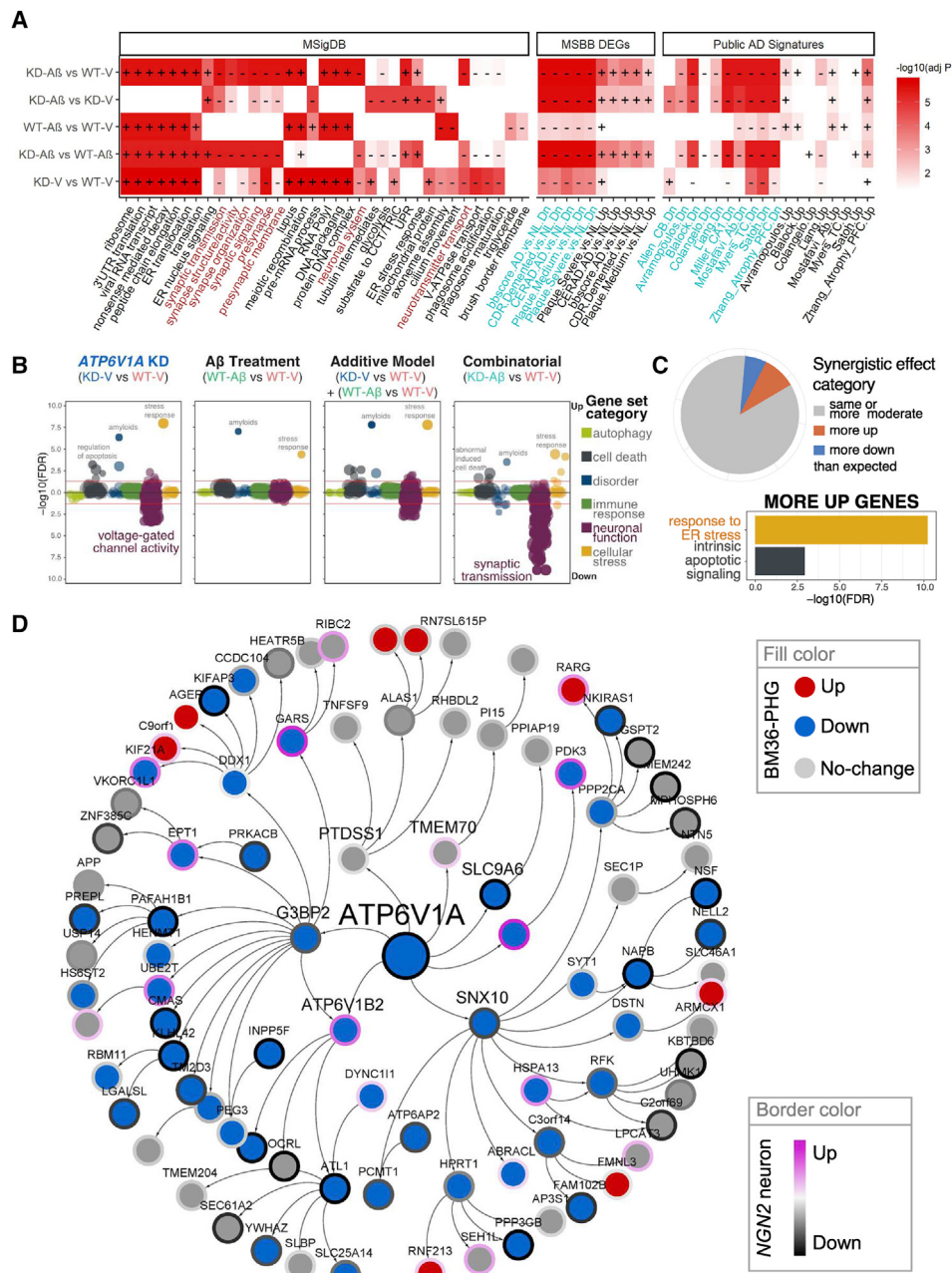


**Figure 5. RNA-Seq Analysis of ATP6V1A KD Neurons Validates ATP6V1A-Regulated Neuronal Networks in LOAD Brains**

(A) Top Molecular Signatures Database (MsigDB) gene sets and human AD signatures enriched in the perturbations of iNs. Plus (+) and minus (−) symbols denote the sign of the GSEA enrichment score (ES). Brown in the x axis of the left panel highlights the neuron-related terms. Cyan in the x axis of the two right panels highlights the downregulated signatures.

(B and C) Analysis of the synergistic effect between ATP6V1A KD and Aβ treatment in iNs.

(B) Summary of the functional categories that are likely to be affected by the synergistic effect. p values are calculated by the camera function in the limma package and adjusted by FDR.

(C) Pie chart showing percentages of genes that exhibit a synergistic difference following combinatorial treatment compared with the expected additive model. The bar chart shows pathways enriched for genes with “more up” regulation.

(D) Genes within a path length of 3 from ATP6V1A on the BM36-PHG BN were enriched for downregulated signals of Aβ-KD versus V-WT (GSEA normalized ES = 2.3, adjusted p = 8.3E-6).

Enrichment p values in (A) and (C) are calculated from Fisher's exact test and adjusted by FDR. See also Figures S22 and S23 and Tables S16–S20.

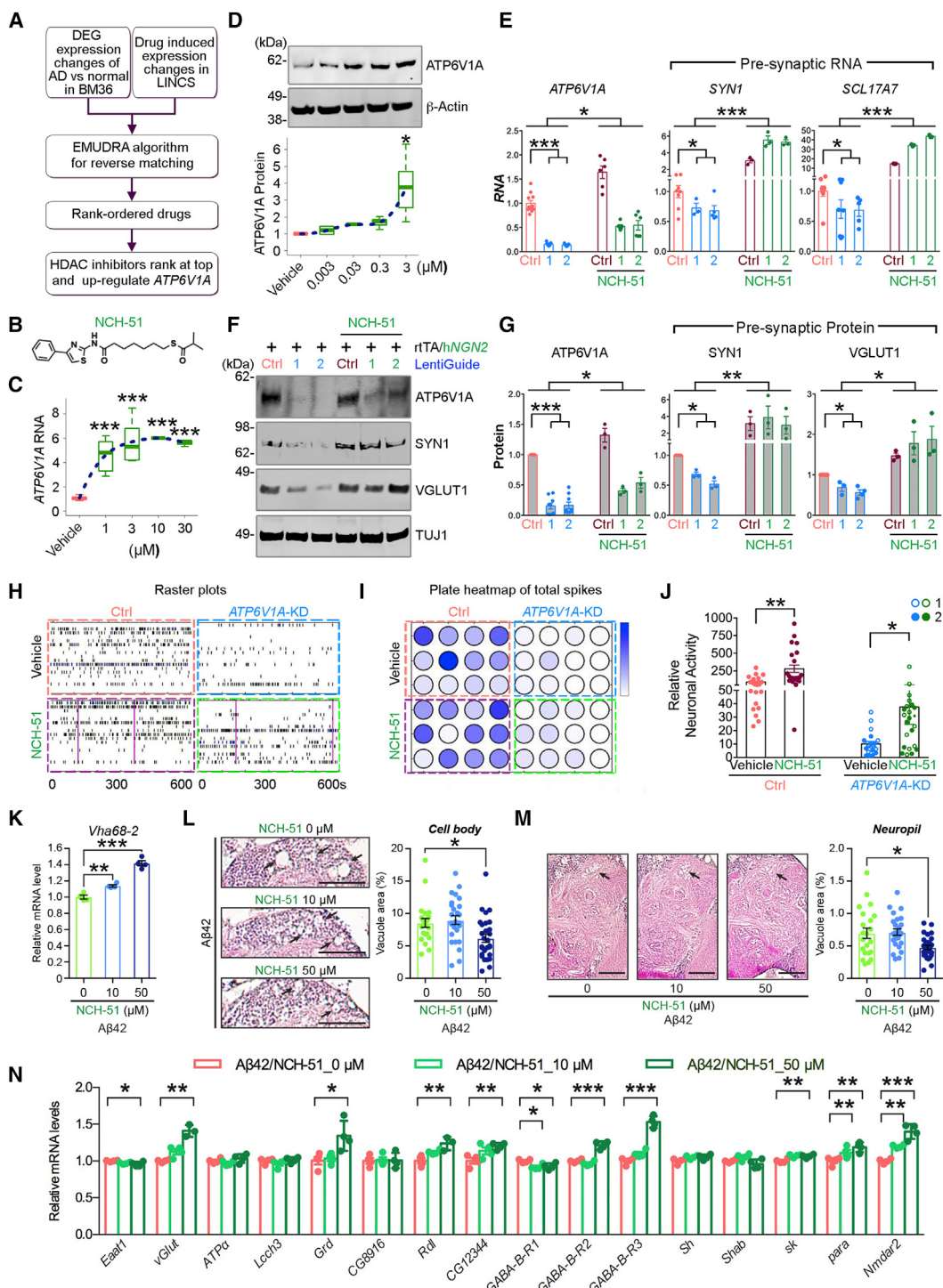


**Figure 6. A Novel Compound, NCH-51, Increases ATP6V1A Expression and Partially Restores Neuronal Function**

(A) The procedure for predicting compounds that could increase ATP6V1A expression and the reverse transcriptomics signature of LOAD.

(B) Chemical structure of NCH-51.

(C) Effects of NCH-51 at 1, 3, 10, and 30 μM on ATP6V1A mRNA level after 24-h exposure.

(D) Effects of NCH-51 at 0.003, 0.03, 0.3, and 3 μM on ATP6V1A protein level after 48-h exposure. β-Actin is a loading control. A blue dotted line is curve fitted for the set of data points.

(E) mRNA expression of ATP6V1A and the presynaptic SYN1 and SCL17A7 in iNs in the absence and presence of 3 μM NCH-51. n = 3–12.

(F and G) Representative WB and quantitative analysis (n = 3–8) of ATP6V1A, SYN1, and VGLUT1 proteins. TUJ1 is a loading control.

(legend continued on next page)

potential to increase the mRNA expression of *ATP6V1A* in NPCs. Interestingly, the top prioritized drugs contain several histone deacetylase (HDAC) inhibitors such as SAHA, NCH-51, and MS-275 (Table S21).

To verify the prediction, we measured the transcriptional and translational levels of *ATP6V1A* in D21 iNs treated with the 3 HDAC inhibitors at a series of concentrations between 1 and 30  $\mu$ M. Only NCH-51 effectively increased *ATP6V1A* levels (Figures 6B–6D), whereas SAHA and MS-275 were ineffective (Figures S24A–S24F), suggesting that the HDAC-inhibitory activity of NCH-51 is not required for modulating *ATP6V1A*. A time-course experiment indicated that 24-h treatment resulted in sufficient production of *ATP6V1A* mRNA; 3  $\mu$ M NCH-51 was adequate to significantly increase the protein yield (Figure 6D).

NCH-51 (3  $\mu$ M, 24 h) dramatically elevated the mRNA levels of *ATP6V1A* ( $p < 0.05$ ), presynaptic *SYN1* ( $p < 0.001$ ), and *SCL17A7* ( $p < 0.001$ ), particularly in *ATP6V1A* KD iNs (Figure 6E). The protein levels of *ATP6V1A* ( $p < 0.05$ ), *SYN1* ( $p < 0.01$ ), and *VGLUT* ( $p < 0.05$ ) were increased similarly by NCH-51 (Figures 6F and 6G). NCH-51 had no effect on postsynaptic PSD95, whereas the HOMER1 level increased in *ATP6V1A* KD iNs or the isogenic controls following NCH-51 treatment (Figures S24G–S24I). The MEA indicated that NCH-51 was a potent activator of neuronal activity (Figures 6H–6J), partially restoring neuronal activity in *ATP6V1A* KD iNs (Figure 6J).

### Feeding NCH-51 Induces Expression of a Fly Ortholog of *ATP6V1A* and Suppresses Neurodegeneration in *A $\beta$ 42* Flies

NCH-51 feeding significantly increased the mRNA levels of *Vha68-2* (Figure 6K) but not *Vha68-1* (Figure S25A) in *A $\beta$ 42* fly brains in a dose-dependent manner. Because *Vha68-2* was decreased more dramatically compared with *Vha68-1* in *A $\beta$ 42* fly brains (Figure 4Q), NCH-51 treatment might counteract pathological reductions in *Vha68-2* levels. In support of this, NCH-51 feeding did not increase the mRNA levels of *Vha68-1* or *Vha68-2* in control flies (Figure S25B).

*A $\beta$ 42* flies were treated with 0, 10, or 50  $\mu$ M of NCH-51 during aging to examine the effects of NCH-51 treatment on neurodegeneration. Compared with control (0  $\mu$ M), 50  $\mu$ M treatment of NCH-51 significantly suppressed cell loss (Figure 6L) and neuropil degeneration (Figure 6M). NCH-51 did not affect *A $\beta$ 42* levels in fly brains (Figure S25C), suggesting that observed effects were not due to reduced *A $\beta$ 42* levels. NCH-51 also increased the mRNA levels of 9 of 16 key regulatory genes of neuronal activity, including 4 key network driver genes (*GABRA1/Grd* in M62, *SCN2A/para* in M65, and *GABBR2/GABA-B-R2,3* in M6; Fig-

ure 2D) in *A $\beta$ 42* fly brains (Figure 6N), suggesting that NCH-51 confers neuroprotective effects by correcting neuronal activity.

### DISCUSSION

Our integrative network analysis-based target nomination method complements the conventional linkage and linkage disequilibrium-based gene mapping methods in identifying the most relevant genes for functional studies. We highlighted multiple neuronal modules of particular relevance to LOAD pathology and predicted key regulators of these modules using BNs; one top driver, *ATP6V1A*, was tested experimentally for disease relevance. *ATP6V1A* is known for its role in the acidification of intracellular compartments such as the lysosome. Morpholino KD of *ATP6V1A* impairs acid secretion in zebrafish (Horng et al., 2007), small interfering (siRNA)-mediated KD induces autophagy activity in U87-MG cells (Kim et al., 2017), and KD of *ATP6V1A* in HeLa cells prevents drug-induced lysosomal acidification and autophagy activation (Chung et al., 2019). Under our experimental conditions, *ATP6V1A* CRISPRi in iNs did not significantly alter lysosomal pH according to cell acidic organelle labeling by Lysotracker Red DND-99 (data not shown). Instead, *ATP6V1A* CRISPRi downregulated neuronal activity-associated functional pathways, particularly in the presence of *A $\beta$ 42* peptides. Similar results were obtained in *A $\beta$ 42* flies: mRNA levels of fly orthologs of *ATP6V1A*, *Vha68-1/Vha68-2*, were reduced, and neuronal KD of *Vha68-1* exacerbated age-dependent behavioral deficits and neurodegeneration accompanied by downregulation of synaptic genes, suggesting evolutionarily conserved roles of *ATP6V1A* in maintaining neuronal activity and synaptic integrity. Although *de novo* heterozygous mutations (p.Asp349Asn and p.Asp100Tyr) in *ATP6V1A* in rat hippocampal neurons revealed contradictory effects on lysosomal acidification, both mutations lead to abnormalities in neurite outgrowth, branching, and synaptic connectivity (Fassio et al., 2018). The possible synaptic role of *ATP6V1A* in LOAD brains requires further investigation.

hiPSC-based models recapitulate disease-relevant features and gene expression signatures and identify deregulated genes with potential clinical implications (Hoffmann et al., 2018). Induced neurons also possess age-related signatures that have similarities to the transcriptomic aging signatures detected in postmortem human brain samples (Mertens et al., 2018). Likewise, here we show that the *ATP6V1A* KD signatures in iNs were highly enriched for the LOAD DEGs and the sub-network surrounding *ATP6V1A*, indicating that the hiPSC system is a promising avenue to model devastating diseases such as LOAD when living tissues are not available.

(H–J) MEA after exposure to 3  $\mu$ M NCH-51.

(H) Representative raster plots of the spike events over 10 min.

(I) plate map of total spike events.

(J) analysis of spike events ( $n = 24$  wells).

(K) NCH-51 increased mRNA levels of *Vha68-2* in *A $\beta$ 42* flies.  $n = 4$ .

(L and M) NCH-51 suppressed neurodegeneration in the cell body (L) and central neuropil regions (M) in 21-day-old *A $\beta$ 42* fly brains. Scale bars, 200  $\mu$ m. Percentages of vacuole areas (indicated by arrows) were analyzed.  $n = 22$ –28 hemispheres.

(N) NCH-51 increased mRNA levels of synaptic biology-related genes in *A $\beta$ 42* fly brains in a dose-dependent manner ( $n = 4$ ).

See also Figures S24–S26 and Table S21. See Figure 3 for statistical test and p value annotations.

To date, therapeutic agents that are promising in mouse models of AD have failed to benefit human patients (Egan et al., 2018; Honig et al., 2018), urging development of novel therapeutic targets and new model systems. Computational drug repositioning (Pushpakom et al., 2019; Zhou et al., 2018) provides a rapid and cost-effective route for translating transcriptional network findings into promising therapeutic agents. FK506, a drug known to induce autophagy by binding to ATP6V1A (Kim et al., 2017), was ineffective in recovering ATP6V1A expression at the mRNA or protein level in our ATP6V1A KD iNs (data not shown). This contrasts the current predicted novel drug candidate NCH-51, which activates ATP6V1A at the transcriptional and translational levels. We demonstrated that NCH-51 improved AD-related phenotypes, increasing neuronal activity in iNs and suppressing neurodegeneration in A $\beta$ 42 flies by recovering the expression of key regulators of neuronal activity. However, the molecular mechanisms by which NCH-51 acts remain unresolved. In the future, we will test NCH-51 on ATP6V1A-engineered mice and other mammalian models of AD.

Although the present study focused on the role of ATP6V1A on neuronal activity and A $\beta$ 42-mediated toxicity, tau pathology is closely associated with cognitive deficits and neurodegeneration in AD. Ectopic expression of human tau in fly eyes caused age-dependent and progressive neurodegeneration in the lamina, which contains photoreceptor axons (Ando et al., 2016). RNAi-mediated KD of *Vha68-1* or *Vha68-2* significantly exacerbated this axon degeneration (Figures S26A and S26B) without altering the accumulation or phosphorylation levels of tau (Figure S26C), suggesting that ATP6V1A may have broad neuroprotective effects and is a potential therapeutic target for other neurodegenerative diseases involving tau.

A limitation of the current bulk transcriptomic data is that the expression changes may be confounded by cell type composition difference. Consistent with existing knowledge, we confirm through deconvolution analysis that LOAD brains showed progressive neuronal cell loss as the severity advanced, accompanied by a gradual increase of glial cells (Figure S27). With the current technology, we can study diseased tissues at the single-cell level (Deczkowska et al., 2018). Compared with a recent snRNA-seq analysis of LOAD (Mathys et al., 2019), we found significant preservations of our gene signatures (Figure S4), suggesting that cell type proportion change may have a limited effect on the gene signatures identified here. Nonetheless, we anticipate future cell-type-specific network models to offer more in-depth understanding of the cellular complexity and etiology underlying the devastating disease.

In summary, we employed a transformative platform to systematically identify molecular signatures, multiscale gene networks, and key regulators of LOAD in 4 brain regions. We uncovered a number of relatively independent neuronal enriched gene subnetworks that were highly dysregulated in LOAD. We validated one predicted top key driver of the dysregulated neuronal system, ATP6V1A, *in silico*, *in vitro*, and *in vivo* and demonstrated NCH-51, a compound that can increase the expression level of ATP6V1A, to be a promising therapeutic candidate for treating LOAD.

## STAR METHODS

Detailed methods are provided in the online version of this paper and include the following:

- KEY RESOURCES TABLE
- RESOURCE AVAILABILITY
  - Lead Contact
  - Materials Availability
  - Data and Code Availability
- EXPERIMENTAL MODEL AND SUBJECT DETAILS
  - Human Postmortem Brain Tissue Samples
  - Human Induced Pluripotent Stem Cell Lines
  - *Drosophila* Models
- METHOD DETAILS
  - The MSBB-AD cohort data quality control and preprocessing
  - Differential expression analysis
  - Overlap and functional enrichment analysis
  - Cell-type deconvolution analysis
  - MEGENA gene coexpression network analysis
  - Network connectivity preservation analysis
  - Discovery of region-wide expression quantitative trait loci (eQTLs)
  - Integrating eQTL, gene expression traits, and LOAD GWAS loci to identify causal LOAD genes
  - Bayesian probabilistic causal network inference and key driver analysis
  - Drug repositioning of AD signature in neural progenitor cells
  - Lentivirus generation
  - gRNA design and cloning for *in vitro* functional validation of ATP6V1A deficit in NGN2-neurons
  - hiPSC-NPC culture and NGN2 neuronal differentiation
  - Primary human astrocyte (pHA) co-culture
  - RNA sequencing data processing of ATP6V1A KD and A $\beta$ -treated neurons
  - ATP6V1A KD and A $\beta$ -treatment synergistic effect analysis from the RNA-seq data
  - Quantitative reverse transcription PCR (qRT-PCR) of ATP6V1A
  - Preparation of cell lysates and western blotting
  - Immunofluorescence and microscopy
  - $\beta$ -Amyloid preparation and treatment
  - Multi-electrode array (MEA)
  - Electrophysiology
  - ATP6V1A orthologs in fly
  - RNA extraction and quantitative real time PCR analysis
  - Climbing assay
  - Histological analysis
  - Drug feeding in flies
  - Western blotting analysis of fly models
- QUANTIFICATION AND STATISTICAL ANALYSIS

## SUPPLEMENTAL INFORMATION

Supplemental Information can be found online at <https://doi.org/10.1016/j.neuron.2020.11.002>.

**ACKNOWLEDGMENTS**

We thank Ni-ka Ford and Dr. Gale Justin from the Instructional Technology Group at the Icahn School of Medicine at Mount Sinai for producing the illustration of Graphical Abstract and [Figure 1](#). We thank the Bloomington Drosophila Stock Center and the Vienna *Drosophila* Resource Center for fly stocks. We thank Mette Peters and Nicole Kauer for setting up the data sharing page on the Synapse platform. This work was supported in part by the computational and data resources and staff expertise provided by Scientific Computing at the Icahn School of Medicine at Mount Sinai. This work was supported in part by grants from the National Institutes of Health (NIH)/National Institute on Aging (U01AG046170, RF1AG054014, RF1AG057440, R01AG057907, U01AG052411, R01AG062355, U01AG058635, and R01AG068030), NIH/National Institute of Allergy and Infectious Diseases (U01AI111598), NIH/National Institute on Drug Abuse (R01DA043247), NIH/National Institute of Dental and Craniofacial Research (R03DE026814), NIH/National Institute of Diabetes and Digestive and Kidney Diseases (R01DK118243), Department of the Army (W81XWH-15-1-0706), Japan Society for the Promotion of Science KAKENHI (JP16K08637 to K.I.), and Research Funding for Longevity Science from the National Center for Geriatrics and Gerontology, Japan (grants 19-49 to M.S. and 19-7 to K.I.).

**AUTHOR CONTRIBUTIONS**

Conceptualization, B.Z. and E.S.; Investigation, M.W., A.L., M.S., N.D.B., and X.Q.; Formal Analysis, M.W., A.L., N.S., and M.S.; Data Curation, V.H., P.K., M.W., E.W., R.N., Y.-S.W., W.-M.S., Q.S., X.Z., L.G., C.M., E.H., and S.V.; Software, Y.-S.W. and J.Z.; Resources, V.H., V.F., S.N., S.G., and M.E.E.; Validation, L.L., A.Y., M.B.F., P.A.S., S.-M.H., L.Z., J.C., Q.W., H.U.K., J.J., M.-M.Z., K.A., D.C., and Z.Y.; Writing – Original Draft, M.W., A.L., M.S., K.M.I., K.J.B., and B.Z.; Writing – Review & Editing, all authors; Visualization, M.W., A.L., A.Y., and M.S.; Supervision, B.Z., K.J.B., and K.M.I.; Project Administration, B.Z.; Funding Acquisition, B.Z.

**DECLARATION OF INTERESTS**

The authors declare no competing interests.

Received: February 24, 2020

Revised: September 16, 2020

Accepted: October 30, 2020

Published: November 24, 2020

**REFERENCES**

- Abbas, Y.M., Wu, D., Bueler, S.A., Robinson, C.V., and Rubinstein, J.L. (2020). Structure of V-ATPase from the mammalian brain. *Science* **367**, 1240–1246.
- Allen, M., Carrasquillo, M.M., Funk, C., Heavner, B.D., Zou, F., Younkin, C.S., Burgess, J.D., Chai, H.S., Crook, J., Eddy, J.A., et al. (2016). Human whole genome genotype and transcriptome data for Alzheimer's and other neurodegenerative diseases. *Sci. Data* **3**, 160089.
- Allen, M., Wang, X., Burgess, J.D., Watzlawik, J., Serie, D.J., Younkin, C.S., Nguyen, T., Malphrus, K.G., Lincoln, S., Carrasquillo, M.M., et al. (2018). Conserved brain myelination networks are altered in Alzheimer's and other neurodegenerative diseases. *Alzheimers Dement.* **14**, 352–366.
- Alzheimer's Association (2018). 2018 Alzheimer's disease facts and figures. *Alzheimers Dement.* **14**, 367–429.
- Ando, K., Maruko-Otake, A., Otake, Y., Hayashishita, M., Sekiya, M., and Iijima, K.M. (2016). Stabilization of Microtubule-Unbound Tau via Tau Phosphorylation at Ser262/356 by Par-1/MARK Contributes to Augmentation of AD-Related Phosphorylation and A $\beta$ 42-Induced Tau Toxicity. *PLoS Genet.* **12**, e1005917.
- Avramopoulos, D., Szymanski, M., Wang, R., and Bassett, S. (2011). Gene expression reveals overlap between normal aging and Alzheimer's disease genes. *Neurobiol. Aging* **32**, 2319.e27–2319.e34.
- Benjamini, Y., and Hochberg, Y. (1995). Controlling the False Discovery Rate: A Practical and Powerful Approach to Multiple Testing. *J. R. Stat. Soc. B Methodol.* **57**, 289–300.
- Blalock, E.M., Geddes, J.W., Chen, K.C., Porter, N.M., Markesberry, W.R., and Landfield, P.W. (2004). Incipient Alzheimer's disease: microarray correlation analyses reveal major transcriptional and tumor suppressor responses. *Proc. Natl. Acad. Sci. USA* **101**, 2173–2178.
- Braak, H., and Braak, E. (1991). Neuropathological stageing of Alzheimer-related changes. *Acta Neuropathol.* **82**, 239–259.
- Braak, H., Alafuzoff, I., Arzberger, T., Kretschmar, H., and Del Tredici, K. (2006). Staging of Alzheimer disease-associated neurofibrillary pathology using paraffin sections and immunocytochemistry. *Acta Neuropathol.* **112**, 389–404.
- Chung, C.Y.-S., Shin, H.R., Berdan, C.A., Ford, B., Ward, C.C., Olzmann, J.A., Zoncu, R., and Nomura, D.K. (2019). Covalent targeting of the vacuolar H<sup>+</sup>-ATPase activates autophagy via mTORC1 inhibition. *Nat. Chem. Biol.* **15**, 776–785.
- Cohain, A., Divaraniya, A.A., Zhu, K., Scarpa, J.R., Kasarskis, A., Zhu, J., Chang, R., Dudley, J.T., and Schadt, E.E. (2017). Exploring the Reproducibility of Probabilistic Causal Molecular Network Models. *Pac. Symp. Biocomp.* **22**, 120–131.
- Colangelo, V., Schurr, J., Ball, M.J., Pelaez, R.P., Bazan, N.G., and Lukiw, W.J. (2002). Gene expression profiling of 12633 genes in Alzheimer hippocampal CA1: transcription and neurotrophic factor down-regulation and up-regulation of apoptotic and pro-inflammatory signaling. *J. Neurosci. Res.* **70**, 462–473.
- De Jager, P.L., Ma, Y., McCabe, C., Xu, J., Vardarajan, B.N., Felsky, D., Klein, H.-U., White, C.C., Peters, M.A., Lodgson, B., et al. (2018). A multi-omic atlas of the human frontal cortex for aging and Alzheimer's disease research. *Sci. Data* **5**, 180142.
- Deczkowska, A., Keren-Shaul, H., Weiner, A., Colonna, M., Schwartz, M., and Amit, I. (2018). Disease-Associated Microglia: A Universal Immune Sensor of Neurodegeneration. *Cell* **173**, 1073–1081.
- Dobin, A., Davis, C.A., Schlesinger, F., Drenkow, J., Zaleski, C., Jha, S., Batut, P., Chaisson, M., and Gingeras, T.R. (2013). STAR: ultrafast universal RNA-seq aligner. *Bioinformatics* **29**, 15–21.
- Dooneief, G., Marder, K., Tang, M.X., and Stern, Y. (1996). The Clinical Dementia Rating scale: community-based validation of "profound" and "terminal" stages. *Neurology* **46**, 1746–1749.
- Egan, M.F., Kost, J., Tariot, P.N., Aisen, P.S., Cummings, J.L., Vellas, B., Sur, C., Mukai, Y., Voss, T., Furtek, C., et al. (2018). Randomized Trial of Verubecestat for Mild-to-Moderate Alzheimer's Disease. *N. Engl. J. Med.* **378**, 1691–1703.
- Fassio, A., Esposito, A., Kato, M., Saitsu, H., Mei, D., Marini, C., Conti, V., Nakashima, M., Okamoto, N., Olmez Turker, A., et al.; C4RCD Research Group (2018). De novo mutations of the ATP6V1A gene cause developmental encephalopathy with epilepsy. *Brain* **141**, 1703–1718.
- Forgac, M. (2007). Vacuolar ATPases: rotary proton pumps in physiology and pathophysiology. *Nat. Rev. Mol. Cell Biol.* **8**, 917–929.
- Fowler, K.D., Funt, J.M., Artyomov, M.N., Zeskind, B., Kolitz, S.E., and Towfic, F. (2015). Leveraging existing data sets to generate new insights into Alzheimer's disease biology in specific patient subsets. *Sci. Rep.* **5**, 14324.
- Frega, M., van Gestel, S.H., Linda, K., van der Raadt, J., Keller, J., Van Rhijn, J.R., Schubert, D., Albers, C.A., and Nadif Kasri, N. (2017). Rapid Neuronal Differentiation of Induced Pluripotent Stem Cells for Measuring Network Activity on Micro-electrode Arrays. *J. Vis. Exp.* (119).
- Gilbert, L.A., Horbeck, M.A., Adamson, B., Vilalta, J.E., Chen, Y., Whitehead, E.H., Guimaraes, C., Panning, B., Ploegh, H.L., Bassik, M.C., et al. (2014). Genome-Scale CRISPR-Mediated Control of Gene Repression and Activation. *Cell* **159**, 647–661.
- Haroutunian, V., Katsel, P., and Schmeidler, J. (2009). Transcriptional vulnerability of brain regions in Alzheimer's disease and dementia. *Neurobiol. Aging* **30**, 561–573.

- Haure-Mirande, J.-V., Wang, M., Audrain, M., Fanutza, T., Kim, S.H., Heja, S., Readhead, B., Dudley, J.T., Blitzer, R.D., Schadt, E.E., et al. (2019). Integrative approach to sporadic Alzheimer's disease: deficiency of TYROBP in cerebral A $\beta$  amyloidosis mouse normalizes clinical phenotype and complement sub-network molecular pathology without reducing A $\beta$  burden. *Mol. Psychiatry* 24, 431–446.
- Heyman, A., Wilkinson, W.E., Hurwitz, B.J., Helms, M.J., Haynes, C.S., Utley, C.M., and Gwyther, L.P. (1987). Early-onset Alzheimer's disease: clinical predictors of institutionalization and death. *Neurology* 37, 980–984.
- Ho, S.-M., Hartley, B.J., Tew, J., Beaumont, M., Stafford, K., Slesinger, P.A., and Brennan, K.J. (2016). Rapid Ngn2-induction of excitatory neurons from hiPSC-derived neural progenitor cells. *Methods* 101, 113–124.
- Ho, S.M., Hartley, B.J., Flaherty, E., Rajarajan, P., Abdelaal, R., Obiorah, I., Barreto, N., Muhammad, H., Phatnani, H.P., Akbarian, S., and Brennan, K.J. (2017). Evaluating Synthetic Activation and Repression of Neuropsychiatric-Related Genes in hiPSC-Derived NPCs, Neurons, and Astrocytes. *Stem Cell Reports* 9, 615–628.
- Hoffman, G.E., and Schadt, E.E. (2016). variancePartition: interpreting drivers of variation in complex gene expression studies. *BMC Bioinformatics* 17, 483.
- Hoffmann, A., Ziller, M., and Spengler, D. (2018). Childhood-Onset Schizophrenia: Insights from Induced Pluripotent Stem Cells. *Int. J. Mol. Sci.* 19, 3829.
- Honig, L.S., Vellas, B., Woodward, M., Boada, M., Bullock, R., Borrie, M., Hager, K., Andreasen, N., Scarpini, E., Liu-Seifert, H., et al. (2018). Trial of Solanezumab for Mild Dementia Due to Alzheimer's Disease. *N. Engl. J. Med.* 378, 321–330.
- Hornig, J.L., Lin, L.Y., Huang, C.J., Katoh, F., Kaneko, T., and Hwang, P.P. (2007). Knockdown of V-ATPase subunit A (atp6v1a) impairs acid secretion and ion balance in zebrafish (*Danio rerio*). *Am. J. Physiol. Regul. Integr. Comp. Physiol.* 292, R2068–R2076.
- Huan, T., Zhang, B., Wang, Z., Joehanes, R., Zhu, J., Johnson, A.D., Ying, S., Munson, P.J., Raghavachari, N., Wang, R., et al.; Coronary Artery Disease Genome wide Replication and Meta-analysis (CARDIoGRAM) Consortium, International Consortium for Blood Pressure GWAS (ICBP) (2013). A systems biology framework identifies molecular underpinnings of coronary heart disease. *Arterioscler. Thromb. Vasc. Biol.* 33, 1427–1434.
- Iijima, K., Liu, H.P., Chiang, A.S., Hearn, S.A., Konsolaki, M., and Zhong, Y. (2004). Dissecting the pathological effects of human Abeta40 and Abeta42 in Drosophila: a potential model for Alzheimer's disease. *Proc. Natl. Acad. Sci. USA* 101, 6623–6628.
- Jansen, I.E., Savage, J.E., Watanabe, K., Bryois, J., Williams, D.M., Steinberg, S., Sealock, J., Karlsson, I.K., Hägg, S., Athanasiu, L., et al. (2019). Genome-wide meta-analysis identifies new loci and functional pathways influencing Alzheimer's disease risk. *Nat. Genet.* 51, 404–413.
- Johnson, E.C.B., Dammer, E.B., Duong, D.M., Ping, L., Zhou, M., Yin, L., Higginbotham, L.A., Guajardo, A., White, B., Troncoso, J.C., et al. (2020). Large-scale proteomic analysis of Alzheimer's disease brain and cerebrospinal fluid reveals early changes in energy metabolism associated with microglia and astrocyte activation. *Nat. Med.* 26, 769–780.
- Katsiyi, I., Wang, M., Song, W.M., Zhou, X., Zhao, Y., Park, S., Zhu, J., Zhang, B., and Irie, H.Y. (2016). EPRES is a critical regulator of cell proliferation and estrogen signaling in ER+ breast cancer. *Oncotarget* 7, 69592–69605.
- Keenan, A.B., Jenkins, S.L., Jagodnik, K.M., Koplev, S., He, E., Torre, D., Wang, Z., Dohman, A.B., Silverstein, M.C., Lachmann, A., et al. (2018). The Library of Integrated Network-Based Cellular Signatures NIH Program: System-Level Cataloging of Human Cells Response to Perturbations. *Cell Syst.* 6, 13–24.
- Kim, D., Hwang, H.Y., Kim, J.Y., Lee, J.Y., Yoo, J.S., Marko-Varga, G., and Kwon, H.J. (2017). FK506, an Immunosuppressive Drug, Induces Autophagy by Binding to the V-ATPase Catalytic Subunit A in Neuronal Cells. *J. Proteome Res.* 16, 55–64.
- Kuleshov, M.V., Jones, M.R., Rouillard, A.D., Fernandez, N.F., Duan, Q., Wang, Z., Koplev, S., Jenkins, S.L., Jagodnik, K.M., Lachmann, A., et al. (2016). Enrichr: a comprehensive gene set enrichment analysis web server 2016 update. *Nucleic Acids Res.* 44 (W1), W90–7.
- Kunkle, B.W., Grenier-Boley, B., Sims, R., Bis, J.C., Damotte, V., Naj, A.C., Boland, A., Vronskaya, M., van der Lee, S.J., Amie-Wolf, A., et al.; Alzheimer Disease Genetics Consortium (ADGC); European Alzheimer's Disease Initiative (EADI); Cohorts for Heart and Aging Research in Genomic Epidemiology Consortium (CHARGE); Genetic and Environmental Risk in AD/Defining Genetic, Polygenic and Environmental Risk for Alzheimer's Disease Consortium (GERAD/PERADES) (2019). Genetic meta-analysis of diagnosed Alzheimer's disease identifies new risk loci and implicates A $\beta$ , tau, immunity and lipid processing. *Nat. Genet.* 51, 414–430.
- Kwakowsky, A., Calvo-Flores Guzmán, B., Pandya, M., Turner, C., Waldvogel, H.J., and Faull, R.L. (2018). GABA<sub>A</sub> receptor subunit expression changes in the human Alzheimer's disease hippocampus, subiculum, entorhinal cortex and superior temporal gyrus. *J. Neurochem.* 145, 374–392.
- Lake, B.B., Ai, R., Kaeser, G.E., Salathia, N.S., Yung, Y.C., Liu, R., Wildberg, A., Gao, D., Fung, H.-L., Chen, S., et al. (2016). Neuronal subtypes and diversity revealed by single-nucleus RNA sequencing of the human brain. *Science* 352, 1586–1590.
- Lambert, J.-C., Ibrahim-Verbaas, C.A., Harold, D., Naj, A.C., Sims, R., Bellenguez, C., DeStafano, A.L., Bis, J.C., Beecham, G.W., Grenier-Boley, B., et al.; European Alzheimer's Disease Initiative (EADI); Genetic and Environmental Risk in Alzheimer's Disease; Alzheimer's Disease Genetic Consortium; Cohorts for Heart and Aging Research in Genomic Epidemiology (2013). Meta-analysis of 74,046 individuals identifies 11 new susceptibility loci for Alzheimer's disease. *Nat. Genet.* 45, 1452–1458.
- Langfelder, P., Luo, R., Oldham, M.C., and Horvath, S. (2011). Is my network module preserved and reproducible? *PLoS Comput. Biol.* 7, e1001057.
- Law, C.W., Chen, Y., Shi, W., and Smyth, G.K. (2014). voom: Precision weights unlock linear model analysis tools for RNA-seq read counts. *Genome Biol.* 15, R29.
- Legrand, D., Pierce, A., Elass, E., Carpentier, M., Mariller, C., and Mazurier, J. (2008). Lactoferrin structure and functions. *Adv. Exp. Med. Biol.* 606, 163–194.
- Liang, W.S., Dunckley, T., Beach, T.G., Grover, A., Mastroeni, D., Ramsey, K., Caselli, R.J., Kukull, W.A., McKeel, D., Morris, J.C., et al. (2008). Altered neuronal gene expression in brain regions differentially affected by Alzheimer's disease: a reference data set. *Physiol. Genomics* 33, 240–256.
- Liao, Y., Smyth, G.K., and Shi, W. (2014). featureCounts: an efficient general purpose program for assigning sequence reads to genomic features. *Bioinformatics* 30, 923–930.
- Liberzon, A., Subramanian, A., Pinchback, R., Thorvaldsdóttir, H., Tamayo, P., and Mesirov, J.P. (2011). Molecular signatures database (MSigDB) 3.0. *Bioinformatics* 27, 1739–1740.
- Limon, A., Reyes-Ruiz, J.M., and Miledi, R. (2012). Loss of functional GABA(A) receptors in the Alzheimer diseased brain. *Proc. Natl. Acad. Sci. USA* 109, 10071–10076.
- Liu, H., Wei, Z., Dominguez, A., Li, Y., Wang, X., and Qi, L.S. (2015). CRISPR-ERA: a comprehensive design tool for CRISPR-mediated gene editing, repression and activation. *Bioinformatics* 31, 3676–3678.
- Marioni, R.E., Harris, S.E., Zhang, Q., McRae, A.F., Hagenaars, S.P., Hill, W.D., Davies, G., Ritchie, C.W., Gale, C.R., Starr, J.M., et al. (2018). GWAS on family history of Alzheimer's disease. *Transl. Psychiatry* 8, 99.
- Mathys, H., Davila-Velderrain, J., Peng, Z., Gao, F., Mohammadi, S., Young, J.Z., Menon, M., He, L., Abdurrob, F., Jiang, X., et al. (2019). Single-cell transcriptomic analysis of Alzheimer's disease. *Nature* 570, 332–337.
- McKenzie, A.T., Wang, M., Hauberg, M.E., Fullard, J.F., Kozlenkov, A., Keenan, A., Hurd, Y.L., Dracheva, S., Casaccia, P., Roussos, P., and Zhang, B. (2018). Brain Cell Type Specific Gene Expression and Co-expression Network Architectures. *Sci. Rep.* 8, 8868.

- Mertens, J., Reid, D., Lau, S., Kim, Y., and Gage, F.H. (2018). Aging in a Dish: iPSC-Derived and Directly Induced Neurons for Studying Brain Aging and Age-Related Neurodegenerative Diseases. *Annu. Rev. Genet.* 52, 271–293.
- Miller, J.A., Woltjer, R.L., Goodenbour, J.M., Horvath, S., and Geschwind, D.H. (2013). Genes and pathways underlying regional and cell type changes in Alzheimer's disease. *Genome Med.* 5, 48.
- Miller, J.A., Ding, S.-L., Sunkin, S.M., Smith, K.A., Ng, L., Szafer, A., Ebbert, A., Riley, Z.L., Royall, J.J., Aiona, K., et al. (2014). Transcriptional landscape of the prenatal human brain. *Nature* 508, 199–206.
- Millstein, J., Zhang, B., Zhu, J., and Schadt, E.E. (2009). Disentangling molecular relationships with a causal inference test. *BMC Genet.* 10, 23.
- Mirra, S.S., Heyman, A., McKeel, D., Sumi, S.M., Crain, B.J., Brownlee, L.M., Vogel, F.S., Hughes, J.P., van Belle, G., and Berg, L. (1991). The Consortium to Establish a Registry for Alzheimer's Disease (CERAD). Part II. Standardization of the neuropathologic assessment of Alzheimer's disease. *Neurology* 41, 479–486.
- Morley, M., Molony, C.M., Weber, T.M., Devlin, J.L., Ewens, K.G., Spielman, R.S., and Cheung, V.G. (2004). Genetic analysis of genome-wide variation in human gene expression. *Nature* 430, 743–747.
- Morris, J.C. (1993). The Clinical Dementia Rating (CDR): current version and scoring rules. *Neurology* 43, 2412–2414.
- Mostafavi, S., Gaiteri, C., Sullivan, S.E., White, C.C., Tasaki, S., Xu, J., Taga, M., Klein, H.-U., Patrick, E., Komashko, V., et al. (2018). A molecular network of the aging human brain provides insights into the pathology and cognitive decline of Alzheimer's disease. *Nat. Neurosci.* 21, 811–819.
- Murphy, M.P., and LeVine, H., 3rd (2010). Alzheimer's disease and the amyloid-beta peptide. *J. Alzheimers Dis.* 19, 311–323.
- Nehme, R., Zuccaro, E., Ghosh, S.D., Li, C., Sherwood, J.L., Pietilainen, O., Barrett, L.E., Limone, F., Worringer, K.A., Kommineni, S., et al. (2018). Combining NGN2 Programming with Developmental Patterning Generates Human Excitatory Neurons with NMDAR-Mediated Synaptic Transmission. *Cell Rep.* 23, 2509–2523.
- Ng, B., White, C.C., Klein, H.-U., Sieberts, S.K., McCabe, C., Patrick, E., Xu, J., Yu, L., Gaiteri, C., Bennett, D.A., et al. (2017). An xQTL map integrates the genetic architecture of the human brain's transcriptome and epigenome. *Nat. Neurosci.* 20, 1418–1426.
- Ping, L., Duong, D.M., Yin, L., Gearing, M., Lah, J.J., Levey, A.I., and Seyfried, N.T. (2018). Global quantitative analysis of the human brain proteome in Alzheimer's and Parkinson's Disease. *Sci. Data* 5, 180036.
- Pushpakom, S., Iorio, F., Eyers, P.A., Escott, K.J., Hopper, S., Wells, A., Doig, A., Guilliams, T., Latimer, J., McNamee, C., et al. (2019). Drug repurposing: progress, challenges and recommendations. *Nat. Rev. Drug Discov.* 18, 41–58.
- Ridge, P.G., Mukherjee, S., Crane, P.K., and Kauwe, J.S.K.; Alzheimer's Disease Genetics Consortium (2013). Alzheimer's disease: analyzing the missing heritability. *PLoS ONE* 8, e79771.
- Robinson, M.D., McCarthy, D.J., and Smyth, G.K. (2010). edgeR: a Bioconductor package for differential expression analysis of digital gene expression data. *Bioinformatics* 26, 139–140.
- Satoh, J., Yamamoto, Y., Asahina, N., Kitano, S., and Kino, Y. (2014). RNA-Seq data mining: downregulation of NeuroD6 serves as a possible biomarker for Alzheimer's disease brains. *Dis. Markers* 2014, 123165.
- Schadt, E.E., Monks, S.A., Drake, T.A., Lusis, A.J., Che, N., Colinayo, V., Ruff, T.G., Milligan, S.B., Lamb, J.R., Cavet, G., et al. (2003). Genetics of gene expression surveyed in maize, mouse and man. *Nature* 422, 297–302.
- Schadt, E.E., Lamb, J., Yang, X., Zhu, J., Edwards, S., Guhathakurta, D., Sieberts, S.K., Monks, S., Reitman, M., Zhang, C., et al. (2005). An integrative genomics approach to infer causal associations between gene expression and disease. *Nat. Genet.* 37, 710–717.
- Schrode, N., Ho, S.-M., Yamamoto, K., Dobbyn, A., Huckins, L., Matos, M.R., Cheng, E., Deans, P.J.M., Flaherty, E., Barreto, N., et al. (2019). Synergistic effects of common schizophrenia risk variants. *Nat. Genet.* 51, 1475–1485.
- Sekiya, M., Maruko-Otake, A., Hearn, S., Sakakibara, Y., Fujisaki, N., Suzuki, E., Ando, K., and Iijima, K.M. (2017). EDEM Function in ERAD Protects against Chronic ER Proteinopathy and Age-Related Physiological Decline in Drosophila. *Dev. Cell* 41, 652–664.e5.
- Shabalin, A.A. (2012). Matrix eQTL: ultra fast eQTL analysis via large matrix operations. *Bioinformatics* 28, 1353–1358.
- Sigel, E., and Steinmann, M.E. (2012). Structure, function, and modulation of GABA(A) receptors. *J. Biol. Chem.* 287, 40224–40231.
- Song, W.-M., and Zhang, B. (2015). Multiscale Embedded Gene Co-expression Network Analysis. *PLoS Comput. Biol.* 11, e1004574.
- Storey, J.D., and Tibshirani, R. (2003). Statistical significance for genomewide studies. *Proc. Natl. Acad. Sci. USA* 100, 9440–9445.
- Subramanian, A., Tamayo, P., Mootha, V.K., Mukherjee, S., Ebert, B.L., Gillette, M.A., Paulovich, A., Pomery, S.L., Golub, T.R., Lander, E.S., and Mesirov, J.P. (2005). Gene set enrichment analysis: a knowledge-based approach for interpreting genome-wide expression profiles. *Proc. Natl. Acad. Sci. USA* 102, 15545–15550.
- Subramanian, A., Narayan, R., Corsello, S.M., Peck, D.D., Natoli, T.E., Lu, X., Gould, J., Davis, J.F., Tubelli, A.A., Asiedu, J.K., et al. (2017). A Next Generation Connectivity Map: L1000 Platform and the First 1,000,000 Profiles. *Cell* 171, 1437–1452.e17.
- Tian, R., Gachechiladze, M.A., Ludwig, C.H., Laurie, M.T., Hong, J.Y., Nathaniel, D., Prabhu, A.V., Fernandopulle, M.S., Patel, R., Abshari, M., et al. (2019). CRISPR Interference-Based Platform for Multimodal Genetic Screens in Human iPSC-Derived Neurons. *Neuron* 104, 239–255.e12.
- Wang, M., Roussos, P., McKenzie, A., Zhou, X., Kajiwara, Y., Brennand, K.J., De Luca, G.C., Crary, J.F., Casaccia, P., Buxbaum, J.D., et al. (2016). Integrative network analysis of nineteen brain regions identifies molecular signatures and networks underlying selective regional vulnerability to Alzheimer's disease. *Genome Med.* 8, 104.
- Tiscornia, G., Singer, O., and Verma, I.M. (2006). Production and purification of lentiviral vectors. *Nat Protoc* 1, 241–245.
- Wang, M., Beckmann, N.D., Roussos, P., Wang, E., Zhou, X., Wang, Q., Ming, C., Neff, R., Ma, W., Fullard, J.F., et al. (2018). The Mount Sinai cohort of large-scale genomic, transcriptomic and proteomic data in Alzheimer's disease. *Sci. Data* 5, 180185.
- Wang, M., Zhao, Y., and Zhang, B. (2015). Efficient Test and Visualization of Multi-Set Intersections. *Scientific reports* 5, 16923.
- Webster, J.A., Gibbs, J.R., Clarke, J., Ray, M., Zhang, W., Holmans, P., Rohrer, K., Zhao, A., Marlowe, L., Kaleem, M., et al.; NACC-Neuropathology Group (2009). Genetic control of human brain transcript expression in Alzheimer disease. *Am. J. Hum. Genet.* 84, 445–458.
- Yang, S., Liu, Y., Jiang, N., Chen, J., Leach, L., Luo, Z., and Wang, M. (2014). Genome-wide eQTLs and heritability for gene expression traits in unrelated individuals. *BMC Genomics* 15, 13.
- Zhang, B., and Zhu, J. (2013). Identification of key causal regulators in gene networks. In *Proceedings of the World Congress on Engineering II*, pp. 1309–1312.
- Zhang, B., Gaiteri, C., Bodea, L.-G., Wang, Z., McElwee, J., Podtelezhnikov, A.A., Zhang, C., Xie, T., Tran, L., Dobrin, R., et al. (2013a). Integrated Systems Approach Identifies Genetic Nodes and Networks in Late-Onset Alzheimer's Disease. *Cell* 153, 707–720.
- Zhang, Y., Pak, C., Han, Y., Ahlenius, H., Zhang, Z., Chanda, S., Marro, S., Patzke, C., Acuna, C., Covy, J., et al. (2013b). Rapid single-step induction of functional neurons from human pluripotent stem cells. *Neuron* 78, 785–798.
- Zhao, H., Wang, J., and Wang, T. (2018). The V-ATPase V1 subunit A1 is required for rhodopsin anterograde trafficking in Drosophila. *Mol. Biol. Cell* 29, 1640–1651.

- Zhong, Y., Wan, Y.-W., Pang, K., Chow, L.M.L., and Liu, Z. (2013). Digital sorting of complex tissues for cell type-specific gene expression profiles. *BMC Bioinformatics* 14, 89.
- Zhou, X., Wang, M., Katsyv, I., Irie, H., and Zhang, B. (2018). EMUDRA: Ensemble of Multiple Drug Repositioning Approaches to improve prediction accuracy. *Bioinformatics* 34, 3151–3159.
- Zhu, J., Wiener, M.C., Zhang, C., Fridman, A., Minch, E., Lum, P.Y., Sachs, J.R., and Schadt, E.E. (2007). Increasing the power to detect causal associations by combining genotypic and expression data in segregating populations. *PLoS Comput. Biol.* 3, e69.
- Zhu, J., Zhang, B., Smith, E.N., Drees, B., Brem, R.B., Kruglyak, L., Bumgarner, R.E., and Schadt, E.E. (2008). Integrating large-scale functional genomic data to dissect the complexity of yeast regulatory networks. *Nat. Genet.* 40, 854–861.
- Zhu, Y., Paniccia, A., Schulick, A.C., Chen, W., Koenig, M.R., Byers, J.T., Yao, S., Bevers, S., and Edil, B.H. (2016a). Identification of CD112R as a novel checkpoint for human T cells. *J. Exp. Med.* 213, 167–176.
- Zhu, Z., Zhang, F., Hu, H., Bakshi, A., Robinson, M.R., Powell, J.E., Montgomery, G.W., Goddard, M.E., Wray, N.R., Visscher, P.M., and Yang, J. (2016b). Integration of summary data from GWAS and eQTL studies predicts complex trait gene targets. *Nat. Genet.* 48, 481–487.
- Zoncu, R., Bar-Peled, L., Efeyan, A., Wang, S., Sancak, Y., and Sabatini, D.M. (2011). mTORC1 senses lysosomal amino acids through an inside-out mechanism that requires the vacuolar H(+)-ATPase. *Science* 334, 678–683.

## STAR★METHODS

## KEY RESOURCES TABLE

REAGENT or RESOURCE	SOURCE	IDENTIFIER
<b>Antibodies</b>		
Recombinant Anti-ATP6V1A antibody	Abcam	Cat# ab199326; RRID:AB_2802119
Anti-Homer 1 antibody	Synaptic Systems	Cat# 160 003; RRID:AB_887730
PSD-95 antibody	Millipore	Cat# K28/43; RRID:AB_2315221
Anti-Synapsin 1 antibody	Synaptic Systems	Cat# 106 011C3; RRID:AB_993029
Anti-Synaptophysin 1	Synaptic Systems	Cat# 101 002; RRID:AB_887905
VGLUT 1 (vesicular glutamate transporter 1, BNPI, SLC17A7) antibody	Synaptic Systems	Cat# 135 303; RRID:AB_887875
Goat Anti-Human Sox1 Polyclonal antibody	R and D Systems	Cat# AF3369; RRID:AB_2239879
Purified anti-Tubulin beta 3 (TUBB3) antibody	BioLegend	Cat# 801202; RRID:AB_10063408
Anti-β-amyloid, 1-16 antibody, clone 6E10 (mouse ascites)	Biolegend (Signet, Covance)	Cat# SIG-39300-1000; RRID: AB_662809
Mouse monoclonal anti-α-tubulin antibody	Sigma-Aldrich	Cat# T9026; RRID: AB_477593
Anti-Tau, clone Tau 12 antibody	Millipore	Cat# MAB2241; RRID: AB_1977340
Phospho-Tau (Ser202, Thr205) monoclonal antibody (AT8)	Thermo Fisher Scientific	Cat# MN1020; RRID: AB_223647
Mouse anti-Drosophila nervana protein monoclonal antibody	DSHB	Cat# Nrv5F7; RRID: AB_528395
Sheep anti-mouse IgG, whole Ab ECL antibody, HRP conjugated	GE Healthcare	Cat# NA931; RRID: AB_772210
<b>Biological Samples</b>		
Human postmortem brain samples	Mount Sinai/JJ Peters VA Medical Center Brain Bank (MSBB)	<a href="https://icahn.mssm.edu/research/nih-brain-tissue-repository">https://icahn.mssm.edu/research/nih-brain-tissue-repository</a>
<b>Chemicals, Peptides, and Recombinant Proteins</b>		
PTACH [NCH51]	AdipoGen Life Sciences	Cat# AG-CR1-3667; CAS: 848354-66-5
SAHA	MilliporeSigma	Cat# SML0061; CAS: 149647-78-9
NCH-51	MilliporeSigma	Cat# 382185; CAS: 848354-66-5
MS-275	MilliporeSigma	Cat# EPS002; CAS: 209783-80-2
β-Amyloid (1-42) peptide, human	GenScript	Cat# RP10017
<b>Critical Commercial Assays</b>		
ECL Prime Western Blotting Detection Reagents	GE Healthcare	Cat# RPN2236
Hematoxylin Solution, Mayer's	Sigma-Aldrich	Cat# MHS16
Eosin Y solution	Sigma-Aldrich	Cat# HT110132
TRIzol Reagent	Thermo Fisher Scientific	Cat# 15596018
PrimeScript RT reagent Kit with gDNA Eraser	Takara Bio	Cat# RR047A
Thunderbird SYBR qPCR Mix	Toyobo	Cat# QPS-201
Power SYBR® Green RNA-to-CT 1-Step Kit	Thermo Fisher Scientific	Cat# 4389986
Multi-electrode array (MEA)	Axon Biosystems	Cat# M768-MEA-48W
<b>Deposited Data</b>		
Human brain bulk sequencing data	Wang et al., 2018	The Synapse open source platform (syn3159438) <a href="https://www.synapse.org/#!Synapse:syn3159438">https://www.synapse.org/#!Synapse:syn3159438</a>
ATP6V1A knock-down RNA sequencing data	This paper	Gene expression omnibus (GEO): GSE128367

(Continued on next page)

**Continued**

REAGENT or RESOURCE	SOURCE	IDENTIFIER
Experimental Models: Cell Lines		
Two stable human iPSC-derived neuronal progenitor cells (hiPSC-NPCs) expressing dCas9-KRAB (Addgene 99372)	Brennand Lab at Icahn School of Medicine at Mount Sinai	553-S1-1 KRAB and 2607-1-4 KRAB
Human Astrocytes	Scicell	Cat# 1800
Experimental Models: Organisms/Strains		
<i>D. melanogaster</i> : UAS-Aβ42	Iijima et al., 2004	N/A
<i>D. melanogaster</i> : UAS-Tau	Sekiya et al., 2017	N/A
<i>D. melanogaster</i> : UAS-Luciferase RNAi	This paper	N/A
<i>D. melanogaster</i> : elav-GAL4	Bloomington <i>Drosophila</i> Stock Center	BDSC: 458; FlyBase: FBst0000458
<i>D. melanogaster</i> : GMR-GAL4	Bloomington <i>Drosophila</i> Stock Center	BDSC: 1104; FlyBase: FBst0001104
<i>D. melanogaster</i> : UAS-mcherry RNAi	Bloomington <i>Drosophila</i> Stock Center	BDSC: 35785; FlyBase: FBst0035785
<i>D. melanogaster</i> : UAS-Vha68-1 RNAi	Bloomington <i>Drosophila</i> Stock Center	BDSC: 50726; FlyBase: FBst0050726
<i>D. melanogaster</i> : UAS-Vha68-1 RNAi	Bloomington <i>Drosophila</i> Stock Center	BDSC: 42888; FlyBase: FBst0042888
<i>D. melanogaster</i> : Vha68-1 <sup>1</sup>	Bloomington <i>Drosophila</i> Stock Center	BDSC: 82466; FlyBase: FBst0082466
<i>D. melanogaster</i> : UAS-Vha68-2 RNAi	Bloomington <i>Drosophila</i> Stock Center	BDSC: 34582; FlyBase: FBst0034582
<i>D. melanogaster</i> : UAS-Vha68-1 RNAi	Vienna <i>Drosophila</i> Resource Center	VDRC: v46397; FlyBase: FBst0466673
<i>D. melanogaster</i> : UAS-Vha68-2 RNAi	Vienna <i>Drosophila</i> Resource Center	VDRC: v110600; FlyBase: FBst0482165
Oligonucleotides		
qRT-PCR primers for <i>D. melanogaster</i> , see Table in STAR Methods	This paper	N/A
gRNA sequences to repress ATP6V1A expression, see Table in Experimental Model and Subject Details	This paper	N/A
qRT-PCR primers for ATP6V1A and β-Actin, see Table in Experimental Model and Subject Details	This paper	N/A
Recombinant DNA		
lentiGuide-Hygro-mTagBFP2	Ho et al., 2017	Addgene Plasmid #99374
lenti-EF1a-dCas9-KRAB-Puro	Ho et al., 2017	Addgene Plasmid #99372
pLV-TetO-hNGN2-eGFP-Neo	This paper	N/A
Software and Algorithms		
R/limma (v3.38.3)	Bioconductor	<a href="https://www.bioconductor.org/packages/release/bioc/html/limma.html">https://www.bioconductor.org/packages/release/bioc/html/limma.html</a>
STAR aligner (v2.5.2a)	Dobin et al., 2013	<a href="https://github.com/alexdobin/STAR">https://github.com/alexdobin/STAR</a>
featureCounts (v1.6.3)	Liao et al., 2014	<a href="http://subread.sourceforge.net/">http://subread.sourceforge.net/</a>
MEGENA (v1.3.6)	Song and Zhang 2015	<a href="https://cran.r-project.org/web/packages/MEGENA/index.html">https://cran.r-project.org/web/packages/MEGENA/index.html</a>
SMR (v0.712)	Zhu et al., 2016b	<a href="https://cnsgenomics.com/software/smr/">https://cnsgenomics.com/software/smr/</a>
R/SuperExactTest (v1.0.6),	Wang et al., 2015	<a href="https://cran.r-project.org/web/packages/SuperExactTest/index.html">https://cran.r-project.org/web/packages/SuperExactTest/index.html</a>
R/NetWeaver (v0.0.5)	CRAN	<a href="https://cran.r-project.org/web/packages/NetWeaver/index.html">https://cran.r-project.org/web/packages/NetWeaver/index.html</a>
R/msigdb (v0.1.4)	github	<a href="https://github.com/mw201608/msigdb">https://github.com/mw201608/msigdb</a>
R/MatrixEQTL (v2.2)	Shabalin, 2012	<a href="https://cran.r-project.org/web/packages/MatrixEQTL/index.html">https://cran.r-project.org/web/packages/MatrixEQTL/index.html</a>
Prism7	GraphPad	<a href="https://www.GraphPad.com">https://www.GraphPad.com</a>
RIMBANET		<a href="https://icahn.mssm.edu/research/genomics/about/resources">https://icahn.mssm.edu/research/genomics/about/resources</a>
CRISPR-ERA web tool	Liu et al., 2015	<a href="http://crispr-era.stanford.edu">crispr-era.stanford.edu</a>

**RESOURCE AVAILABILITY****Lead Contact**

Further information and requests for resources and reagents should be directed to and will be fulfilled by the Lead Contact, Bin Zhang ([bin.zhang@mssm.edu](mailto:bin.zhang@mssm.edu)).

**Materials Availability**

Stable human iPSC-derived neuronal progenitor cells (hiPSC-NPCs) expressing dCas9-KRAB utilized in this study can be requested through Dr. Kristen Brennand ([kristen.brennand@mssm.edu](mailto:kristen.brennand@mssm.edu)) upon Material Transfer Agreement.

*Drosophila* lines developed in this study and the related reagents can be requested through Koichi M. Iijima ([ijimakm@ncgg.go.jp](mailto:ijimakm@ncgg.go.jp)) or Michiko Sekiya ([mmsk@ncgg.go.jp](mailto:mmsk@ncgg.go.jp)).

**Data and Code Availability**

The human postmortem sequencing data are available via the AD Knowledge Portal (<https://adknowledgeportal.synapse.org>). The AD Knowledge Portal is a platform for accessing data, analyses, and tools generated by the Accelerating Medicines Partnership (AMP-AD) Target Discovery Program and other National Institute on Aging (NIA)-supported programs to enable open-science practices and accelerate translational learning. The data, analyses and tools are shared early in the research cycle without a publication embargo on secondary use. Data is available for general research use according to the following requirements for data access and data attribution (<https://adknowledgeportal.synapse.org/DataAccess/Instructions>).

For access to content described in this manuscript see: <https://www.synapse.org/#!Synapse:syn23519511>

**EXPERIMENTAL MODEL AND SUBJECT DETAILS****Human Postmortem Brain Tissue Samples**

The MSBB-AD cohort included 364 human brains accessed from the Mount Sinai/JJ Peters VA Medical Center Brain Bank (MSBB) ([Haroutunian et al., 2009](#); [Wang et al., 2016, 2018](#)). The postmortem interval (PMI) is ranged from 75 to 1800 minutes (min), with a mean of 436.5 min, a median of 312 min, and a standard deviation of 323 min. Each donor and corresponding brain sample was assessed for multiple cognitive, medical, and neurological features, including mean plaque density, Braak staging for neurofibrillary tangles (NFT) ([Braak et al., 2006](#); [Braak and Braak, 1991](#)), clinical dementia rating (CDR) ([Morris, 1993](#)), and neuropathology scale as determined by the Consortium to Establish a Registry for Alzheimer's Disease (CERAD) protocol ([Mirra et al., 1991](#)). Mean plaque density was calculated as the average of neuritic plaque density measures in five regions, including middle frontal gyrus, orbital frontal cortex, superior temporal gyrus, inferior parietal lobule and occipital cortex. Because many of the donors were nursing home residents and some experienced dementia that was more severe than that captured by the 0-3 scale of CDR, we used the validated version of the "extended" CDR which adds "profound" (CDR = 4) and "terminal" (CDR = 5) to the original 5 point scale ([Dooneief et al., 1996](#); [Heyman et al., 1987](#)). These four cognitive/neuropathological traits were scored as semiquantitative features ranging from normal to severe disease stages, reflecting the continuum and divergence of pathologic and clinical diagnoses of AD beyond a simple case-control classification. Donor brains with no discernable neuropathology (by CERAD assessment) or only neuropathologic feature characteristic of LOAD were selected from over 2,000 brains in the MSBB. Please refer to [Table S1](#) for a summary of the subject demographic information. Since we focus on the common mechanisms between male and female, sex has been adjusted in the present RNA-seq data preprocessing (detailed below). We plan to assess the gender difference in AD at the molecular level in future studies.

**Human Induced Pluripotent Stem Cell Lines**

iPSC-derived NPCs (2607-1-4, 553-S1-1; both male) were generated by Dr. Kristen Brennand Lab at the Icahn School of Medicine at Mount Sinai. iPSCs (NSB553, NSB2607) were originally from the National Institute of Mental Health (NIMH) childhood-onset schizophrenia (COS) cohort. Human Astrocytes (Cat #1800) were purchased from ScienCell Research Laboratories, Inc. All hiPSC research was conducted under the oversight of the Institutional Review Board (IRB) and Embryonic Stem Cell Research Overview (ESCRO) committees at the Icahn School of Medicine at Mount Sinai (ISSMS). Informed consent was obtained from all skin cell donors as part of a study directed by Judith Rapoport MD at the National Institute of Mental Health (NIMH).

**Drosophila Models**

Flies were maintained in standard cornmeal media at 25°C. Transgenic fly lines carrying UAS-A $\beta$ 42 and UAS-Tau were previously described ([Iijima et al., 2004](#); [Sekiya et al., 2017](#)). The *elav*-GAL4 (#458), GMR-GAL4 (#1104), UAS-mcherry RNAi (#35785), UAS-Vha68-1 RNAi (#50726 and #42888), Vha68-1<sup>1</sup> (#82466), and UAS-Vha68-2 RNAi (#34582) were obtained from the Bloomington *Drosophila* Stock Center. UAS-Vha68-1 RNAi (#46397) and UAS-Vha68-2 RNAi (#110600) were obtained from the Vienna *Drosophila* Resource Center. The UAS-Luciferase RNAi Transgenic flies were generated by PhiC31 integrase-mediated transgenesis systems (Best Gene Inc.). Genotypes and ages of all flies used in this study are provided in figure legends. Experiments were performed using age-matched male flies and genetic background of the flies was controlled. For example, for RNAi experiments,

we crossed virgin females from *elav-GAL4; UAS-A $\beta$ 42* (double transgenic flies expressing A $\beta$ 42 pan-neuronally) and males from *UAS-Vha68-1* RNAi lines (experimental group) or a *UAS-mcherry* RNAi line with the same genetic background as the RNAi lines (control group). The resultant offspring from each cross has the same hybrid genetic background and these flies were used for the experiments.

## METHOD DETAILS

### The MSBB-AD cohort data quality control and preprocessing

As described previously (Wang et al., 2018), we generated whole genome sequencing (WGS) as well as RNA-sequencing (RNA-seq) data in four brain regions from majority of the cases, including Brodmann area 10 (frontal pole, BM10-FP), Brodmann area 22 (superior temporal gyrus, BM22-STG), Brodmann area 36 (parahippocampal gyrus, BM36-PHG) and Brodmann area 44 (inferior frontal gyrus, BM44-IFG). Through an iterative QC and adjustment procedure which examined the genetic similarity between every pair of molecular profiles across different data types and multiple brain regions, we identified mislabeled or duplicated molecular profiles (Wang et al., 2018). In this paper, we excluded all mislabeled samples for downstream analyses. For RNA-seq, we further removed RNA-seq libraries with RNA integrity number (RIN) less than 4 or rRNA rate larger than 5%, and then selected one with the best sequencing coverage for the duplicated sequencing libraries (see Table S1 for demographics of the final set of RNA-seq samples). In the QCed dataset, the RIN is ranged from 4 to 10, with a mean of 6.8, a median of 6.6, and a standard deviation of 1.5. To avoid any artificial regional difference, the data from all four brain regions were merged and processed together. Genes with at least 1 count per million (CPM) reads in at least 10% of the libraries were considered expressed and hence retained for further analysis; others were removed. After filtering, 23,201 genes were retained. The gene read counts data were normalized using the trimmed mean of M-values normalization (TMM) (Robinson et al., 2010) method in the R/Bioconductor edgeR package to adjust for sequencing library size differences. It is critical to identify and correct for confounding factors in the RNA-seq data. For this purpose, we used R/Bioconductor variancePartition (Hoffman and Schadt, 2016) package to evaluate the impact of multiple sources of biological and technical variation in gene expression experiments, including sex, race, age, RIN, postmortem interval (PMI), sequencing batch, rate of exonic reads, and rate of rRNA reads, together with the four cognitive/neuropathological features described in the main text. Figure S1 illustrates the principal component analysis and variance partition analysis of the RNA-seq data. We found sequencing batch, exonic rate and brain donor contributed to the most variance. The contributions from the cognitive/neuropathological variables were similar and ranked in the middle among all the variables. While rRNA rate generally did not explain a large proportion of variation, it contributed more overall variance than did sex and race. Therefore, in addition to the usual confounding factors that are commonly corrected in postmortem brain gene expression data, including batch, sex, race, age, RIN, and PMI, we included exonic rate and rRNA rate as covariates. As there were more than 30 batches, the batch was first regressed out with a random effect model using variancePartition (Hoffman and Schadt, 2016), and the other covariates were corrected by linear regression in R.

### Differential expression analysis

For each neuropathological/cognitive trait in each brain region, we grouped the samples into multiple disease severity stages and compared the gene expression between every two groups using limma's moderated t test analysis (Law et al., 2014). Specifically, for CDR, samples were classified into cognitive normal (nondemented) (CDR = 0), mild cognitive impairment (MCI) (CDR = 0.5), and demented (CDR  $\geq$  1). For Braak score, samples were classified into normal (NL) when Braak score  $\leq$  2, and AD when Braak score  $>$  2. For plaque mean density (PlaqueMean), samples were classified into 4 categories, namely normal (PlaqueMean = 0), mild ( $0 <$  PlaqueMean  $\leq$  6), medium ( $6 <$  PlaqueMean  $\leq$  12), and severe (PlaqueMean  $>$  12) groups. With CERAD score, two types of samples classification schemes were used. First, samples were classified into normal (NL) (CERAD = 1), definite AD (CERAD = 2), probable AD (CERAD = 3) and possible AD (CERAD = 4). Second, samples were classified into two groups, normal (NL) when CERAD = 1 and AD when CERAD  $>$  1. To adjust for multiple tests, false discovery rate (FDR) was estimated using the Benjamini-Hochberg (BH) method (Benjamini and Hochberg, 1995). Genes showing at least 1.2-fold change (FC) and FDR adjusted P values less than 0.05 were considered significant. The gene showing the largest fold increase in all comparisons is *LTF* (lactotransferrin) (3.8-fold, adjusted P value 3.9E-5) as identified in BM36-PHG with respect to the PlaqueMean trait. Lactotransferrin is a major component of mammals' innate immune system, protecting from direct antimicrobial activities to anti-inflammatory and anticancer activities (Legrand et al., 2008). *NEUROD6* (neuronal differentiation factor 6) showed the largest fold decrease across all contrasts (0.34-fold, adjusted P value = 6.3E-9). *NEUROD6* encodes a transcription activator that may be involved in neuronal development and differentiation. Downregulation of *NEUROD6* in LOAD has been consistently observed in several previous studies (Fowler et al., 2015; Satoh et al., 2014).

To systematically validate the present DEG signatures of LOAD related traits, we assembled public ALOD signatures from 10 studies, including Zhang et al. (2013a), Webster et al. (2009), Satoh et al. (2014), Miller et al. (2013), Avramopoulos et al. (2011), Liang et al. (2008), Colangelo et al. (2002), Blalock et al. (2004), Mostafavi et al. (2018), and Allen et al. (2018). Then we evaluated the overlap between the present DEGs and these previously published LOAD signatures using the Fisher's exact test (FET). We observed a highly significant overlap (adjusted P value up to 1.0E-100) for almost every differential contrast in public LOAD signatures as illustrated in Figure S3. We note that when up- and downregulated DEGs were separated, we observed significant enrichments in consistent directions with respect to expression changes in this analysis. The relatively mild enrichment for the signatures in BM10-FP and

BM44-IFG was due to the small number of genes identified in the two regions. To further investigate if the present expression signatures from bulk tissue RNA-seq tend to reflect cell-type changes, we collected a set of cell type-specific DEGs identified from a recent single-nuclei RNA-seq (snRNA-seq) analysis of LOAD postmortem brains (Mathys et al., 2019). Here, we used cell type-specific DEGs computed from the cell-level model. Figure S4 shows the FET of the enrichment between our bulk-tissue DEGs and the cell type-specific DEGs detected in Ex (excitatory neurons), In (inhibitory neurons), Oli (oligodendrocytes), Opc (oligodendrocyte progenitor cells), Ast (astrocytes), or Mic (microglia) in brains with LOAD pathology. We observed a strong preservation of both up- and downregulated genes in a cell type-specific manner. These results demonstrate a robust set of LOAD related gene signatures across all brain regions profiled.

To understand what biological processes are represented in the DEGs, we tested these signatures for enrichment of gene ontology (GO) and canonical functional pathway gene sets from the Molecular Signatures Database (MSigDB) gene annotation database v6.1 (Liberzon et al., 2011; Subramanian et al., 2005). For convenience, the MSigDB gene set collections have been assembled into an R package called “msigdb” which is publicly available from <https://github.com/mw201608/msigdb>. We overlapped the DEGs with the MSigDB gene sets and computed the fold enrichment (FE) and P value significance using the algorithms described in the next section “Overlap and functional enrichment analysis.” The top enriched terms are summarized in Figure S5, and the full list of significant enrichments is provided in Table S3.

### Overlap and functional enrichment analysis

Functional enrichment analysis (or overlap test) P value was calculated using the hypergeometric test (equivalent to the Fisher’s exact test, FET) assuming the sets of genes, such as DEGs, were identically independently sampled from all the genome-wide genes detected by RNA-seq except otherwise specifically stated. Fold enrichment (FE) was calculated as the ratio between observed overlap size and expected overlap size. To control for multiple testing, we employed the Benjamini-Hochberg (BH) approach (Benjamini and Hochberg, 1995) to constrain the FDR. For GO and pathway enrichment analysis, we utilized the functional gene set collections from the Molecular Signatures Database (MSigDB) v6.1 (Liberzon et al., 2011; Subramanian et al., 2005).

For brain cell type marker gene enrichment analysis, we focused on the 5 major brain cell types, i.e., neurons, microglia, astrocytes, oligodendrocytes and endothelial, and for each type used the top 500 ranked consensus cell type-specific genes derived from a meta-analysis of 5 cell type-specific or single cell RNA-seq datasets (McKenzie et al., 2018).

### Cell-type deconvolution analysis

We performed cell-type deconvolution analysis to estimate the major brain cell-type proportions using a Digital Sorting Algorithm (DSA) (Zhong et al., 2013). From the normalized gene expression matrix and cell-type marker genes, DSA estimates the cell type frequencies by solving a restricted linear model. Here we focused on 5 major brain cell types (i.e., neurons, astrocytes, oligodendrocytes, microglia, and endothelial), and for each type, we used 5 markers which were top ranked for cell type specificity according to our recent brain cell type specific transcriptomic analysis (McKenzie et al., 2018). As illustrated in Figure S27, the diseased brains showed progressive neuronal loss as the severity advanced, which was accompanied by the increase of glia cells. The neuronal cell frequencies were negatively correlated with disease traits in all brain regions. For example, the Spearman correlation between neuronal frequencies and CDR ranged from -0.18 to -0.41 (P value = 3.1E-3 ~ 2.6E-10). The proportion of microglia cells was not estimable, likely due to the low sensitivity in estimating cells with low abundance.

### MEGENA gene coexpression network analysis

For MEGENA (Song and Zhang, 2015), Pearson correlation coefficients (PCCs) were computed for all gene pairs in every brain region. Significant PCCs at a permutation-based FDR cutoff of 0.05 were ranked and iteratively tested for planarity to grow a Planar Filtered Network (PFN) by using the PMFG algorithm. Multiscale Clustering Analysis (MCA) was conducted with the resulting PFN to identify coexpression modules at different network scale topology. We identified 475, 527, 441 and 423 coherent gene expression modules in BM10-FP, BM22-STG, BM36-PHG and BM44-IFG, respectively (Table S4). To annotate the potential biological functions associated with the modules, we performed MSigDB gene set enrichment analysis using FET as described above. Most of these modules (53.9% to 67.3%) were enriched for MSigDB GO/pathway gene sets (adjusted P value < 0.05) (Table S5), indicating that MEGENA is capable of capturing data-drive biologically meaningful, context-dependent co-regulation signals beyond what is represented in canonical pathways from ontology databases. For simplicity, modules were annotated by the top enriched functional category. It is noted that MEGENA modules are formed in a hierarchy with parent-child relationships which can be illustrated by a sunburst style plot.

To prioritize the gene modules with respect to their association to LOAD pathology, we applied an ensemble ranking metric (Wang et al., 2016) across multiple feature types (Figures 2B and 2C), including 1) correlations between module eigengenes (i.e., the first principal component of module gene expression profile) and cognitive/pathological traits associated with LOAD, and 2) enrichment for the DEG signatures identified above. A more complete description of the information used to rank the modules is included in Table S6. The ranking of the top 25 MEGENA modules are illustrated in Figure 2B, with all of the top modules coming from the BM36-PHG region.

We annotated the potential cell type specificity of the modules by evaluating enrichment of brain cell type-specific marker as described above, with the enrichment statistics summarized in Table S6. We found many top-ranked modules were enriched for

neuronal or microglia-specific cell types (Figures 2B and 2C) based on enrichment analysis of cell type-specific markers of five major brain cell types, including neurons, microglia, endothelial, astrocytes and oligodendrocytes (McKenzie et al., 2018). To test whether the top-ranked neuronal system modules reflected distinct neuronal subtypes, we utilized a large-scale single-nucleus RNA-seq data of inhibitory and excitatory neurons isolated from six different regions of the human cerebral cortex (Lake et al., 2016). We downloaded the preprocessed gene expression data (transcripts per million, TPM) from this published study and further selected genes with at least 1 TPM in at least 10% of the cells in one subtype. Then we computed genes which showed differential expression between cell types using limma's moderated t test analysis (Law et al., 2014). Source of brain region origination of the cells was incorporated as a covariate. While the original study identified up to 16 different sub-types of neurons, we focused on the genes differentiate between the two major neuron cell types (i.e., inhibitory and excitatory). We called genes inhibitory neuron-enriched if they presented at least 4-fold higher expression in inhibitory neuron cells than in excitatory neuron cells with FDR < 0.05, and excitatory neuron-enriched if they presented at least 4-fold higher expression in excitatory neuron cells than in inhibitory neuron cells with FDR < 0.05. As a result, we identified 1008 excitatory neuron-enriched genes and 413 inhibitory neuron-enriched genes. Lastly, we overlapped the cell type-enriched genes with the top-ranked neuronal modules and found that module M64 was overrepresented with inhibitory neuron-enriched genes while M6, M87, M65, M236, M62, and M252 were overrepresented with excitatory neuron-enriched genes (Table S7).

Interestingly, a number of LOAD GWAS risk genes were present in our top-ranked modules, including *MEF2C* (M62), *CELF1*, *MADD*, *PLD3*, *PTK2B*, and *ZCWPW1* (M6), and *APP* and *SORL1* (M64), *CLU* and *CR1* (M17), and *APOE*, *CASS4*, *CD33*, *HLA-DRB1/HLA-DRB5*, *INPP5D*, *MS4A4A/MS4A6A* and *TREM2* (M153 and M14). The mechanism underlying the clustering of GWAS risk genes in the top modules is unknown. One possible reason is that they express in common cell types.

### Network connectivity preservation analysis

We investigated the preservation of global MEGENA co-expression network between our MSBB RNA-seq data and the ROSEMAP RNA-seq data (Mostafavi et al., 2018), using the network-based statistics calculated by the modulePreservation function from WGCNA (Langfelder et al., 2011). Since modulePreservation does not allow a single gene to be present in multiple modules as in MEGENA, we considered each gene-module combination as a unique gene and renamed the genes, then created a new expression matrix accordingly. We reported module preservation with the main network-based statistics Zsummary.pres and followed the original software guideline to denote a module as strongly preserved ( $Z\text{summary}.pres > 10$ ), weakly to moderately preserved ( $2 < Z\text{summary}.pres < 10$ ), or not preserved ( $Z\text{summary}.pres < 2$ ).

### Discovery of region-wide expression quantitative trait loci (eQTLs)

Given the well-established relationships between gene expression and interactions with genetic and environment factors, we mapped expression quantitative trait loci (eQTLs) by integrating the RNA-seq and WGS-based Single-nucleotide polymorphism (SNP) genotype data. SNPs significantly associated with gene expression traits were identified using the MatrixEQTL package (Shabalin, 2012). Significant SNPs (eSNPs) were classified into *cis*- and *trans*-acting elements according to whether they are located within 1-MB from the gene or not. At a conservative Bonferroni corrected P value threshold of 0.05 (equivalent to a nominal P value cutoff of 3.0E-10), 1214, 922, 762, and 1054 genes were identified to be regulated by at least one proximal SNP within 1 million base (Mb) from the gene, termed *cis*-eSNP, in BM10-FP, BM22-STG, BM36-PHG, and BM44-IFG, respectively (Table S9). For simplicity, we refer to genes with significant eSNPs as eGenes and a significant association between a SNP and a gene as an eSNP-eGene pair. By such a definition, 126,799, 101,705, 92,336, and 112,139 *cis*-eSNP-eGene pairs were identified in BM10-FP, BM22-STG, BM36-PHG and BM44-IFG, respectively. It is noted that there are redundant eSNPs for the same eGene due to linkage disequilibrium (LD) of the SNPs. Figure S7 shows the overlap of these *cis*-eSNP-eGene pairs among the four brain regions. 66.1% to 90.7% of the *cis*-eSNP-eGene pairs identified in one brain region were also detected in at least one other brain region. In addition, 71,298 *cis*-eSNP-eGene pairs from 548 unique genes were shared by all 4 brain regions.

We detected 20,657, 14,011, 14,766, and 17,125 *trans*-eSNP-eGene pairs from BM10-FP, BM22-STG, BM36-PHG and BM44-IFG, respectively. For each brain region, 28.5 to 70.1% of the *trans*-eSNP-eGene pairs identified were also detected in at least one other brain region (Figure S7). We grouped Bonferroni corrected significant SNPs within a 5-Mb interval into a single peak because of insufficient resolution to break LD over such narrow windows (Morley et al., 2004; Yang et al., 2014). Each peak was represented by the most significant eSNP in the window, referred to as the lead eSNP, for a given *trans*-eGene. We identified 2,411, 1,965, 1,392 and 2,460 *trans*-eQTL peaks from BM10-FP, BM22-STG, BM36-PHG and BM44-IFG, respectively. Early eQTL studies noted the existence of master *trans*-genetic regulators, which we refer to as eQTL hotspots (Schadt et al., 2003), that regulate many genes throughout the human genome. We defined *trans*-eQTL hotspots as those peaks associated with 10 or more *trans*-eGenes. At this definition, we identified 24, 12, 2 and 27 *trans*-eQTL hotspots from BM10-FP, BM22-STG, BM36-PHG and BM44-IFG, respectively (Figure S8 and Table S10), with nine *trans*-eQTL hotspots shared between 2 or 3 brain regions (Figure S9). Each of these hotspots were associated with 10 to 36 *trans*-eQTL genes. The hotspot associated with the greatest number of *trans*-eQTL genes (36 genes) was located at a region near 84.4-Mb on chromosome 17 (lead eSNP rs10264300) in BM44-IFG. SNP rs10264300 is 181 kilobases upstream of AC003984.1 (a long intergenic noncoding RNA, lncRNA) and 82.5 kilobases downstream of AC093716.1 (a pseudogene gene). About half (16) of the gene targets of this hotspot encode enzyme binding proteins (6.4-FE, adjusted FET = 7.1E-5) (Table S11). Interestingly, synaptic pathway genes were enriched for the targets of a hotspot near lead

SNP rs34072069 on chromosome 10 in BM10-FP (17.1-FE, adjusted FET p = 4.9E-6). SNP rs34072069 is 44.5 kilo-bases (KB) upstream of RNU6-535P (a small nuclear RNA gene) and 1.9 KB downstream of RP11-385N23.1 (an antisense gene).

We evaluated whether any modules were enriched for our *cis*-eGenes. Twelve MEGENA modules were significantly enriched for *cis*-eQTL genes (Table S12), among which four were associated with GTPase mediated signal transduction (one from each brain region (> 17.9-FE, adjusted FET p < 3.5E-11) and three were associated with transferase activity (one from each of 3 brain regions except BM44-IFG; > 10.9-FE, adjusted FET p < 2.3E-4). We noted that the genes in the GTPase mediated signal transduction modules were concentrated in chromosome region 17q21, while the transferase activity modules in chromosome region 8p23, suggesting the genetic regulation of these modules by common eQTLs shared by multiple brain regions.

We attempted to replicate eQTLs in an independent LOAD postmortem brain RNA-seq dataset generated from the ROSMAP cohort (Mostafavi et al., 2018), which is, to our knowledge, the largest sampled RNA-seq based eQTL analysis of LOAD in a single brain region (494 individuals). *Cis*-eQTLs were identified for 3,388 genes from the ROSMAP cohort as published by Ng et al. (2017). However, since no *trans*-eQTLs were reported for the ROSMAP cohort (Ng et al., 2017), we focused on the replication of *cis*-eQTLs in this paper, and particularly the *cis*-eSNP-eGene pairs that were available in both datasets. To avoid including dependent signals induced by LD among adjacent SNPs, only the associations comprising the top SNP for each eGene were included in the replication rate calculations. To circumvent the statistical power difference caused by different sample sizes (494 individuals in ROSMAP and 215~261 individuals across the present four brain regions), we first followed Ng et al. (2017) to assess the replication rate of LOAD brain *cis*-eSNP-eGene discovered in the ROSMAP cohort in our dataset using the  $\pi_1$  statistic (Storey and Tibshirani, 2003), which estimated the proportion of reported ROSMAP *cis*-eSNP-eGene pairs that are also significant in the current dataset based on their P value distribution.  $\pi_1$  values of the ROSMAP *cis*-eSNP-eGene pairs were 0.698, 0.674, 0.637, and 0.670 in the present brain regions BM10-FP, BM22-STG, BM36-PHG, and BM44-IFG, respectively. These values were significantly larger than their empirical null mean of 0.025~0.038 from 10,000 random samples of P values of associations that did not overlap with the eQTLs (one-tailed P value < 0.0001). Analogously, we applied the same  $\pi_1$  statistic to estimate the replication rate of the present region-wide eQTLs in the ROSMAP data but were unsuccessful because the P value distributions of the MSBB *cis*-eSNP-eGene pairs were truncated (maximum P value = 0.92) with majority of the values approaching 0 (93% to 96% were less than 0.05) in the ROSMAP data. In fact, 81.6%, 84.3%, 89.0% and 82.5% of the *cis*-eSNP-eGene pairs identified in BM10-FP, BM22-STG, BM36-PHG, and BM44-IFG, respectively, were also called genome-wide significant in the ROSMAP data, indicating most of the present *cis*-eQTLs were replicated, while the rest 11~18% are likely novel *cis*-eQTLs or false positives. Nonetheless, these results indicate marked common genetic regulation occurring across different brain regions.

### Integrating eQTL, gene expression traits, and LOAD GWAS loci to identify causal LOAD genes

We did not observe significant enrichment for *cis*-eGenes in the LOAD-related DEGs or brain cell type-specific markers in each brain region (with less than 8% of the *cis*-eGenes detected as DEGs and less than 6% of the DEGs detected as *cis*-eGenes, FET P value > 0.1), suggesting a lack of detectable *cis*-genetic regulation among the genes dysregulated in LOAD brains. However, for the most strongly associated SNPs across all *cis*-eGenes, we observed a significant enrichment (p < 0.05) for LOAD genetic association signals based on the SNP-level summary statistics from a recent meta-analysis of AD GWAS (Kunkle et al., 2019), compared to random samples of SNPs of the same size (Table S13). In this analysis, we first selected the strongly associated SNPs across all *cis*-eGenes and then extracted their SNP-level LOAD GWAS chi-square statistics from the AD GWAS study (Kunkle et al., 2019). The mean chi-square statistics among those *cis*-eSNPs was compared to a null distribution which was obtained by randomly sampling the same number of SNPs for 10,000 times. Enrichment P value was computed as the proportion of randomly sampled SNP sets with mean chi-square values larger than the observed one.

Moreover, *cis*-eQTLs overlapped the genome-wide significant LOAD GWAS SNPs at GWAS risk loci *HLA-DRB1/HLA-DRB5* and *ZCWPW1*. To aid in the identification of candidate causal genes in these GWAS loci, we applied the summary-data-based mendelian randomization (SMR) (Zhu et al., 2016b) method to test if the effects of the top GWAS SNPs in the *HLA-DRB1/HLA-DRB5* and *ZCWPW1* loci were mediated by gene expression associated with eQTL coincident with the GWAS loci. By integrating eQTLs and GWAS signals, we aimed to prioritize the most possible functional relevant genes underlying the effects of causal variants on the disease phenotype at two LOAD GWAS risk loci. We reformatted the eQTL results and AD GWAS SNP-level summary statistics (Kunkle et al., 2019) data files in accordance to the manual of the SMR software (Zhu et al., 2016b). Then we ran region-wide SMR analysis using the default parameter. For each locus, we used the region-wide rather than the experiment-wise significance threshold because we were interested in gene discovery for each specific locus in each brain region than the joint analysis of all regions as a whole. For the genes with significant association by the SMR test, the heterogeneity in dependent instruments (HEIDI) test (Zhu et al., 2016b) was further employed to distinguish whether the association was caused by pleiotropy of the same causal variant underlies the disease risk, or due to linkage of distinct variant to the one causal to the disease.

Figure S10 shows the GWAS and eQTL P value profiles at the *HLA-DRB1/HLA-DRB5* locus as well as the SMR test results in four brain regions. In a 2-Mb region centered on *HLA-DRB1*, there were 11~12 genes with *cis*-eQTLs across the four brain regions. For example, 12 genes were found to have *cis*-eQTLs in BM10-FP; the SMR test was significant for *HLA-DRB5* at a Bonferroni corrected P value threshold of 4.5E-3, while the gene *HLA-DRB1* was not significant. To distinguish whether the significant association in the SMR test was caused by pleiotropy that gene expression and the trait affected by the same underlying causal variant, or due to linkage that the top associated *cis*-eQTL being in LD with two distinct causal variants, one affecting the disease trait and the other

affecting the gene expression, we further performed the heterogeneity in dependent instruments (HEIDI) test as in [Zhu et al. \(2016b\)](#). *HLA-DRB5* showed no significant heterogeneity by the HEIDI test ( $P$  value  $> 0.05$ ), supporting the null hypothesis that there is a single causal variant affecting both gene expression and disease trait phenotype. In summary, we found that *HLA-DRB5* passed both SMR and HEIDI tests in all four brain regions, *HLA-DQA1* passed both SMR and HEIDI tests in BM36-PHG and BM22-STG, *HLA-DRB1* passed both SMR and HEIDI tests in BM36-PHG, and *HLA-DQB2* passed both SMR and HEIDI tests in BM44-IFG ([Figure S10](#)), suggesting that *HLA-DQA1*, *HLA-DQB2*, *HLA-DRB1*, and especially *HLA-DRB5* are the most plausible functionally relevant targets underlying the GWAS hits at this locus.

At a 2-Mb region surrounding gene *ZCWPW1*, there were 3 to 6 genes with *cis*-eQTLs across the different brain regions ([Figure S11](#)). *ZCWPW1* did not pass the SMR test, indicating that our data do not support that the expression of *ZCWPW1* mediates the causal effect on the disease phenotype. However, an adjacent gene *PVRIG* passed the SMR test in BM36-PHG. *PVRIG*, also known as *CD112R*, encodes a protein that recruits tyrosine phosphatases for signal transduction and could act as a coinhibitory receptor that suppresses T cell receptor (TCR) signaling ([Zhu et al., 2016a](#)). We noted that none of the genes passed the HEIDI test, rejecting the null hypothesis that there is a single causal variant affecting both gene expression and disease trait phenotype.

The present analysis shows that eQTL prioritized genes may not be necessarily the genes nearest to the peak SNP as reported in the association studies. Further independent replications and experimental validations are required to verify the potential causal relationships inferred from the current integrative analysis.

### Bayesian probabilistic causal network inference and key driver analysis

To construct Bayesian probabilistic causal Network (BN), we made use of genetic perturbations in biological systems (e.g., WGS SNP variants) and known transcription factor (TF)-target relationships from the ENCODE project as prior for inferring regulatory relationships between genes. In the causal network construction, the TFs are allowed to be parent node of their target genes; but targets are inhibited to be parent nodes of their TFs. To infer gene regulatory relationship from genetic data, we first computed *cis*- and *trans*-eQTLs for each expression trait using WGS-based SNP variants as described above and then employed a causal inference to infer the causal probability between gene pairs associated with the same eQTL. Since a gene pair associated with the same eSNP may be causally regulated from one to another or independently regulated by a genetic factor in LD with the eSNP, we derived genetic priors under two scenarios. In the first scenario, genes with *cis*-acting eSNP could be parent nodes of genes with *trans*-acting eSNP, but the opposite direction was not permitted following previous practices ([Zhu et al., 2007, 2008](#)). In the second scenario where the genes are both *cis*-regulated or both *trans*-regulated, either gene can be the parent node of the other and hence there are two possible directions. For the latter scenario, we applied a formal causality inference test (CIT) ([Millstein et al., 2009](#); [Schadt et al., 2005](#)) to distinguish the causal/reactive and independent relationships between the gene expression traits by modeling the gene pair and associated eSNP with a “chain” of mathematical conditions. For each trio (a gene pair and one eSNP), CIT will compute the probability of the causal “chain” in which one gene is mediating the causal impact of the eSNP to the other gene when the regulatory direction is allowed ([Millstein et al., 2009](#)). In cases that the gene pair is associated with multiple common eSNPs, the individual causality test  $P$  values of each trio were aggregated using Fisher’s method to make a collective call for the gene pair. As the conservative Bonferroni corrected  $P$  value threshold of 0.05 in the eQTL analysis gave a very limited number of gene pairs associated with common SNPs, we relaxed the cutoff to a BH FDR adjusted  $P$  value threshold of 0.05 to increase the pool of potential causal-reactive gene pairs. The causal relationships thus inferred by CIT were combined with TF-target relationships, and together they were used as structure priors for building a brain region-wide BN from all 23,201 expressed genes through a Monte Carlo Markov Chain (MCMC) simulation based procedure ([Zhu et al., 2007](#)). Following previous practices ([Zhu et al., 2007, 2008](#)), we employed a network averaging strategy in which 1,000 networks were generated by this MCMC process starting with different random structure, and links that appeared in more than 30% of the networks were used to define a final consensus network. If loops were present in the consensus network, the weakly supported link involved in a loop was removed to ensure the final network structure was a directed acyclic graph.

From the region-wide BNs, we identified network key drivers that are predicted to modulate a large number of downstream nodes, and as a result, modulate the state of the network, by using the Key Driver Analysis (KDA) ([Huan et al., 2013](#); [Zhang et al., 2013a](#); [Zhang and Zhu, 2013](#)). Here we loaded all the BN nodes as input in the KDA and hence the resulting key drivers were called global network key drivers which were different from the pathway (such as the neuronal modules) context dependent key drivers described later. There were 1,545, 1,418, 1,454, and 1,371 global key drivers in the BNs from BM10-FP, BM22-STG, BM36-PHG and BM44-IFG, respectively. Strikingly, the key drivers were significantly conserved across the region-wide BNs, with any two BNs sharing a significant number of key drivers ( $7.2 < \text{FE} \leq 8.2$ , FET  $P$  values  $< 1.0\text{E-}320$ ) while 325 key drivers were shared across four BNs (929.4-FE, Super Exact Test  $P$  value  $< 1.0\text{E-}320$ ) ([Figure S12](#)), demonstrating a high-degree of conservation of the regulatory architecture in the brain regions we profiled. This is in line with previous study that replication of edge-to-edge is strongly dependent on the sample size while highly connected key driver nodes tend to be more stable than network edges ([Cohain et al., 2017](#)).

To perform a comprehensive validation of the BN topological structures and the global key drivers that modulate them, we downloaded a library of 2,460 single gene perturbation signatures curated at the Enrichr server ([Kuleshov et al., 2016](#)). After filtering for central nervous system (CNS) or immune system-related studies and requiring the perturbed genes to be present in the current dataset, we obtained 649 signatures from 320 studies for 287 unique perturbed genes. These gene perturbation signatures were collected from the gene expression omnibus (GEO) database, and the original experiments were conducted in a diversity of

conditions (different cell lines or tissues from different species). 66 of these perturbed genes were global key drivers in at least one of our four brain region-wide BNs. For each of these perturbed global key drivers, we examined whether the experimental perturbation signature was predicted by our networks by examining whether the genes in these signatures were enriched for genes in the network neighborhood of the key driver in our BNs (examining genes that were within a path length of 6 of the key driver gene). Despite the vast heterogeneity of the gene perturbation studies compared to the present human postmortem brain tissues used to generate our data for the region-wide BNs, 50 to 60% of the key driver perturbation signatures were enriched in the network neighborhoods of the corresponding key drivers across the four region-wide BNs (Figure 3B). The significance levels of the enrichments are observed to increase as path lengths defining the network neighborhoods are increased, given the BNs were sparse, with a limited number of neighboring nodes closer to the key driver gene, which serves to reduce the power to make such detections, especially in the context of multiple testing. In contrast, the proportion of significantly enriched perturbation signatures decreased to 20~30% in the network neighborhood of non-driver genes.

We further performed KDA on the top-ranked MEGENA neuronal modules to identify their master regulators. In this analysis, we projected the module genes onto the region-wide BN and searched for key driver genes whose network neighborhood were enriched for the module genes. Different from the global key drivers described above, here the key drivers were context dependent, in this case, related to neuronal system subnetworks. This yielded 42 unique key driver genes across 9 modules (Table S14) predicted to be the network key drivers. 10 key drivers were root nodes in the BM36-PHG BN without parental nodes. To further verify the root node status beyond a single region-based network, we sought to integrate information from all 4 region-wide BNs to build a union BN that contained a union of directed links from all 4 individual BNs by following previous practices (Haure-Mirande et al., 2019; Katsyv et al., 2016). Like region-wide BNs, loops in the union BN were broke by removing the weakly supported links. Two key drivers, ATP6V1A (module M64), and GABRB2, (module M62), remained as root nodes in this union BN.

Gamma-aminobutyric acid (GABA) is the major inhibitory neurotransmitter in the mammalian brain and GABA type A (GABA-A) receptors mediate the inhibition effect (Sigel and Steinmann, 2012). GABA-A receptors form pentameric complexes by combinations of more than 10 subunits and marked functional remodeling GABA-A receptors, including change of subunit composition and reduced expression of principal subunits, had been observed in LOAD brains (Limon et al., 2012). In this paper, we observed a significant downregulation of the subunits  $\alpha$ 1-6,  $\beta$ 2-3 and  $\gamma$ 2-3 in diseased brains compared to control (Table S2). It has been reported that GABA-A  $\beta$ 2 (GABRB2) subunit, paralleled with some other subunits like  $\alpha$ 1,  $\alpha$ 2,  $\alpha$ 5,  $\beta$ 3, and  $\gamma$ 2, showed altered brain region- and cell layer-specific expression (Kwakowsky et al., 2018). Its protein level was significantly decreased in the dentate gyrus stratum moleculare, but increased in the stratum oriens and stratum radiatum of the hippocampal CA2 region, and stratum radiatum of the hippocampal CA3 region (Kwakowsky et al., 2018), indicating a region-dependent up- or down- dysregulation of this gene in LOAD.

### Drug repositioning of AD signature in neural progenitor cells

To identify existing drugs that can restore the molecular expression change in the LOAD brains, we performed a drug repositioning analysis using EMUDRA (Zhou et al., 2018), which provides a novel computational algorithm to match disease signatures and drug-induced signatures. For this purpose, we downloaded drug-treated gene expression profiles (level 3 data of quantile-normalized and log2 transformed expression levels from human iPSC-derived neural progenitor cells (NPCs) from the Library of Integrated Network-Based Cellular Signatures (LINCS) program (Keenan et al., 2018; Subramanian et al., 2017). After removing probes sets mapping to multiple genes or without known gene annotation, the remaining data were adjusted for batch effects using linear regression. Mean expression level of multiple probe sets matching to the same gene was used as the expression level of that gene. For each drug, the transcriptome-wide expression difference between drug-treated and DMSO-treated gene expression profiles was considered the drug signature. We then matched each of the drug signatures to the LOAD signature using EMUDRA to find drugs that could reverse the LOAD signature. For LOAD signature, we used the DEGs between CERAD definite AD and normal control brains in the BM36-PHG region (3,000 up- and 2,076 downregulated genes). In total, 3,629 drug signatures were analyzed and ranked. We further prioritized the top-ranked drugs that can increase ATP6V1A mRNA expression in the NPCs.

### Lentivirus generation

Third-generation VSV.G pseudotyped HIV-1 lentiviruses (below) were produced by polyethylenimine (PEI, Polysciences #23966-2)-transfection of HEK293T cells and packaged with VSVG-coats using established methods (Tiscornia et al., 2006). Lentiviral FUW-M2rtTA (Addgene #20342), pLV-TetO-hNGN2-eGFP-neo (TBD), lentiGuide-Hygro-mTagBFP2, and 6 lentiGuide vectors with insertion were generated. Physical titration of lentivirus was performed by qPCR (qPCR Lentivirus Titration Kit, ABM good #LV900). Lentiviruses were then used to transduce cells according to their physical titer as described below, calculated through the company's website (<https://www.abmgood.com/High-Titer-Lentivirus-Calculation.html>).

### gRNA design and cloning for *in vitro* functional validation of ATP6V1A deficit in NGN2-neurons

gRNA design and cloning were performed as previously described (Ho et al., 2017). Specifically, 6 gRNA candidates for ATP6V1A were designed by using CRISPR-ERA web tool ([crispr-era.stanford.edu](http://crispr-era.stanford.edu)): 6 gRNA sequences targeting promoter region (between +658 bps and transcription start site) of ATP6V1A. For lentiviral cloning, the gRNA sequences were inserted into

LentiGuide-Hygro-mTagBFP2 (Addgene #99374). Oligonucleotides encoding gRNA sequences were annealed, diluted and then ligated into BsmBI-digested LentiGuide vectors as previously described (Ho et al., 2017). Sanger sequencing using U6 promoter confirmed all constructions.

Oligo ID	Location	gRNA (E,S score)	gRNA Sequence (5'-3')
<b>ATP6V1i_#1-1</b>	+260	#1 (20,0)	5'-CACCGGCGGGGAACGACCACACTTGG
<b>ATP6V1i_#1-2</b>			5'-AAACCCAAGTGTGGTCGTTCCGCC
<b>ATP6V1i_#2-1</b>	+101	#2 (20,0)	5'-CACCGGGCGACCGGTAACCTGGCGAG
<b>ATP6V1i_#2-2</b>			5'-AAACCTCGCCAGTTACCGGTGCGCCC
<b>ATP6V1i_#3-1</b>	+94	#3 (20,0)	5'-CACCGGGTGAGCGGGGACCGGTAAC
<b>ATP6V1i_#3-2</b>			5'-AAACGTTACCGGTGCGCGCTCACCC
<b>ATP6V1i_#4-1</b>	+14	#4 (20,-2)	5'-CACCGGGGGAAAGTCCTCAGCTGCAC
<b>ATP6V1i_#4-2</b>			5'-AAACGTGCAGCTGAGGACTTCCCC
<b>ATP6V1i_#5-1</b>	+266	#5 (20,-2)	5'-CACCGGTGGTCGTTCCGCTACTT
<b>ATP6V1i_#5-2</b>			5'-AAACAAGTAGCGGGAACGACCACC
<b>ATP6V1i_#6-1</b>	+658	#6 (15,0)	5'-CACCGGATGTTCACGTGCTTCGGAT
<b>ATP6V1i_#6-2</b>			5'-AAACATCCGAAGCACGTAAACATCC

### hiPSC-NPC culture and NGN2 neuronal differentiation

Two stable hiPSC-derived neuronal progenitor cells (hiPSC-NPCs) (553KRAB and 2607KRAB) expressing dCas9-KRAB (Addgene 99372) were generated as previously described (Ho et al., 2017) and cultured in hNPC media (DMEM/F12 (Life Technologies #10565), 1x N2 (Life Technologies #17502-048), 1x B27-RA (Life Technologies #12587-010), 20 ng/ml FGF2 (Life Technologies), and 0.3 µg/mL puromycin) on Matrigel (Corning, #354230). NPCs at full confluence ( $1\text{-}1.5 \times 10^7$  cells/well of a 6-well plate) were dissociated with Accutase (Innovative Cell Technologies) for 5 mins, spun down (5 mins X 1000 g), resuspended and seeded onto Matrigel-coated plates at  $3\text{-}5 \times 10^6$  cells/well. Media was replaced every two days for four to seven days until next split.

At day -2, NPCs were seeded as  $4\text{-}6 \times 10^5$  cells/well in a 24-well plate coated with Matrigel (coverslips are put in a plate and coated with Matrigel for immunostaining). At day -1, cells were transduced with rTA, pLV-Teto-hNGN2-eGFP-Neo and ATP6V1Ai gRNA or empty lentiguide-Hygro-mTagBFP2 (Addgene 99374) lentiviruses via spinfection. Medium was switched to non-viral medium 3 hours post-spinfection. At Day 0, 1 µg/ml dox was added to induce NGN2-expression. At Day 1, transduced hiPSC-NPCs were treated with corresponding antibiotics to the lentiviruses (300 ng/ml puromycin for dCas9-effectors-Puro, 1 mg/ml G-418 for hNGN2-eGFP-neo and 1 mg/ml HygroB for lentiguide-Hygro-mTagBFP2) in order to increase the purity of transduced NPCs. At day 3, NPC medium was switched to neuronal medium (Brainphys (StemCell Technologies, Inc., #05790), 1x N2 (Life Technologies #17502-048), 1x B27-RA (Life Technologies #12587-010), 1 µg/ml Natural Mouse Laminin (Life Technologies), 20 ng/ml BDNF (Peprotech #450-02), 20 ng/ml GDNF (Peprotech #450-10), 500 µg/ml Dibutyryl cyclic-AMP (Sigma #D0627), 200 nM L-ascorbic acid (Sigma #A0278)) including 1 µg/ml Dox, along with antibiotic withdrawal. 50% of the medium was replaced with fresh neuronal medium (lacking dox once every second day. At day 11, full medium change withdrew residual dox completely. At day 13, NGN2-neurons were treated with 200 nM Ara-C to reduce the proliferation of non-neuronal cells in the culture, followed by half medium change by day 17. At Day 17, Ara-C was completely withdrawn by full medium change, followed by half medium changes until the neurons were fixed or harvested around day 21-24.

### Primary human astrocyte (pHA) co-culture

Commercially available pHAs (ScienCell, #1800; isolated from fetal female brain) were thawed onto a matrigel-coated 100 mm culture dish with commercial astrocyte medium (ScienCell, #1801). While their growing, the astrocytes were fed with fresh astrocyte medium for five days according to the company's manual. Upon their confluence at 90%, astrocytes were detached by TrypLE™ (Thermo Fisher Scientific, #12605010), spun down (200 g x 5 mins), resuspended with freezing medium (astrocyte medium supplemented with 10% DMSO) and banked in liquid nitrogen.

At day -2, pHAs were thawed and seeded onto the matrigel-coated 100 mm culture dish and cultured for five days. At day 3, cells were detached, spun down and resuspended with Brainphys basal medium supplemented with Antibiotic-Antimycotic (Anti/Anti; Thermo Fisher Scientific, #15240062) and 2% fetal bovine serum (FBS; Sigma, F4135). Then, cells were split as  $1 \times 10^5$  cells / well on a matrigel-coated coverslip. At day 5, pHAs were fed by full medium change with the Brainphys medium (2% FBS + Anti/Anti). At day 7, neurons were split on the pHAs with neuronal medium supplemented with 2% FBS.

Until day 7, NGN2-neurons, when co-cultured with pHAs, were prepared as described above. At day 7, NGN2-neurons were gently detached with Accutase, spun down (1000 g x 5 mins) and resuspended in neuronal medium supplemented with 2% FBS. After counting cells with a hemacytometer, NGN2-neurons were seeded on astrocyte culture at different cell densities according to assays

( $4.5\text{-}6 \times 10^5$  cells/coverslip for presynaptic ICC and  $7.5\text{-}10 \times 10^4$  cells/well for MEA). Since day 9, the culture was fed by half medium change along with treatment with 2  $\mu\text{M}$  Ara-C until the day of analysis.

We focused on the phenotypic analyses in 21-day-old *NGN2*-induced neurons because it is the earliest time point that we (Ho et al., 2016; Schröde et al., 2019) and others (Frega et al., 2017; Nehme et al., 2018; Zhang et al., 2013b) consistently observe spontaneous synaptic activity across donors. *ATP6V1A* is robustly expressed across developmental stage in the human brain (Figure S15A; Miller et al., 2014). Overexpression of *NGN2* induces glutamatergic neurons with robust expression of glutamatergic genes and excitatory post-synaptic currents (EPSCs) by 21 days (Zhang et al., 2013b) across dozen of donors in our laboratory (Figure 4). In hiPSC-derived *NGN2*-neurons, *ATP6V1A* expression is elevated within 14-days of neuronal induction and remains relatively stable thereafter (21, 28, and 35 days) tested (Figure S15B; Tian et al., 2019).

### RNA sequencing data processing of *ATP6V1A* KD and A $\beta$ -treated neurons

RNA Sequencing libraries were prepared using the Kapa Total RNA library prep kit. Paired-end sequencing reads (100bp) were generated on a NovaSeq platform. Raw reads were aligned to hg19 using STAR aligner (v2.5.2a) and gene-level expression were quantified by featureCounts (v1.6.3) based on Ensembl GRCh37.70 annotation model. Genes with over 1 count per million (CPM) in at least 1 sample were retained. After filtering, the raw read counts were normalized by the voom function in limma and differential expression was computed by the moderated t test implemented in limma.

We examined the GO/pathways impacted by *ATP6V1A* deficit and/or A $\beta$  treatment by employing the Gene Set Enrichment Analysis (GSEA) (Subramanian et al., 2005), a weighted enrichment test using all genes devoid of setting a hard threshold to select significant ones since there was a relatively small number of DEGs in KD-V versus WT-V passing the stringent multiple-test correction and no individual gene met the threshold for statistical significance between the A $\beta$ -treated cells and the vehicle-treated cells. In these analyses, the t test statistics from the differential expression contrast were used to rank genes in the GSEA. Permutations (up to 100,000 times) were used to assess the GSEA enrichment P value.

### **ATP6V1A** KD and A $\beta$ -treatment synergistic effect analysis from the RNA-seq data

The synergistic effect between *ATP6V1A* KD and A $\beta$ -treatment was performed by limma's linear model analysis with formula: Gene expression ~ Sample treatment. The coefficients, standard deviations and correlation matrix were calculated, using *contrasts.fit*, in terms of the comparisons of interest. Empirical Bayes moderation was applied using the *eBayes* function to obtain more precise estimates of gene-wise variability. P values were adjusted for multiple hypotheses testing using false discovery rate (FDR) estimation, and differentially expressed genes were determined as those with an estimated FDR  $\leq 5\%$ , unless stated otherwise. Details about the synergistic effect analysis method were described in Schröde et al. (2019).

The expected additive effect was modeled through addition of the individual comparisons: (KD-V versus WT-V) + (WT-A $\beta$  versus WT-V). The synergistic effect was modeled by subtraction of the additive effect from the combinatorial perturbation comparison: (KD-A $\beta$  versus WT-V) - (KD-V versus WT-V) - (WT-A $\beta$  versus WT-V). Fitting of this model for differential expression gives genes that show a difference in the differential expression computed for the additive model and that computed for the combinatorial perturbation. However, interpretation of the resulting DEGs depends on several factors, such as the direction of fold change (FC) in all three models. To identify genes of interest, namely those whose magnitude of change is larger in the combinatorial perturbation versus the additive model, we categorized all genes by the direction of their change in both models and their log<sub>2</sub>(FC) in the synergistic model. First, log<sub>2</sub>(FC) standard errors (SE) were calculated for all samples. Genes were then grouped into 'positive synergy' if their FC was larger than SE and 'negative synergy' if smaller than -SE. If the corresponding additive model log<sub>2</sub>(FC) showed the same or no direction, the gene was classified as "more" differentially expressed in the combinatorial perturbation than predicted. 2925 genes were computed to be in this category (1152 more down, 1773 more up).

Pathway enrichment was performed on a curated subset of the MAGMA collection using the limma package camera function, which tests if genes in a given pathway category are ranked highly in comparison to other genes in terms of differential expression, while accounting for inter-gene correlation. Due to the small sample size in this study and moderate fold changes in A $\beta$  treatment, changes in gene expression may be small and distributed across many genes. However, similar to previous studies more powerful enrichment analyses in the limma package were used. These evaluate enrichment based on genes that are not necessarily genome-wide significant, and identify sets of genes for which the distribution of t-statistics differs from expectation. Over-representation analysis (ORA) was performed when subsets of DEGs were of interest, such as the synergistic 'more up' and 'more down' genes. The genes of interests were ranked by -log<sub>10</sub> (p value) and enrichment was performed against a background of all expressed genes using the WebGestaltR package.

### Quantitative reverse transcription PCR (qRT-PCR) of *ATP6V1A*

Quantitative reverse transcription PCR (qRT-PCR) was performed as previously described (Ho et al., 2017). Specifically, cell cultures were harvested with Trizol and total RNA extraction was carried out following the manufacturer's instructions. Quantitative transcript analysis was performed using a QuantStudio 7 Flex Real-Time PCR System with the Power SYBR Green RNA-to-Ct Real-Time qPCR Kit (all Thermo Fisher Scientific). Total RNA template (25 ng per reaction) was added to the PCR mix, including primers listed below. qPCR conditions were as follows; 48°C for 30 min, 95°C for 10 min followed by 40 cycles (95°C for 15 s, 60°C for 60 s). All qPCR data is collected from at least 3 independent biological replicates of one experiment. Data analyses were performed using GraphPad PRISM 6 software.

Gene_id	Primer_FWD	Primer_REV	Length
ATP6V1A	GAGATCCTGTACTTCGCACTG	GGGATGTAGATGCTTGGGTC	130
β-Actin	TGTCCCCAACTTGAGATGT	TGTGCACTTTATTCAACTGGTC	109

### Preparation of cell lysates and western blotting

Cells were rinsed with ice-cold phosphate-buffered saline (PBS), pelleted, and lysed in RIPA Lysis and Extraction Buffer (Thermo Fisher Scientific, #89900) containing Halt Protease and Phosphatase Inhibitor Cocktail (Thermo Fisher Scientific, #78440). Alternatively, MSBB BM36 brain samples were homogenized with similar methods. Samples were sonicated for 1 minute then centrifuged at 13,000 × rpm for 10 min. The supernatant was collected, and total protein concentration was determined using Quick Start™ Bradford Protein Assay (Bio-Rad, 5000201) following the manufacturer's instructions.

Western blotting was performed as previously described using antibodies listed in the table below. Images were captured and quantified using the Odyssey® Imaging Systems (LI-COR, Inc.).

Item Name	Catalog	Species	WB	IF
ATP6V1A	ab199326	Rabbit	1:1000	-
Homer 1	160 003	Rabbit	1:1000	1:200-500
PSD-95	clone K28/43	Mouse IgG2	1:500	1:1000
Synapsin 1	106 011	Mouse	1:1000	1:500
Synaptophysin 1	101 002	Rabbit	1:2000	1:500
VGLUT 1	135 303	Rabbit	1:2000	1:1000
SOX1	AF3369	Goat	-	1:100
TUJ1	801202	Mouse IgG2a	1:1000	1:1000

### Immunofluorescence and microscopy

NGN2-neurons (on coverslips) were washed with PBS and fixed with 4% paraformaldehyde (PFA) at pH 7.4 for 10 mins, room temperature. Then, fixative solution was replaced with PBS. After 3 times wash, NGN2-neurons were incubated with blocking solution (0.1% Tween-20, 0.5% bovine serum albumin in PBS) for 1 hour, room temperature. The blocking solution was aspirated and replaced with the same solution with primary antibodies listed above and incubated overnight at 4°C. Neurons were then incubated with secondary antibodies in blocking solution, for 1 hour at room temperature, followed by PBS-washing 3 times.

20 µL of AquaPolymount mounting solution (Polysciences Inc., #18606-20) per coverslip was placed onto each microscopic slide and the coverslips were gently mounted onto the slides with the neuron side facing down. Mounted coverslips were air-dried for two days at ambient temperature. For synaptic ICC imaging, images were acquired using a confocal microscope (LSM 780, Zeiss) with a 63 × objective lens. These puncta analyses were assessed using NIH ImageJ. Total synapsin1 and homer1 puncta number per image were divided by that image's respective MAP2-positive area in order to calculate synapsin1 and homer1 puncta counts normalized to MAP2 levels. Data from 3 independent experiments were analyzed using GraphPad PRISM 6 software.

### β-Amyloid preparation and treatment

Human β-amyloid (1-42) peptide was purchased from GenScript (#RP10017, 1 mg; MW: 4514.1). 1 mg of lyophilized Aβ was completely dissolved in 221.5 µL of 1,1,1,3,3-Hexafluoro-2-propanol (Hexafluoroisopropanol, HFIP, Sigma, 52517-10ML). 10 µL of 1 mM Aβ-HFIP (0.045 mg) in 0.5 mL EP tube was dried overnight in the hood. Dried Aβ were centrifuged for 1 h at 1,000 × g, 4°C, and stored at –80°C. Before use, allow Aβ to come to room temperature. 5 mM Aβ-DMSO stock was prepared using 2 µL fresh dry Dimethyl sulfoxide (DMSO, Sigma, D5879) to 0.045 mg Aβ. Aβ-DMSO solution was sonicated for 10 min in a bath sonicator. 21-day isogenic pairs of ATP6V1A-manipulated NGN2-neurons were exposed to 5 µM Aβ for 24 hours and then used in qPCR, MEA assays, and RNA sequencing.

### Multi-electrode array (MEA)

In order to evaluate electrical activity of NGN2-neurons by MEA, density-matched isogenic NGN2-neuronal populations, co-cultured with pHAs, were prepared as described above. Specifically, at day 3, pHAs were split as 17,000 cells/well in a Matrigel-coated 48W MEA plate (Axion Biosystems, M768-tMEA-48W) and maintained as above. At day 7, NGN2-neurons were detached, spun down and seeded on the pHAs culture. Outer space of each well in the plate was filled up with autoclaved/deionized water to minimize the evaporation of marginal wells (“edge effect”) during long-term culture. Half volume of neuronal medium (supplemented with 2% FBS) was replaced with fresh medium including 200 nM Ara-C from day 9 until the end of MEA recording. Electrical activity of neurons was daily-recorded during day 14~24. On the recording day, the plate was loaded into the Axion Maestro MEA reader (Axion Biosystems).

Recording was performed via AxIS 2.4 for 10 mins. Quantitative analysis of the recording was exported as a Microsoft excel sheet. Data were analyzed using GraphPad PRISM 6 software.

### Electrophysiology

For whole-cell patch-clamp recordings,  $1.0\text{--}1.5 \times 10^4$  human astrocytes were first seeded onto Matrigel-coated 12-mm glass coverslips in 24-well plates, and then seeded with  $1.0 \times 10^5$  neurons after  $\sim 5$  days. Neurons were recorded at 4–5 weeks following dox-induction, with media exchange every 3–4 days. Cells were visualized on a Nikon inverted microscope equipped with fluorescence and Hoffman optics. Neurons were recorded with an Axopatch 200B amplifier (Molecular Devices), digitized at 10 kHz using a Digidata 1320a (Molecular Devices) and filtered between 1–10 kHz, using Clampex 10 software (Molecular Devices). Series resistance compensation was applied (70%–100%). Patch pipettes were pulled from borosilicate glass electrodes (Warner Instruments) to a final tip resistance of 3–5 M $\Omega$  using a vertical gravity puller (Narishige). Neurons were bathed in artificial cerebral spinal fluid (ACSF) containing (in mM): NaCl, 119; CaCl<sub>2</sub>, 2; KCl, 2.5; MgCl<sub>2</sub>, 1.3; d-glucose, 11; NaHCO<sub>3</sub>, 26.2; NaPO<sub>4</sub>, 1, at a pH of 7.4. The internal patch solution contained (in mM): K-d-gluconate, 140; NaCl, 4; MgCl<sub>2</sub>, 2; EGTA, 1.1; HEPES, 5; Na<sub>2</sub>ATP, 2; sodium creatine phosphate, 5; Na<sub>3</sub>GTP, 0.6, at a pH of 7.4. Osmolarity was 290–295 mOsm. All chemicals were purchased from Sigma-Aldrich Co. (St. Louis, MO). Neurons were chosen at random using DIC or with BFP+ expression to identify neurons with gRNA. For current-clamp recordings, neurons were hyperpolarized to  $\sim -80$  mV, and then current steps applied to evoke activity. Spikelets were defined as small, outward spikes with a peak amplitude of less than 25 mV and occurred at voltages positive to threshold ( $\sim -30$  mV). In voltage-clamp recordings, voltage steps were applied from  $-80$  mV to  $+50$  mV (10 mV increments) to elicit voltage-gated ionic currents. All recordings were made at room temperature ( $\sim 22^\circ\text{C}$ ). Difference between sodium current densities at 0 mV were tested for statistical significance ( $p < 0.05$ ) using a Student's t test between control ( $n = 18$ ) and ATP6V1A KD neurons ( $n = 17$ ), pooling over two experimental replicates. Voltages are corrected for a junction potential of  $\sim -15$  mV. Values are reported as mean  $\pm$  SEM.

### ATP6V1A orthologs in fly

According to the DIOPt (DRSC Integrative Ortholog Prediction Tool), *Drosophila* Vacuolar H<sup>+</sup> ATPase 68kD subunit 1 (*Vha68-1*, CG12403) and *Vha68-2* (CG3762) are the best orthologs of human ATP6V1A proteins (DIOPt score 13 for both genes). *Vha68-1* and ATP6V1A exhibit 83% identity and 91% similarity in primary amino acid sequence, and have similar size (614 and 617 amino acids, respectively), while *Vha68-2* and ATP6V1A exhibit 83% identity and 92% similarity in primary amino acid sequence with similar size (614 and 617 amino acids, respectively).

### RNA extraction and quantitative real time PCR analysis

More than 25 flies for each genotype were collected and frozen. Heads were mechanically isolated, and total RNA was extracted using TRIzol Reagent (Thermo Fisher Scientific) according to the manufacturer's protocol with an additional centrifugation step (16,000  $\times g$  for 10 min) to remove cuticle membranes prior to the addition of chloroform. Total RNA was reverse-transcribed using PrimeScript RT-PCR kit (TaKaRa Bio), and qRT-PCR was performed using Thunderbird SYBR qPCR Mix (Toyobo) on a CFX96 real time PCR detection system (Bio-Rad Laboratories). The average threshold cycle value was calculated from at least three replicates per sample. Expression of genes of interest was standardized relative to GAPDH1. Primer sequences used in this study are provided below.

Fly	Human	Forward primer sequence (5' to 3')	Reverse primer sequence (5' to 3')
<i>Gapdh</i>	<i>GAPDH1</i>	GACGAAATCAAGGCTAACGGTCG	AATGGGTGTCGCTGAAGAAGTC
<i>Vha68-1*</i>	<i>ATP6V1A</i>	ACTACGCACCAAGGTCAAGG	CTTGCCACTTCCAGGGTCA
<i>Vha68-1**</i>	<i>ATP6V1A</i>	ACCTCTTCCGTGGAACCTTG	GCAGTTGTGGACACCTTTGG
<i>Vha68-2</i>	<i>ATP6V1A</i>	CAAATATGGACGTGCTTCGC	CCGGATCTCCGACAGTTACG
<i>Eaat1</i>	<i>SLC1A2</i>	TGCTCTGTTCATCGCCCAAT	CGACGGCTATGATGAGGGAC
<i>VGlut</i>	<i>SLC17A6-8</i>	TTCATCGCTCCAAGTTCCC	GCTGGATAGGTAACGCCCTC
<i>Atp<math>\alpha</math></i>	<i>ATP1A1-3</i>	ACATGGTGCCAGCCATTCA	AAGCCGTTCTAGCCATGAT
<i>Lcch3</i>	<i>GABRB1-3</i>	CCGAGACGTGTTCAACGACA	GGCTATGTCGGTGCCATAA
<i>Grd</i>	<i>GABRA1-6</i>	TTGGCTACACAACGTCGGA	GGTCGTGGTGGATCCTGTT
<i>CG8916</i>	<i>GABRA6</i>	TTGAGTCCAAGAGCGGTGTC	CGTTGGGTGGTCTCTCCA
<i>Rdl</i>	<i>GABRP</i>	TGGCTCAATCGCAATGCAAC	GACCGTGGCGTATTCCAGTA
<i>CG12344</i>	<i>GLRA2</i>	CGAGAGCTCTCGTCGAACA	GAAGTATACTGGTGAGGCGGG
<i>GABA-B-R1</i>	<i>GABBR1</i>	CTCAGGGCGATCGTATTGCT	GGTGCCTAGAACATGGGTGA
<i>GABA-B-R2</i>	<i>GABBR2</i>	TGGCGGGTGCATTGATATT	TCTCGTGTGCAAGGGTTCC
<i>GABA-B-R3</i>	<i>GABBR2</i>	AATTCGCACAGCAATCTGCC	ACAGCTCAAAGAGTCGAGC

(Continued on next page)

**Continued**

Fly	Human	Forward primer sequence (5' to 3')	Reverse primer sequence (5' to 3')
Sh	KCNA1-7,10	TGTCAGGTTCCCGCATGTC	CTGACTGGCGCTTTGGAAG
Shab	KCNB1,2	CGTGCTCGCGTTAGTGTG	TTCTGGTACTCGGCGCATTT
SK	KCNN1-3	GGTTATCGAAAACGAACTGAGCA	CTTCCAAGCATGGTAAGCTAC
para	KCNB1,2	ACGAGGATGAAGGTCCACAAC	ACGACGTATCGGATTGAATGG
Nmdar2	GRIN2A-D	GGCATCCCGGTTATCTCGT	AGAACTGGTGCCACTTGTAGC

**Climbing assay**

Approximately 25 male flies were placed in an empty plastic vial. The vial was then gently tapped to knock all of the flies to the bottom. The numbers of flies in the top, middle, or bottom thirds of the vial were pictured and scored after 10 s. The percentages of flies that stayed at the bottom were subjected to statistical analyses.

**Histological analysis**

Heads of male flies were fixed in 4% paraformaldehyde for 24 h at 4°C and embedded in paraffin. Serial sections (6 µm thickness) through the entire heads were prepared, stained with hematoxylin and eosin (Sigma-Aldrich), and examined by bright-field microscopy. Images of the sections were captured with AxioCam 105 color (Carl Zeiss). To score brain vacuolization, we performed microscopy of serial brain sections within the central neuropil regions and selected the images with the most severe vacuolization from each fly to score area of vacuolization. We selected a section with the most severe neurodegeneration in the same brain area from each individual fly and the area of vacuoles was measured using ImageJ (NIH). We repeated the experiments more than two times and two to three persons are independently involved in these tasks to avoid any bias.

**Drug feeding in flies**

Flies were fed with the food containing 10 µM or 50 µM NCH51 or vehicle (final concentration 0.02% dimethyl sulfoxide) from the day after eclosion. These food vials were changed every 3-4 days.

**Western blotting analysis of fly models**

Western blotting was performed as described previously (Ando et al., 2016). To detect human Aβ42, ten fly heads for each genotype were homogenized in Tris-Glycine SDS sample buffer, and the same amount of the lysate was loaded to 18% Tris-Glycine gels and transferred to nitrocellulose membrane. The membranes were boiled in PBS for 3 min, blocked with 5% nonfat dry milk, blotted with the anti-Aβ 6E10 antibody (Signet, Covance), incubated with appropriate secondary antibody and developed using ECL Western Blotting Detection Reagents (GE Healthcare Life Sciences). The membranes were also probed with anti-tubulin (Sigma-Aldrich) as the loading control in each experiment. To detect human tau, ten fly heads for each genotype were homogenized in Tris-Glycine SDS sample buffer, and the same amount of the lysate was loaded to each lane of 10% Tris-Glycine gels and transferred to nitrocellulose membrane. The membranes were blocked with 5% nonfat dry milk, blotted with the antibodies described below, incubated with appropriate secondary antibody and developed using ECL Prime Western Blotting Detection Reagent (GE Healthcare Life Sciences). The membranes were also probed with anti-Nervana and used as the loading control in each experiment. Anti-tau (Merck Millipore), anti-pSer202/pThr205 tau (Thermo Fisher Scientific), anti-Nervana (Developmental Studies Hybridoma Bank) antibodies were purchased. Imaging was performed with ImageQuant LAS 4000 (GE Healthcare Life Sciences), and the signal intensity was quantified using ImageJ (NIH).

**QUANTIFICATION AND STATISTICAL ANALYSIS**

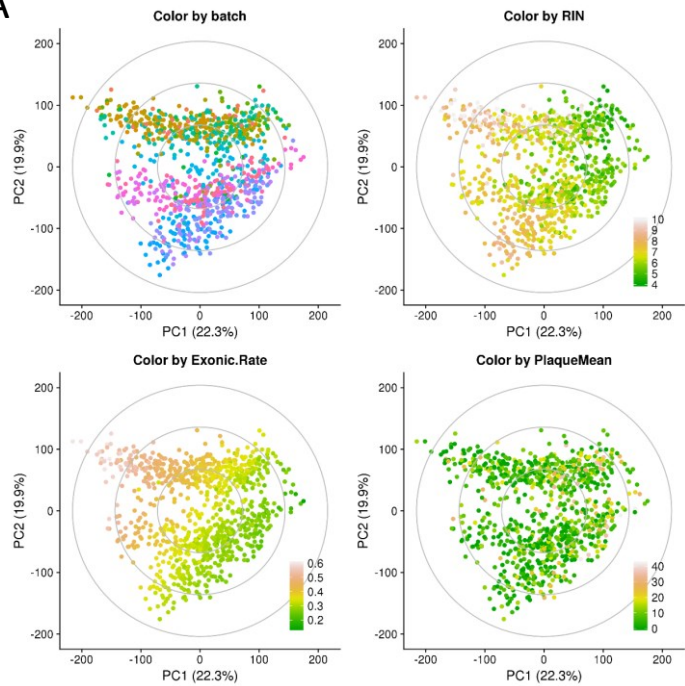
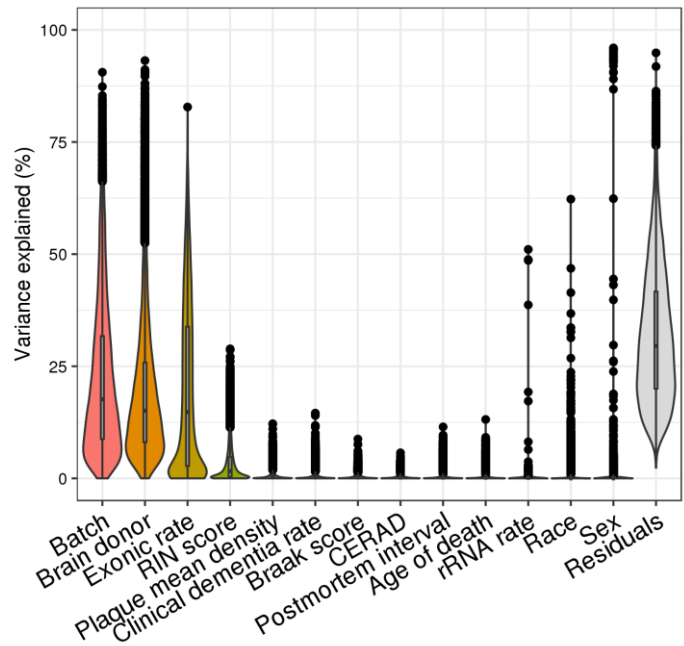
The analytical approaches and software used for quantification were specified for each assay. All available brain tissues from MSBB were sent for sequencing analysis, without randomization process. For sample processing, clustering, differential expression and network analyses, all investigators were blinded to outcomes. The statistical test used and sample size *n* are indicated in the figure legends and the corresponding methods section. Statistical significance is defined as *p* < 0.05 (\* = *p* < 0.05 ; \*\* = *p* < 0.01, \*\*\* = *p* < 0.001, \*\*\*\* = *p* < 0.0001).

**Supplemental Information**

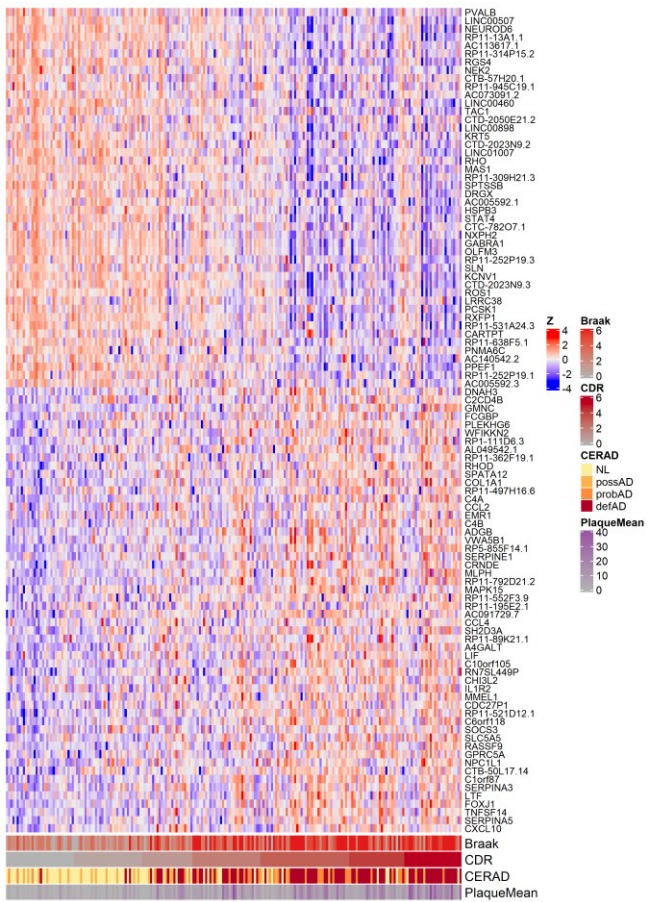
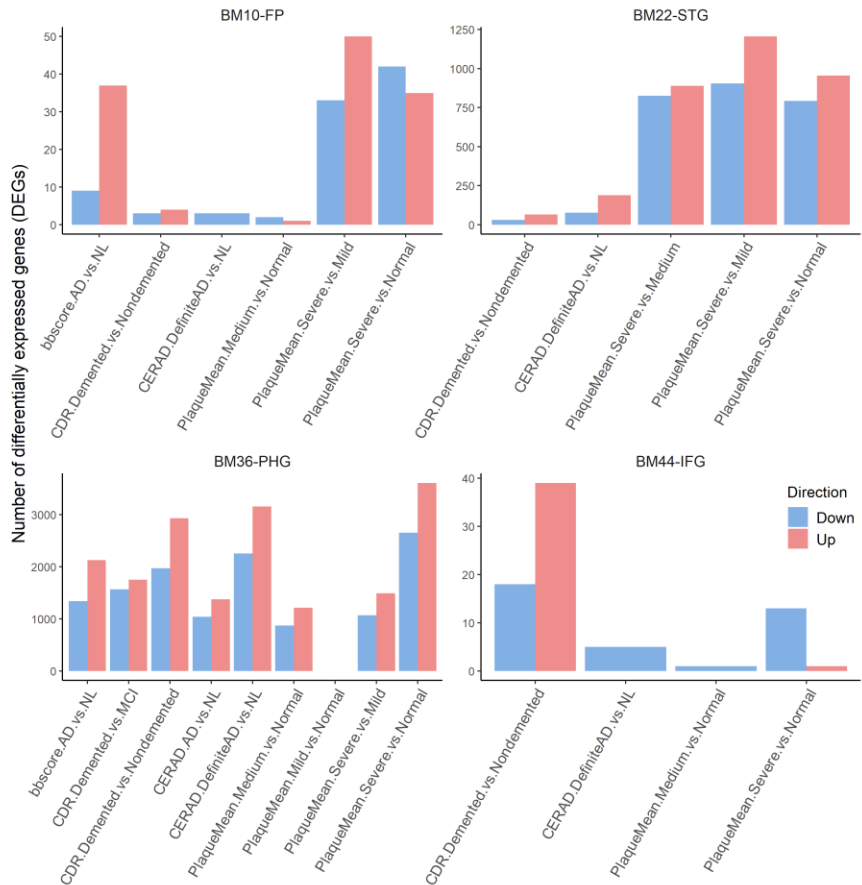
**Transformative Network Modeling of Multi-omics**

**Data Reveals Detailed Circuits, Key Regulators,  
and Potential Therapeutics for Alzheimer's Disease**

Minghui Wang, Aiqun Li, Michiko Sekiya, Noam D. Beckmann, Xiuming Quan, Nadine Schrode, Michael B. Fernando, Alex Yu, Li Zhu, Jiqing Cao, Liwei Lyu, Emrin Horgusluoglu, Qian Wang, Lei Guo, Yuan-shuo Wang, Ryan Neff, Won-min Song, Ermeng Wang, Qi Shen, Xianxiao Zhou, Chen Ming, Seok-Man Ho, Sezen Vatansever, H. Ümit Kaniskan, Jian Jin, Ming-Ming Zhou, Kanae Ando, Lap Ho, Paul A. Slesinger, Zhenyu Yue, Jun Zhu, Pavel Katsel, Sam Gandy, Michelle E. Ehrlich, Valentina Fossati, Scott Noggle, Dongming Cai, Vahram Haroutunian, Koichi M. Iijima, Eric Schadt, Kristen J. Brennand, and Bin Zhang

**A****B**

**Fig. S1. RNA-seq data correction for confounding factors, related to STAR Methods.** **A.** Principal component (PC) plots showing the association between biological/technical variables and top PCs. **B.** Distribution of variance explained by the biological/technical variables according to variancePartition analysis. From left to right, variables were sorted in descending order by median fraction of variance explained.

**A****B**

**Fig. S2. Summary of differential expression signatures, related to STAR Methods.** **A**, Heat-map showing the expression variation of top 100 differentially expressed genes (DEGs) ranked by fold change in the BM36-PHG region. The expression of each gene were scaled into z-values. Sample-level trait values were annotated in the bottom. **B**, bar-plot showing the number of DEGs identified in each contrast for each region regarding 4 different cognitive/neuropathological traits. X-axis denotes the trait-specific contrast. Down, down-regulated DEGs; Up, up-regulated DEGs.

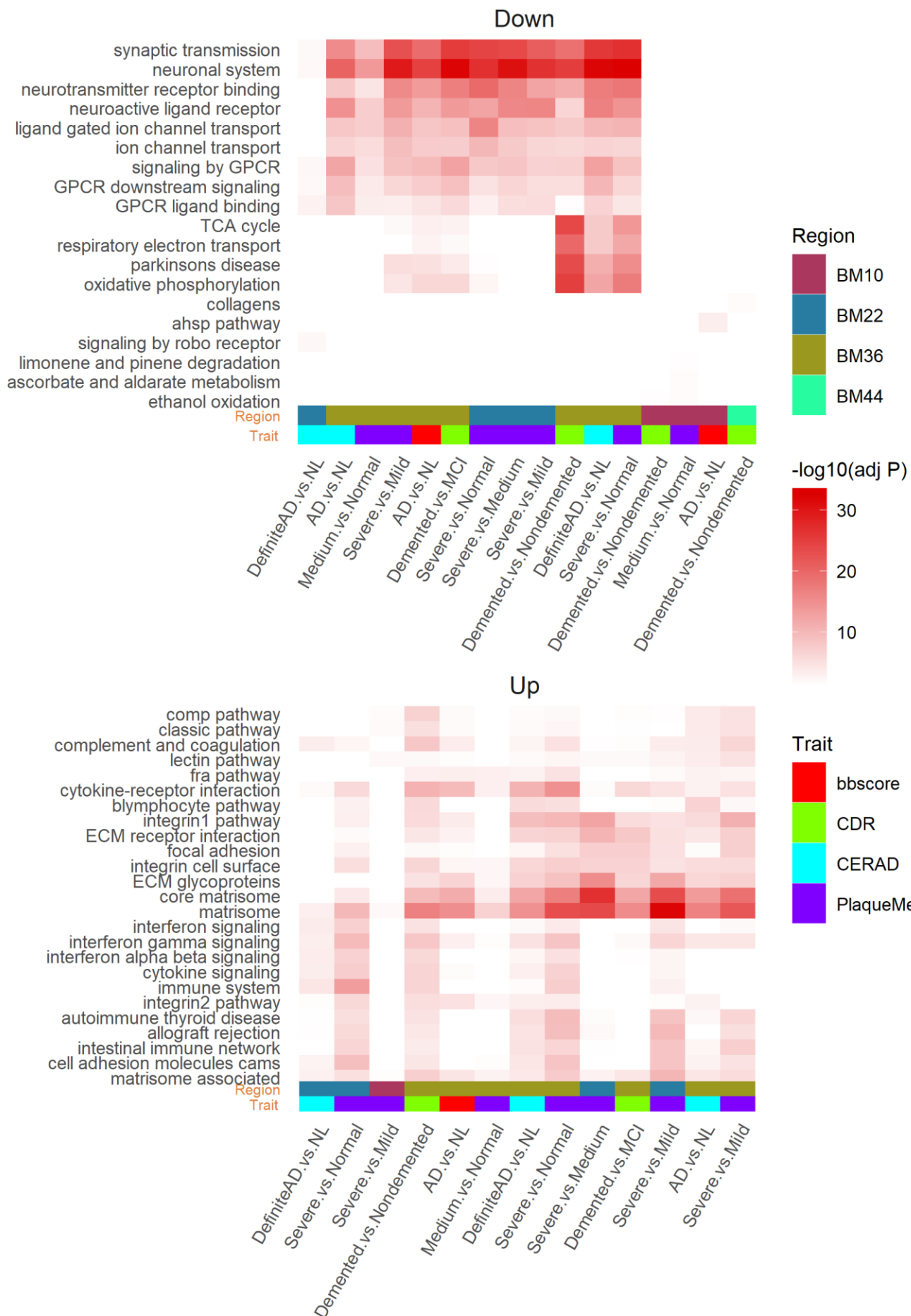


**Fig. S3. Summary of gene ontology (GO)/pathways enriched in differential expression signatures, related to STAR Methods.** Top pathways enriched in the present down-regulated (top) or up-regulated (bottom) DEGs. Columns denote different set of DEGs from 4 brain regions regarding 4 different cognitive/neuropathological traits and rows denote GO/pathways. Down, down-regulated DEGs; Up, up-regulated DEGs.

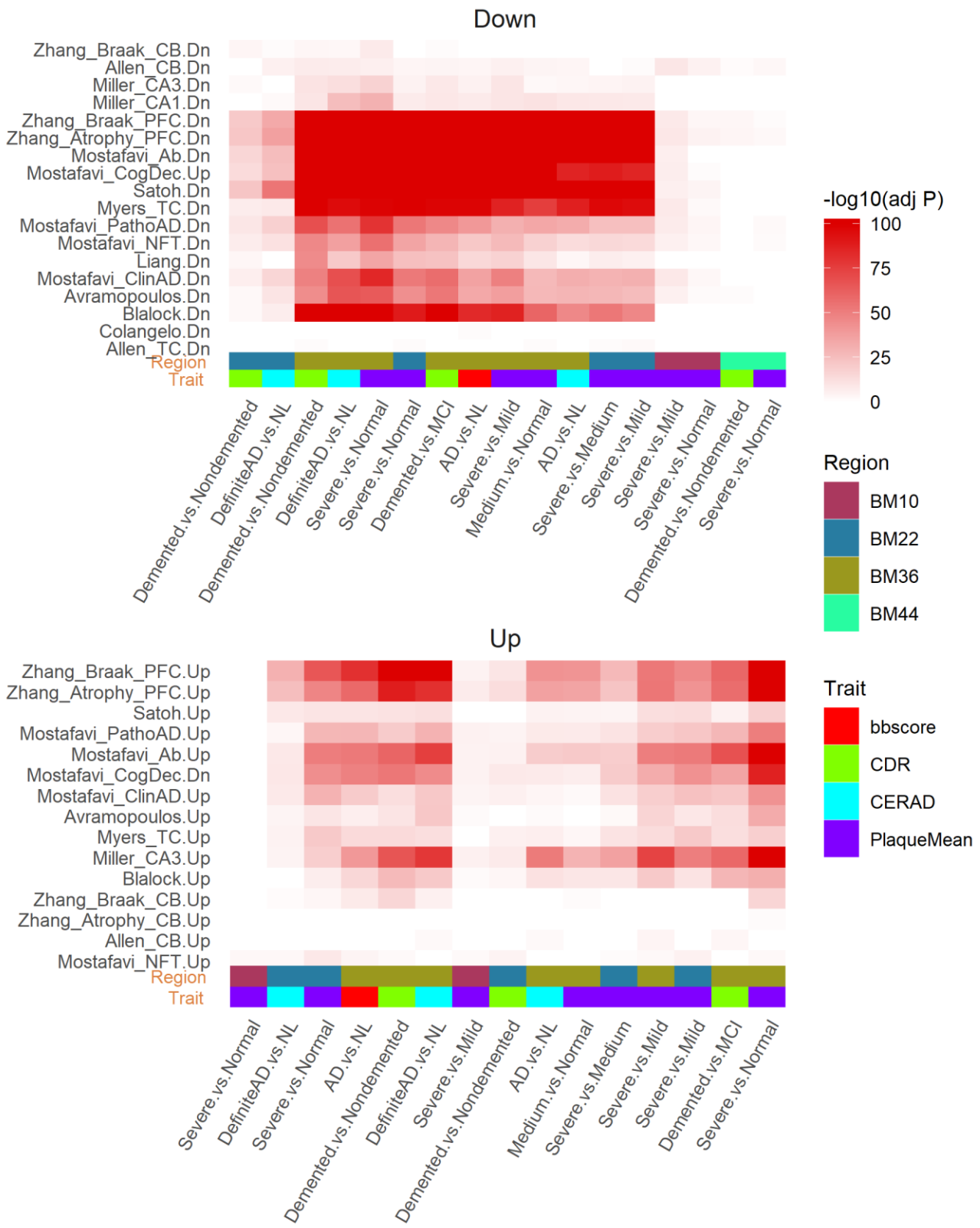


**Fig. S4. Preservation of differential expression signatures in published bulk-tissue transcriptomic analysis datasets, related to STAR Methods.** Public AD signatures enriched in the present down-regulated (top) or up-regulated (bottom) DEGs. In each panel, columns denote the present region-specific DEGs stratified by region, trait and contrast. The rows denote public AD signatures written in a format of “signature.direction”, where “direction” is either Dn (down-regulated) or Up (up-regulated), and “signature” includes: 1) Allen\_CB, signature detected in the cerebellum region from Allen et al 2018, 2) Allen\_TC, signature detected in the temporal cortex region from Allen et al 2018, 3) Avramopoulos, signature detected in the temporal lobe from Avramopoulos et al 2011, 4) Blalock, signature detected in the hippocampus from Blalock et al 2004, 5) Colangelo, signature detected in the hippocampus CA1 region from Colangelo et al 2002, 6) Liang, signature detected in multiple cortex areas from Liang et al 2008, 7) Miller\_CA1, signature detected in the hippocampus CA1 region from Miller et al 2013, 8) Miller\_CA3, signature detected in the hippocampus CA3 region from Miller et al 2013, 9) Mostafavi\_Ab, signature correlated with B amyloid in the prefrontal cortex (PFC) region from Mostafavi et al 2018, 10) Mostafavi\_ClinAD, signature correlated with clinical diagnostic of AD in the PFC from Mostafavi et al 2018, 11) Mostafavi\_CogDec, signature correlated with cognitive decline in the PFC from Mostafavi et al 2018, 12) Mostafavi\_PathoAD, signature correlated with AD pathology in the PFC from Mostafavi et al 2018, 13) Satoh; signature detected in the frontal cortex region from Satoh et al 2014, 14) Myers\_TC, signature computed by comparing gene expression between AD and control with limma from the temporal cortex region from Webster et al 2009, 15) Zhang\_Atrophy\_CB, signature correlated with atrophy in the cerebellum region from Zhang et al 2013, 16) Zhang\_Atrophy\_PFC, signature correlated with atrophy in the PFC from Zhang et al 2013, 17) Zhang\_Braak\_CB, signature correlated with Braak staging in the cerebellum region from Zhang et al 2013, 18) Zhang\_Braak\_PFC, signature correlated with Braak staging in the PFC from Zhang et al 2013. The references of the public AD signatures are listed in supplementary text.

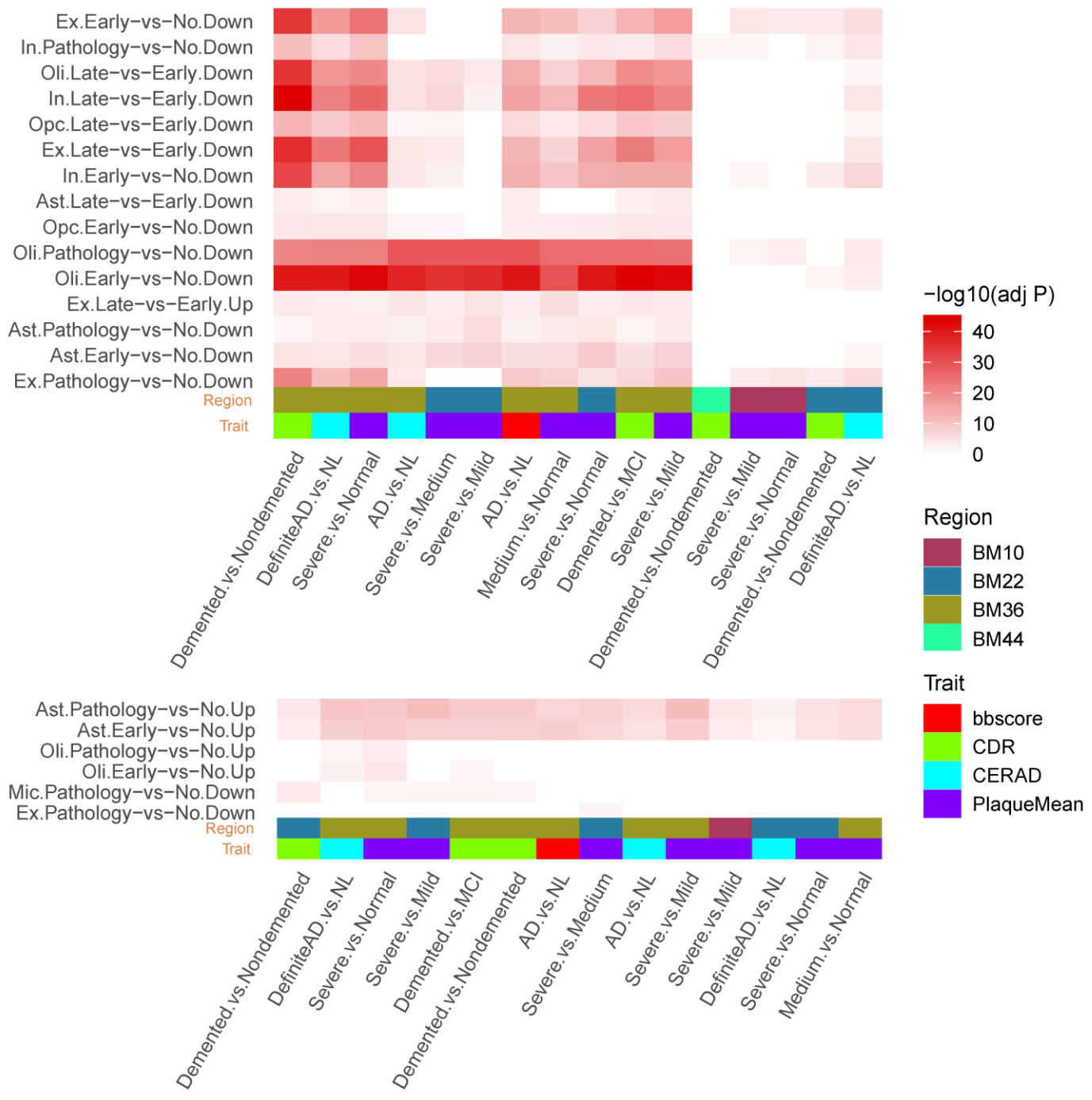


**Fig. S5. Preservation of differential expression signatures in a public single-nucleus RNA-seq (snRNA-seq) analysis of AD and control brains, related to STAR Methods.** The present down-regulated (top) or up-regulated (bottom) DEGs were enriched in cell type-specific AD signatures detected by snRNA-seq (Mathys et al 2019). Columns denote the present DEG signatures identified from 4 brain regions regarding 4 different cognitive/neuropathological traits and rows denote cell type-specific DEGs. The snRNA-seq cell type-specific DEGs are denoted in a format of “cell.contrast.direction”, where cell is either Ex (excitatory neurons), In (inhibitory neurons), Oli (oligodendrocytes), Opc (oligodendrocyte progenitor cells), Ast (astrocytes), or Mic (microglia), contrast is either Early-vs-No (early pathology versus no pathology), Late-vs-Early (late pathology versus early pathology), or Pathology-vs-No (early and late pathology combined versus no pathology), and direction is either Down (down-regulation) or Up (up-regulation).

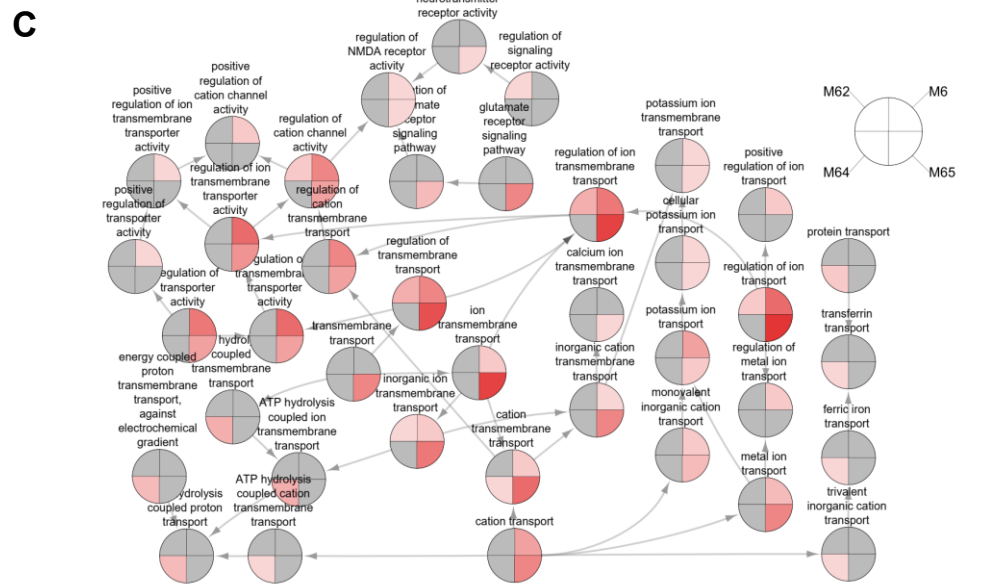
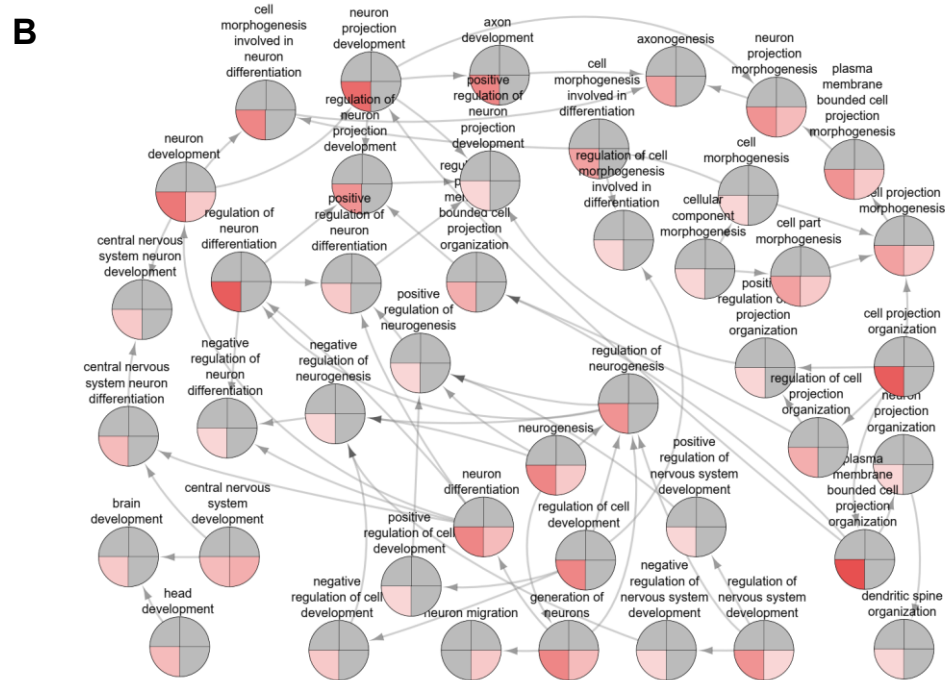
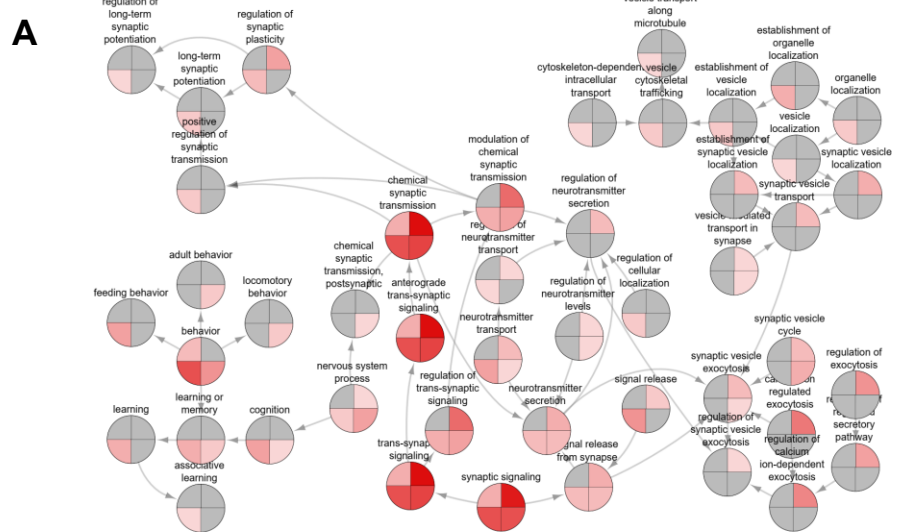


**Fig. S6. GO biological process (BP) hierarchy enrichment reveals distinct functional roles that the top-ranked neuronal/synaptic modules may play, related to Figure 2.** Each node denotes a GO/BP term, with a pie-chart displaying the  $-\log_{10}$ (adjusted P value) of the FET enrichment for the 4 top-ranked neuronal/synaptic modules (i.e. M6, M62, M64 and M65). Arrows denote the direction from a parent term to a child term. The GO hierarchy was extracted from the R/Bioconductor package GO.db and the GO/BP annotation gene sets were obtained from the R/Bioconductor package org.Hs.eg.db. The three subplots A-C group terms in relation to synaptic function, neuronal development and transportation, respectively.

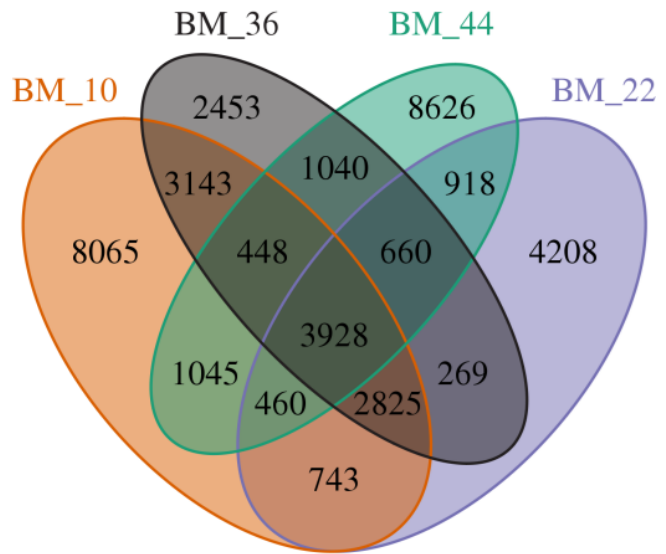
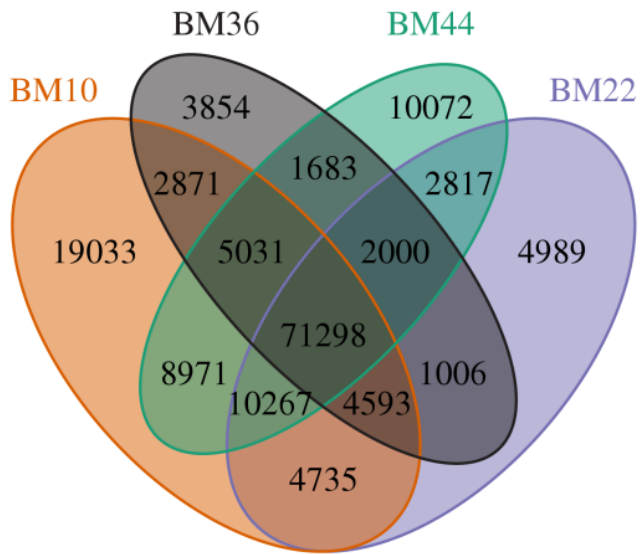
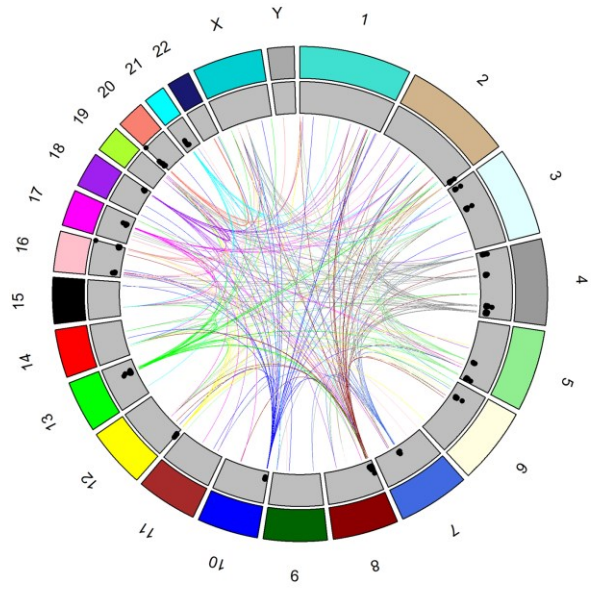
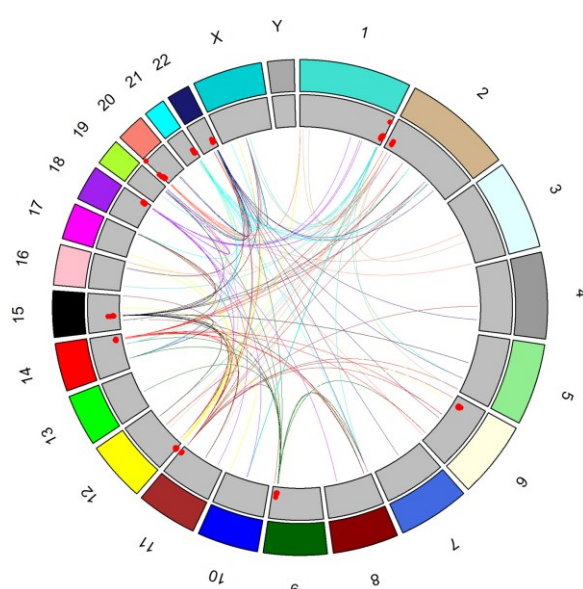


**Fig. S7. eQTLs are shared among different regions, related to STAR Methods.** Venn-diagram showing the overlap among *cis*-eQTLs (left) and *trans*-eQTLs (right).

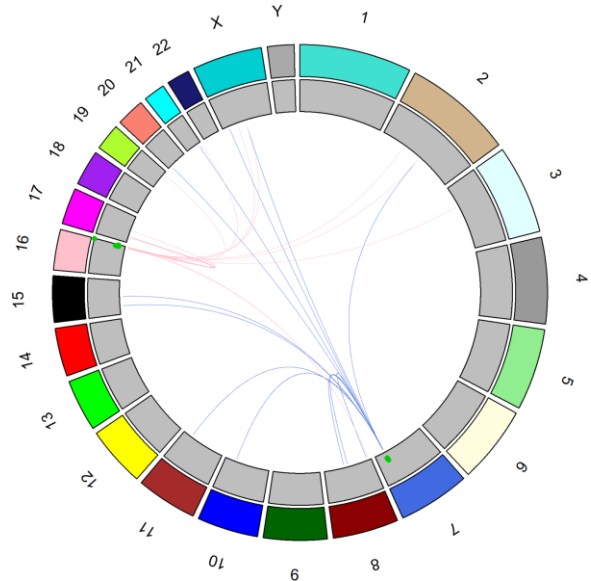
BM10-FP



BM22-STG



BM36-PHG



BM44-IFG

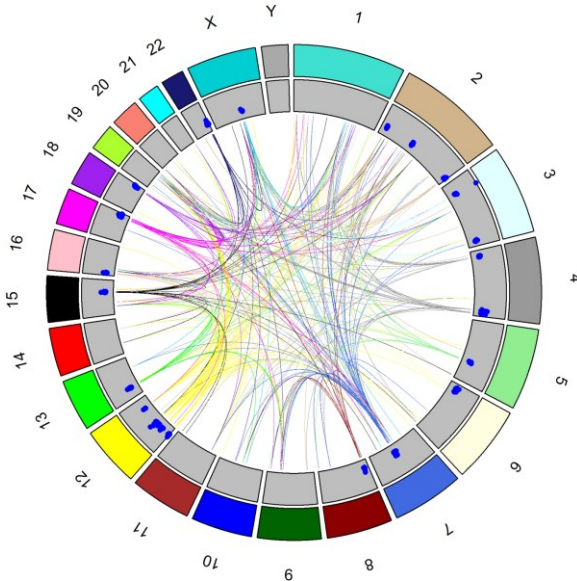


**Fig. S8. Trans-eQTL hotspots identified in the 4 brain regions, related to STAR Methods.** The outermost first track shows the chromosome id. The second track denotes the color coding of the chromosomes. The dots in the third track denote the  $-\log_{10}(P)$  value of the trans-eQTL associations for the hotspots. Links in the middle connect the hotspots to the associated trans-eGenes. Links are colored by the chromosomal origination of the trans-eQTL hotspots.

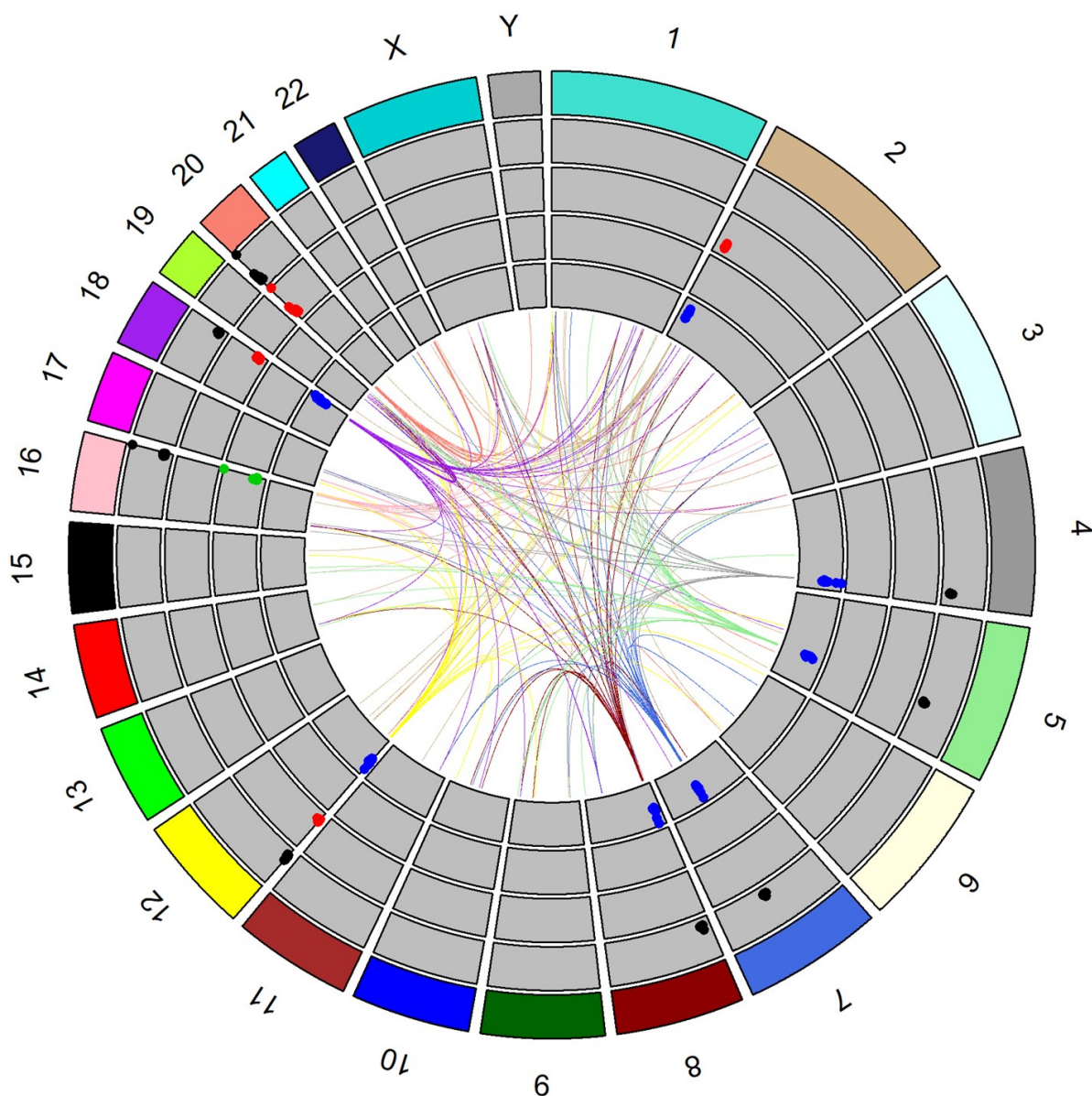
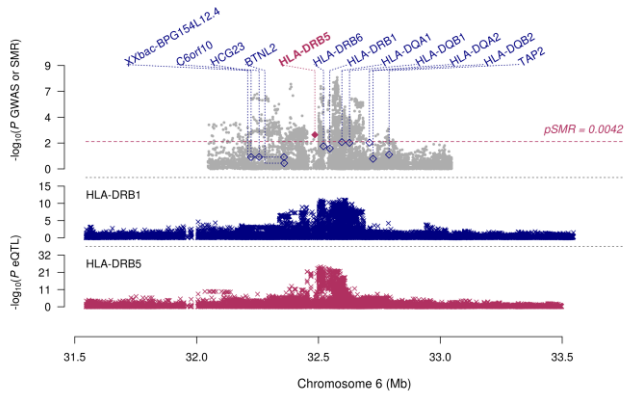
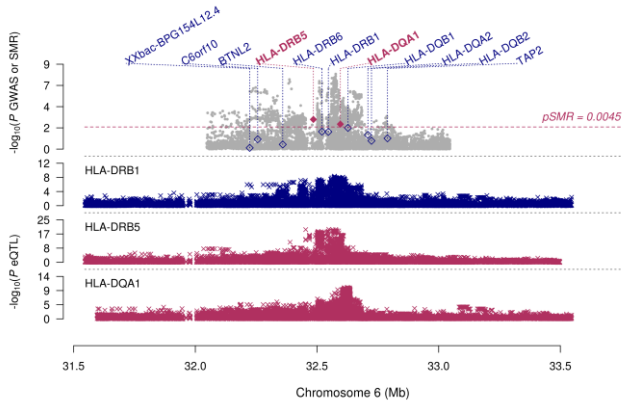


**Fig. S9. Trans-eQTL hotspots shared by at least two brain regions, related to STAR Methods.** The outermost first track shows the chromosome id. The second track denotes the color coding of the chromosomes. The dots in the third to sixth tracks denote the  $-\log_{10}(P \text{ value})$  of the *trans*-eQTL associations for the hotspots in brain region BM10-FP, BM22-STG, BM36-PHG and BM44-IFG, respectively. Links in the middle connect the hotspots to the associated *trans*-eGenes. Links are colored by the chromosomal origination of the *trans*-eQTL hotspots.

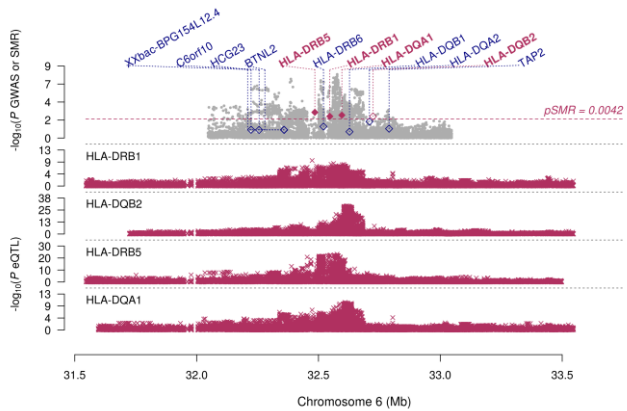
A



B



C



D

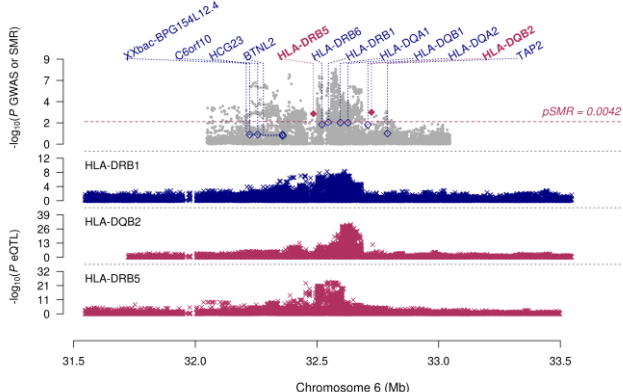
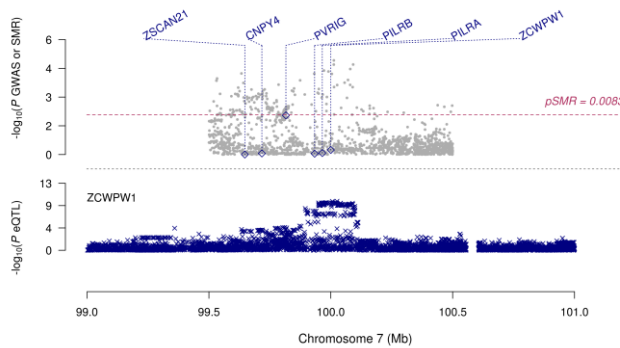
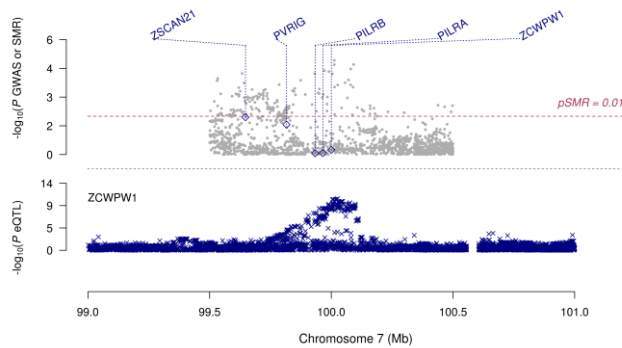


**Fig. S10. Summary data-based Mendelian randomization (SMR) analysis at the *HLA-DRB1/HLA-DRB5* locus based on Kunkle et al 2019 AD GWAS summary statistics, related to STAR Methods.** A-D show the SMR analysis results integrating IGAP AD GWAS with eQTLs derived from brain regions BM10, BM22, BM36 and BM44, accordingly. For the top panel in each plot, dots represent the P values for SNPs from the IGAP AD GWAS analysis and diamonds represent the P values for genes from the SMR test. Filled diamonds highlight the genes surpassing the HEIDI test ( $P \geq 0.05$ ). The genes with cis-eQTLs are listed on the top. Genes surpassing the SMR test were highlighted in red. Dashed line shows the region-specific Bonferroni corrected P value significance threshold of the SMR test controlling for the number of genes examined. Bottom plot shows the eQTL P values of SNPs from the present data.

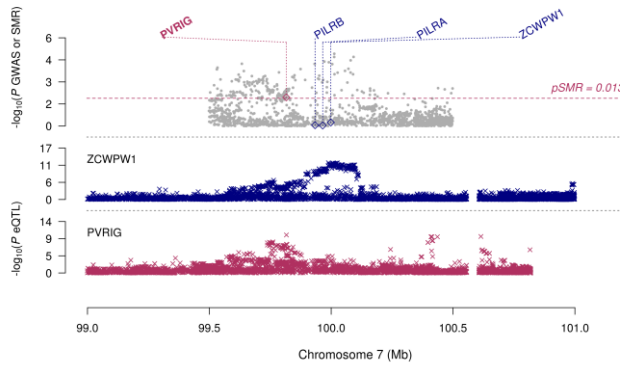
A



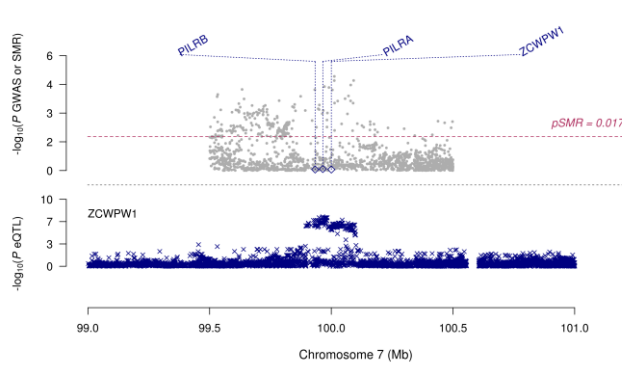
B



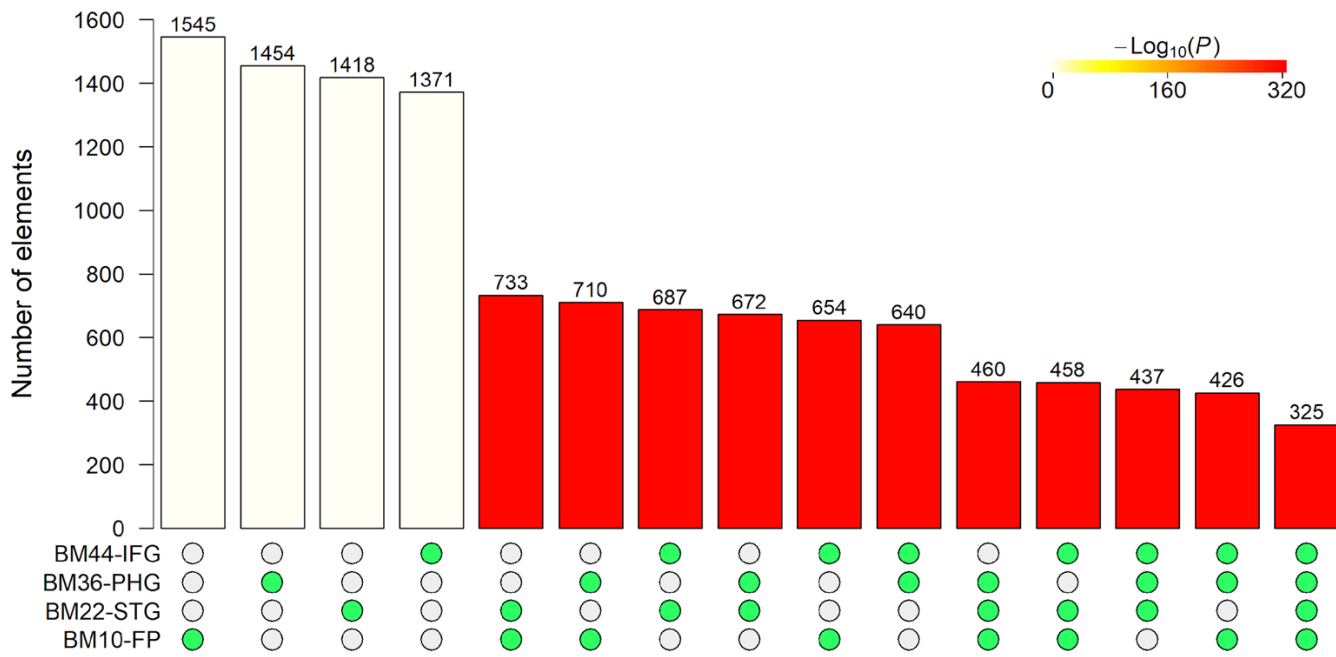
C



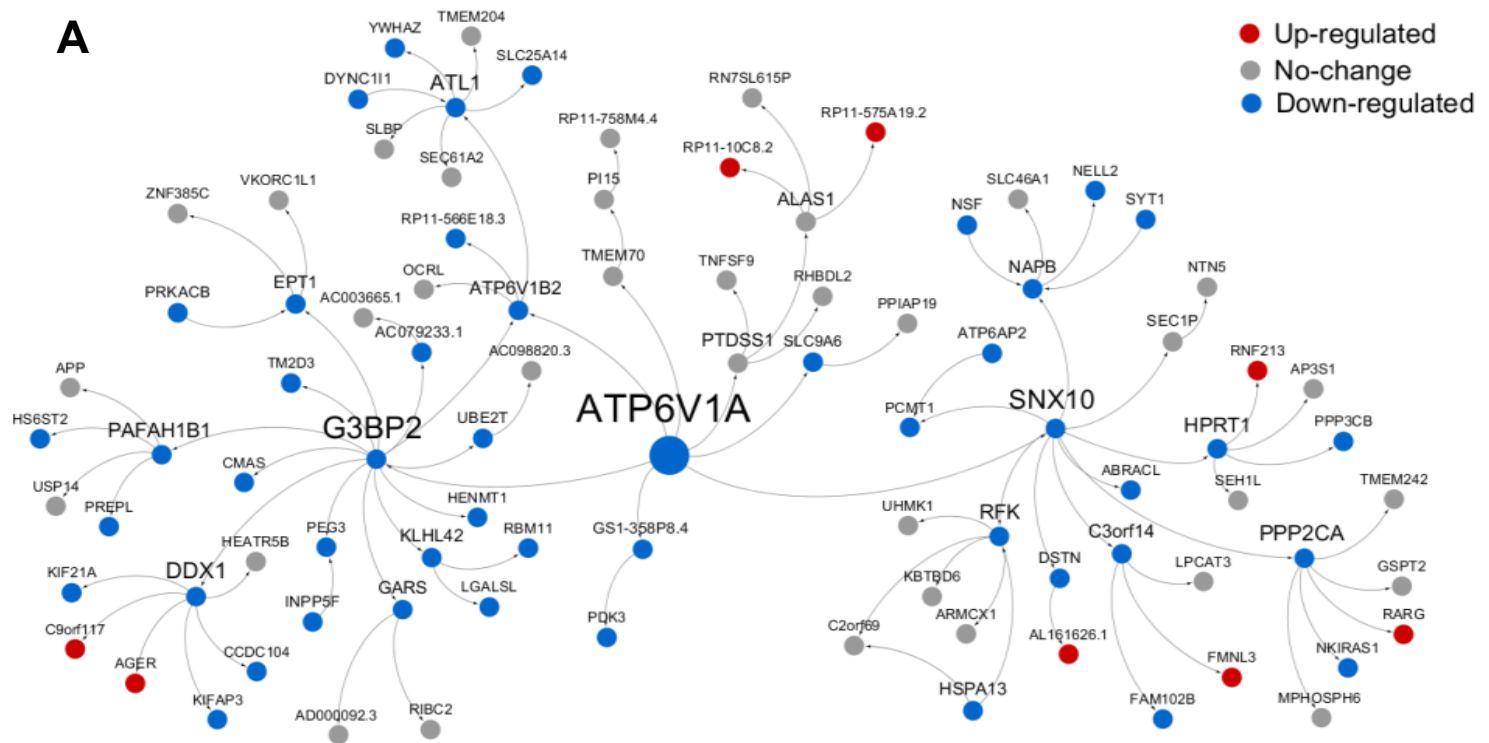
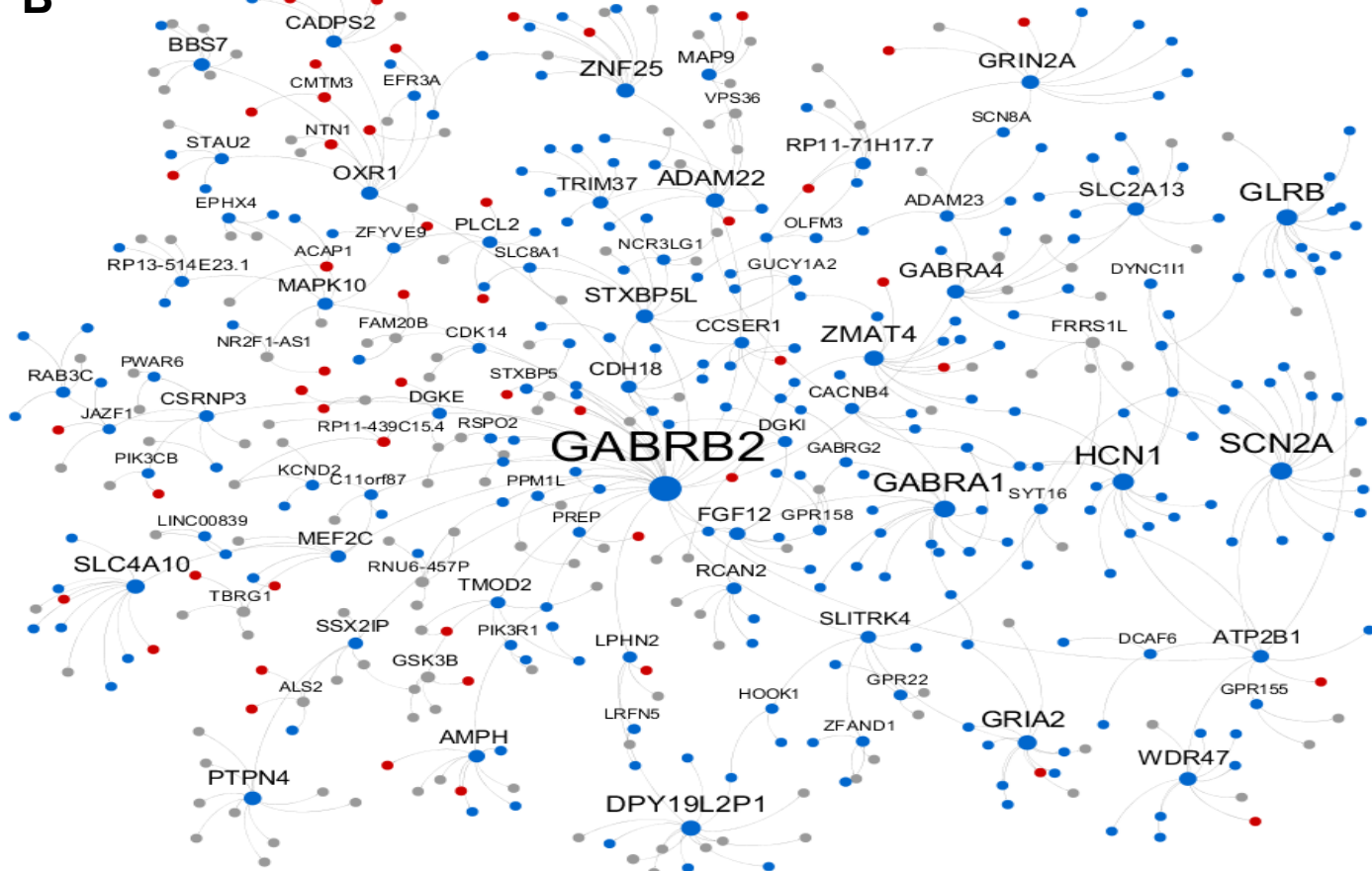
D



**Fig. S11. SMR analysis at the *ZCWPW1* locus based on Kunkle et al 2019 AD GWAS summary statistics, related to STAR Methods.** A-D show the results from BM10, BM22, BM36 and BM44, accordingly. Figure legend is the same as in Fig S11.



**Fig. S12. Bayesian network key drivers are strongly shared among brain region-specific networks, related to STAR Methods.** The bar height denotes the number of key drivers overlapping in a given comparison as specified by the green circles underneath. The overlap size is also shown above the bar. The color denotes the P value significance of the overlap size.

**A****B**

**Fig. S13. Network neighborhood of key driver genes *ATP6V1A* and *GABRB2* on the BM36-PHG BN, related to Figure 3 and STAR Methods.** Down-regulated genes in demented brains are enriched in network neighboring (A) *ATP6V1A* ( $FE = 5.4$  and  $FDR = 3.7E-19$ ) and (B) *GABRB2* ( $FE = 5.8$ ,  $FDR = 1.1E-106$ ). Node color denotes the direction of gene expression change in the BM36-PHG region of patients with dementia ( $CDR \geq 1$ ).

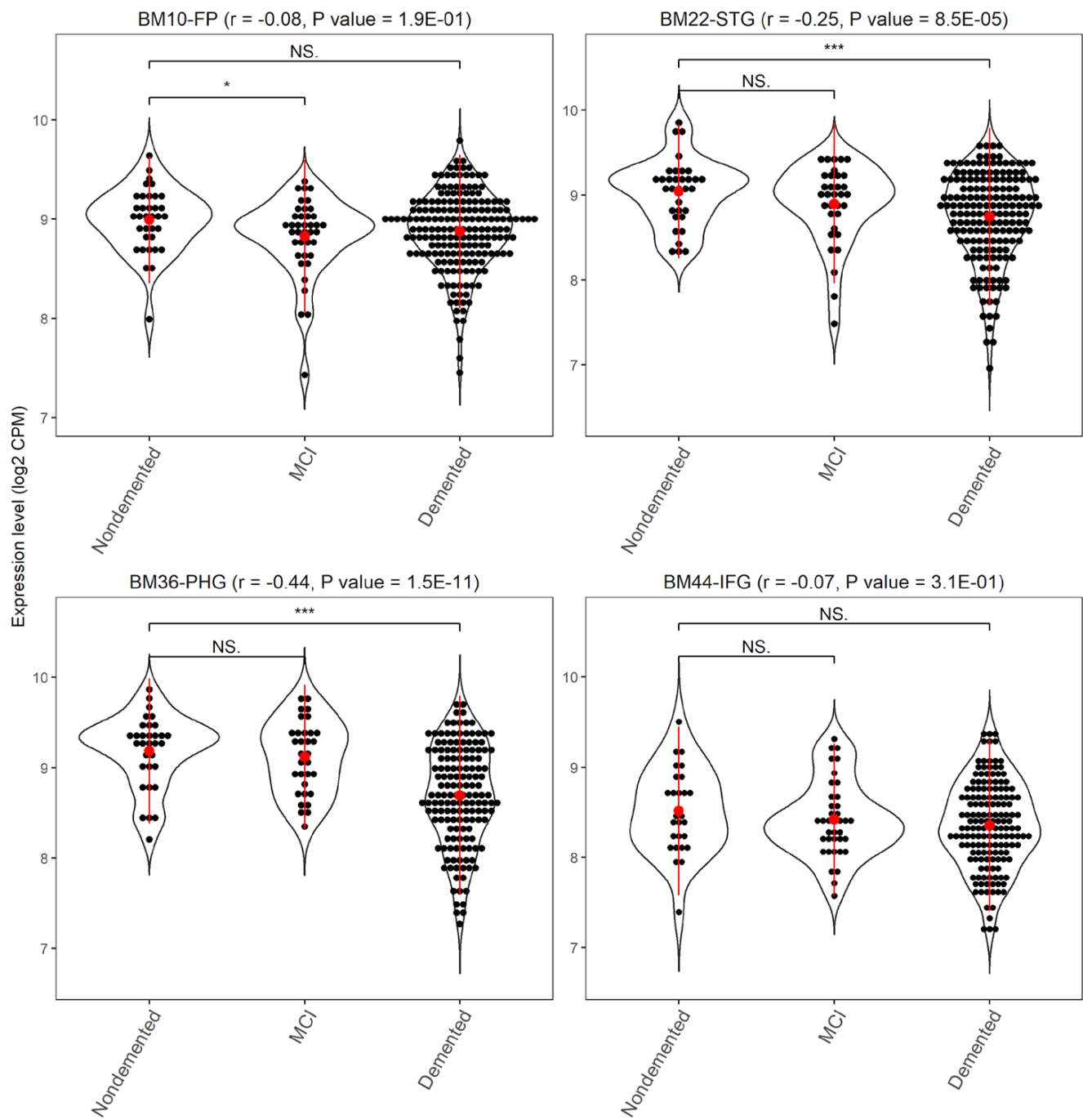


**Fig. S14. *ATP6VIA* is down-regulated in demented patients in multiple brain regions, related to Figure 3.** Significance bar represents t-test  $P$  value. \* $p < 0.05$ ; \*\*\* $p < 0.001$ , NS., no significance. Correlation coefficient ( $r$ ) and  $P$  value of the Spearman correlation between *ATP6VIA* expression and clinical trait CDR are also shown in the top of each sub-plot.

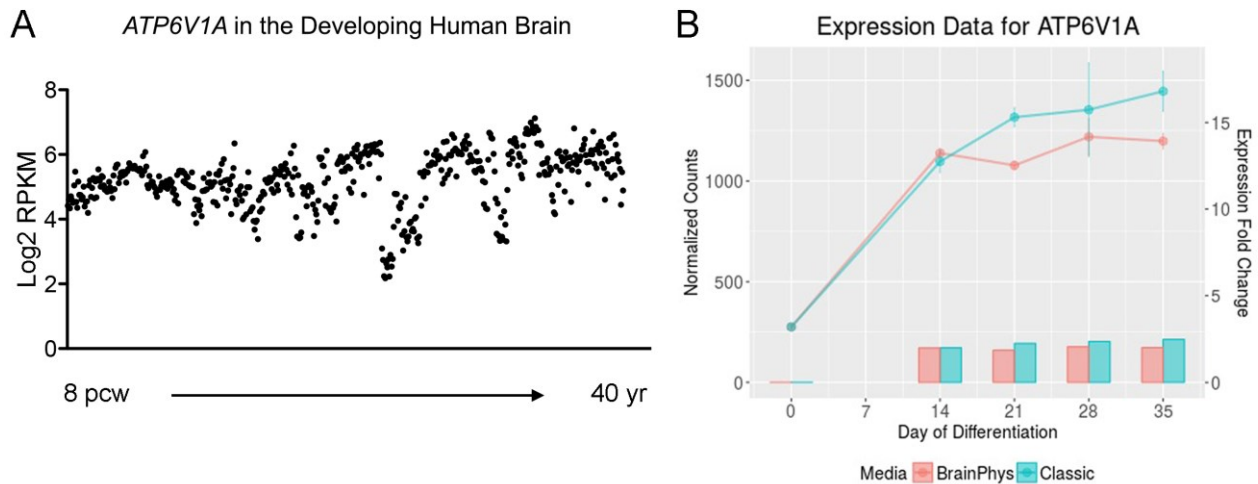


**Fig. S15.** *ATP6V1A* is robustly expressed among different nerve cells, related to Figure 4. (A) A scatter plot represents log<sub>2</sub> RPKM (reads per kilobase per million) expression for *ATP6V1A* gene in the developing brain from age 8 pcw to 40 yrs (Miller et al 2014, available from <https://www.brainspan.org/rnaseq/search/index.html>). (B) *ATP6V1A* visualization in human iPSC-derived neurons during *NGN2*-induction (Tian et al. 2019, available from [https://ineuronrnaseq.shinyapps.io/rnaseq\\_app/](https://ineuronrnaseq.shinyapps.io/rnaseq_app/)).

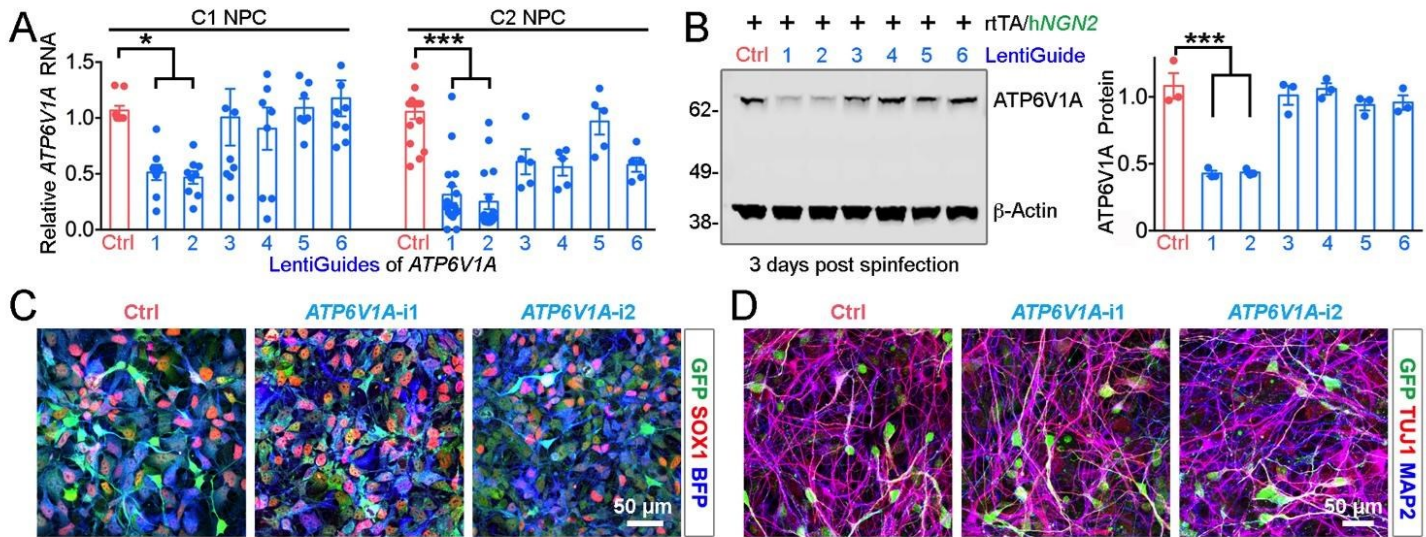


**Fig. S16. Evaluation of six gRNAs for repression of *ATP6V1A* in hiPSC-derived NPCs and *NGN2*-neurons, related to Figure 4.** **A-B**, Normalized relative RNA and protein levels (compared to an empty backbone control) following transduction of dCas9-KRAB NPCs with lentivirus-expressing gRNA targeting *ATP6V1A*. Red: control. Blue: CRISPRi. ANOVA; \*p < 0.05 and \*\*\*p < 0.001; Error bars represent SE. **C-D**, *ATP6V1A* CRISPRi does not affect the neuronal differentiation of NPCs to *NGN2*-neurons. SOX1 is a neural stem cell marker (red); TUJ1 (red) and MAP2 (blue) are pan-neuronal markers. Bars, 50  $\mu$ m.

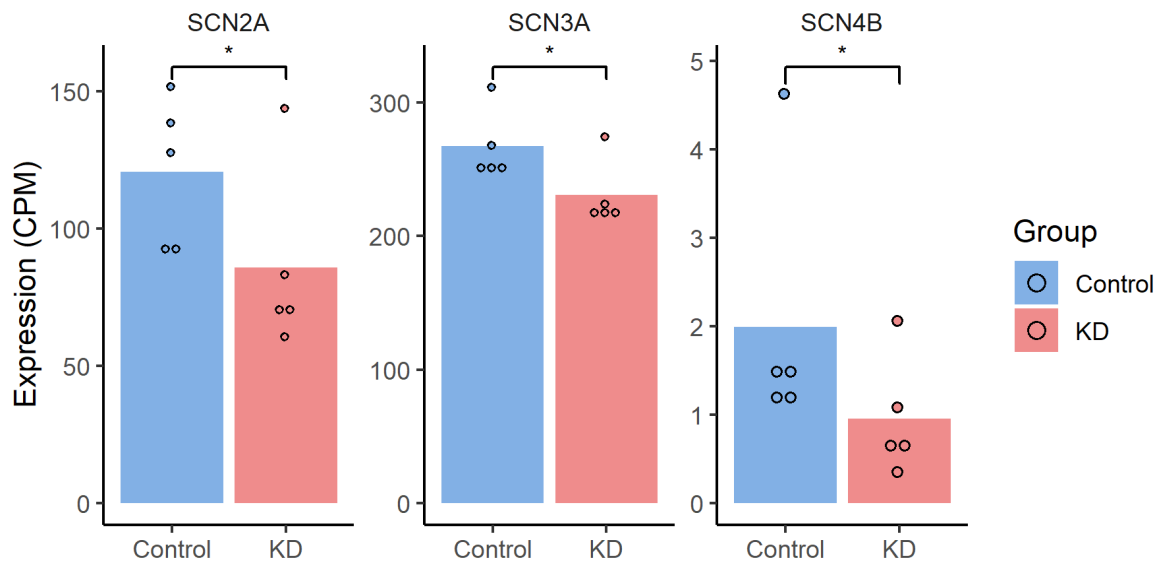


**Fig. S17. RNA-seq revealed reduced mRNA expression of voltage gated sodium channel subunits *SCN3A*, *SCN2A*, and *SCN4B* in *ATP6V1A* KD *NGN2*-neurons, related to Figure 4. \* $p < 0.05$  by Student's t-test.**

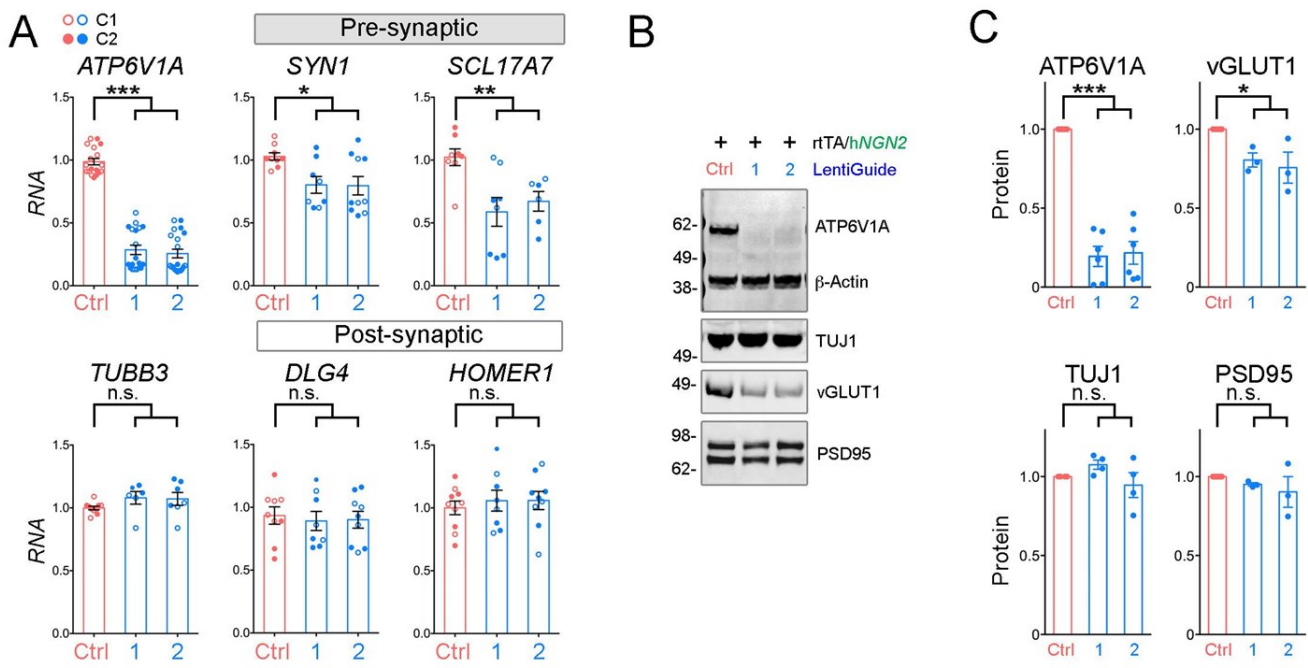


**Fig. S18. Expression of synaptic components in hiPSC-derived *NGN2*-neurons, related to Figure 4.** **A**, qRT-PCR analysis of expression of *ATP6V1A*, *TUBB3*, *SYN1*, *SCL17A7*, *DLG4* and *HOMER1* genes. n = 6-20 replicates. **B-C**, Western blot analysis and quantification of *ATP6V1A*,  $\beta$ -Actin, *TUJ1*, *VGLUT1* and *HOMER1* protein levels. Data represent the mean, n = 3 independent experiments. ANOVA; \*p < 0.05; \*\*p < 0.01; \*\*\*p < 0.001; n.s., no significance; Error bars represent SE.

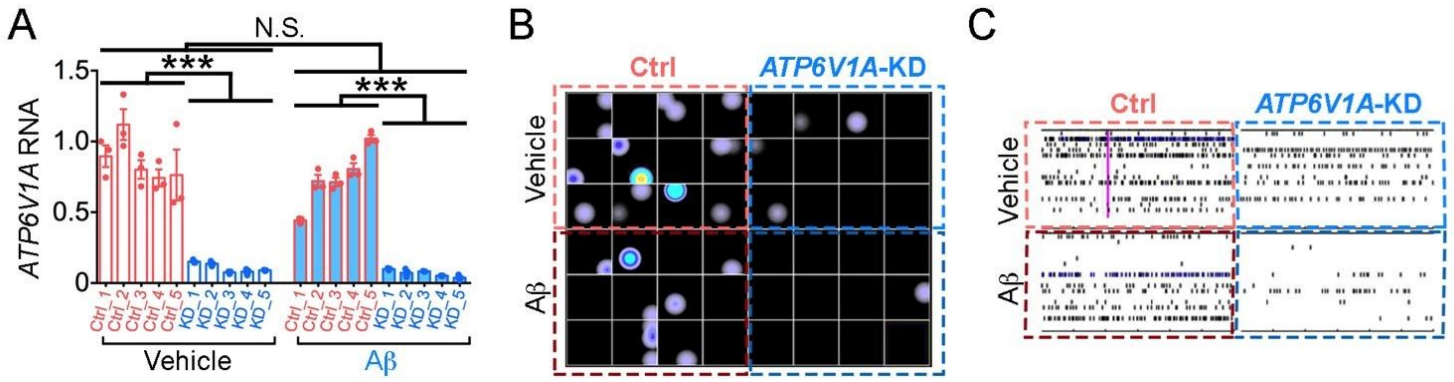


**Fig. S19. MEA arrays in *ATP6V1A*-deficient *NGN2*-neurons with or without exposure to A $\beta$ , related to Figure 4.** **A**, *ATP6V1A* RNA levels across different samples. n = 3 replicates. ANOVA; \*\*\*p < 0.001; N.S., no significance; Error bars represent SE. **B**, Representative heat map recording of a CytoView MEA 48 plate. **C**, Representative raster plots of the spike events over 10 minutes of day 21 (D21) *NGN2*-neurons.

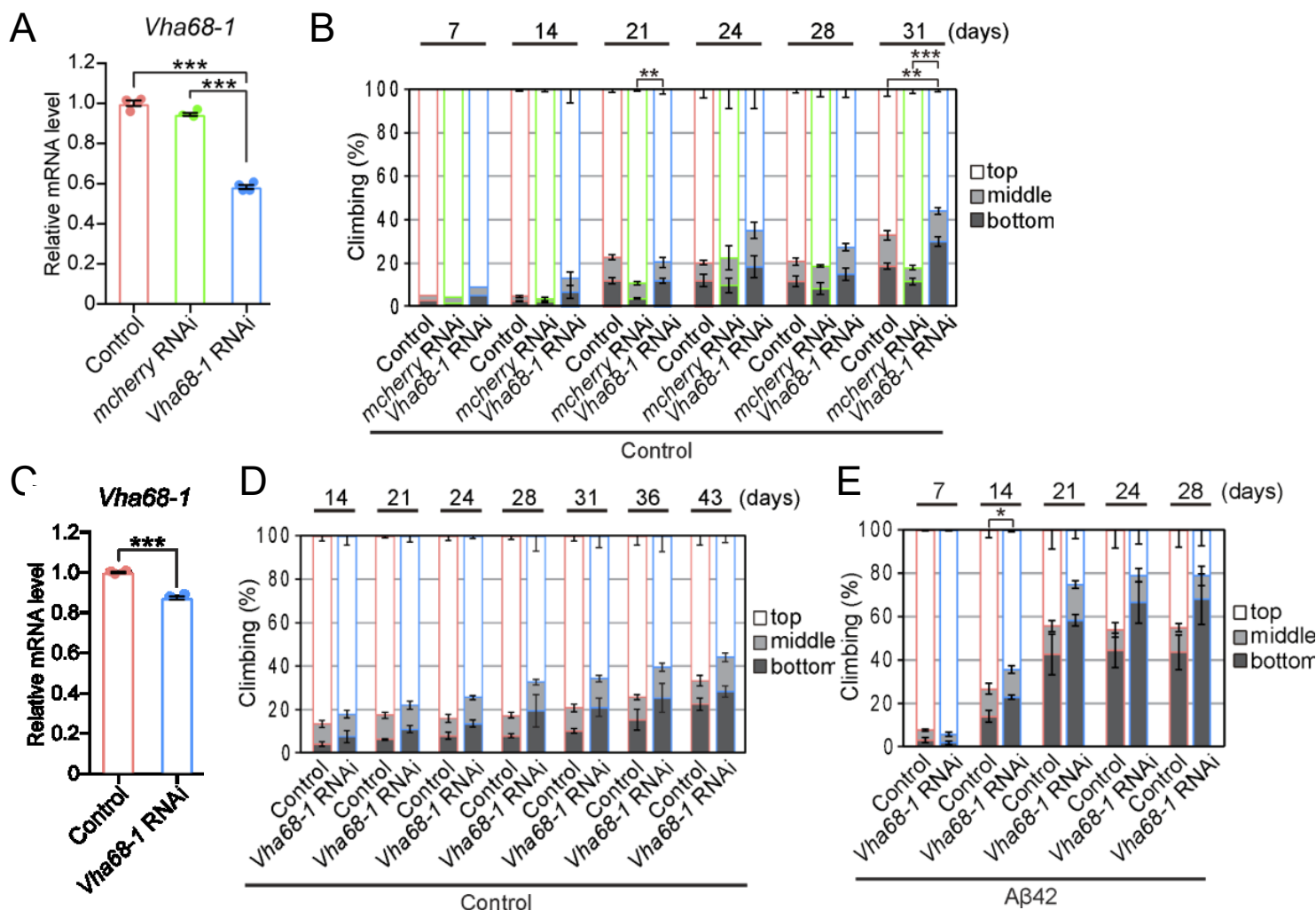
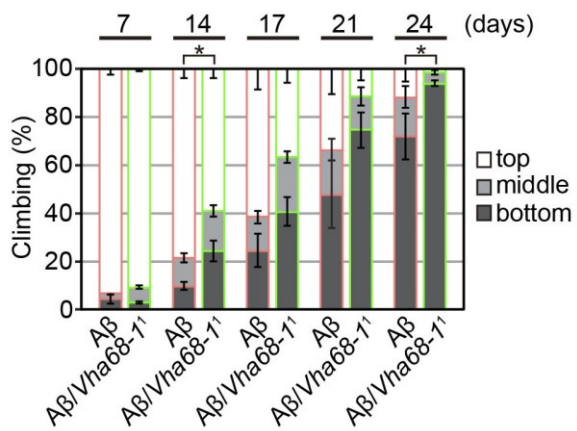
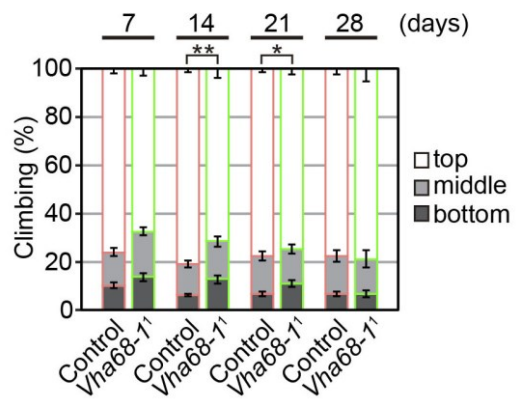


**Fig. S20. Neuronal knockdown of *Vha68-1* exacerbates behavioral deficits caused by overexpression of Aβ42 peptide, related to Figure 4.** **A**, mRNA expression levels of *Vha68-1* in heads of flies expressing RNAi targeting *Vha68-1* (line #50726) were analyzed by qRT-PCR. n = 4, \*\*\*p < 0.001 by Student's t-test. **B**, Neuronal knockdown of *Vha68-1* (line #50726) by itself caused modest decline in climbing ability in aged flies. Average percentages of flies that climbed to the top (white), climbed to the middle (light gray), or stayed at the bottom (dark gray) of the vials. Percentages of flies that stayed at the bottom were subjected to statistical analyses. n = 5 independent experiments except for day 7 when n = 2, \*\*p < 0.01 and \*\*\*p < 0.001 by Student's t-test. **C**, mRNA levels of *Vha68-1* in heads of flies expressing RNAi targeting *Vha68-1* (line #42888) were analyzed by qRT-PCR. n = 4, \*\*\*p < 0.001 by Student's t-test. **D-E**, Neuronal knockdown of *Vha68-1* (line #42888) did not alter climbing ability in control flies (**D**) but slightly enhanced locomotor deficits in Aβ42 flies (**E**). Percentages of flies that stayed at the bottom were subjected to statistical analyses. n = 5 independent experiments, \*\*p < 0.01 and \*\*\*p < 0.001 by Student's t-test. The genotypes of the flies were: **A** and **B**, (Control): *elav-GAL4/Y*; +/*CyO*, (mcherry RNAi): *elav-GAL4/Y*; +/*CyO*; UAS-mcherry RNAi/+, (*Vha68-1* RNAi): *elav-GAL4/Y*; +/*CyO*; UAS-*Vha68-1* RNAi (line #50726)/+. **C** and **E**, (Control): *elav-GAL4/Y*, (*Vha68-1* RNAi): *elav-GAL4/Y*; UAS-*Vha68-1* RNAi (line #42888)/+. **D**, (Aβ42 and Control): *elav-GAL4/Y*; UAS-Aβ42/+; and (Aβ42 and *Vha68-1* RNAi): *elav-GAL4/Y*; UAS-Aβ42/UAS-*Vha68-1* RNAi (line #42888).

A



B



C

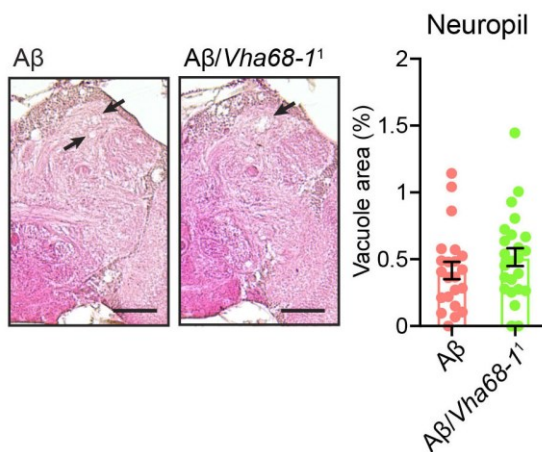


**Fig. S21 A single nucleotide mutation of *Vha68-1* worsens A $\beta$ 42-induced climbing defects, related to Figure 4.** (A) A heterozygous mutation of *Vha68-1* $^1$  worsened locomotor defects caused by A $\beta$ 42 as revealed by climbing assay. (B) A heterozygous mutation of *Vha68-1* $^1$  by itself did not cause obvious climbing defects. Percentages of flies that stayed at the bottom were subjected to statistical analyses. n = 3-4 independent experiments. \*p < 0.05 and \*\*p < 0.01 by Student's t-test. (C) A heterozygous mutation of *Vha68-1* $^1$  slightly worsened neurodegeneration in the neuropil region in A $\beta$ 42 fly brains, but the difference did not reach statistical significance. Representative images show the central neuropil in the paraffin-embedded brain section with hematoxylin and eosin (HE) staining from 24-day-old flies. Scale bars: 50  $\mu$ m. Percentages of vacuole areas (indicated by arrows in the images) were subjected to statistical analyses. n = 22-24 hemispheres. The genotypes of the flies were (A $\beta$ ): *elav*-GAL4/Y;UAS-A $\beta$ 42/+, (A $\beta$ /Vha68-1 $^1$ ): *elav*-GAL4/Y;UAS-A $\beta$ 42/Vha68-1 $^1$ . (Control): *elav*-GAL4/Y and (Vha68-1 $^1$ ): *elav*-GAL4/Y; Vha68-1 $^1$ /+.

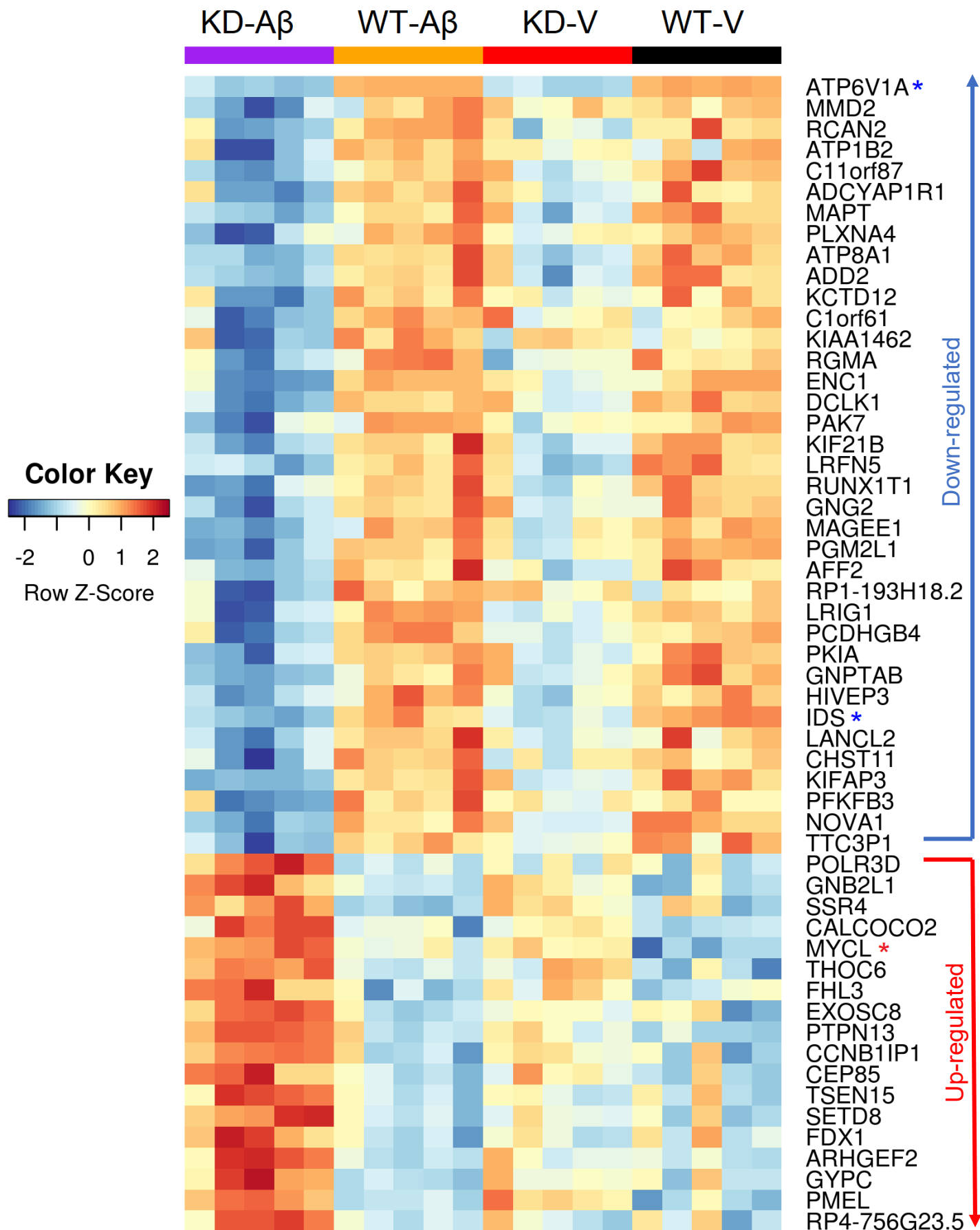


**Fig. S22. Heat-map showing genes significantly differentially expressed between *ATP6V1A* KD and WT in *NGN2*-neurons with or without A $\beta$  treatment, related to Figure 5.** The expression values have been converted to z-score. Blue and red asterisks (\*) denote, respectively, the genes consistently down- or up-regulated irrespective of A $\beta$  treatment (i.e. KD-V vs WT-V and KD-A $\beta$  vs WT-A $\beta$ ). Genes without any symbol annotation are detected only in A $\beta$  treated cells (i.e. KD-A $\beta$  vs WT-A $\beta$ ).

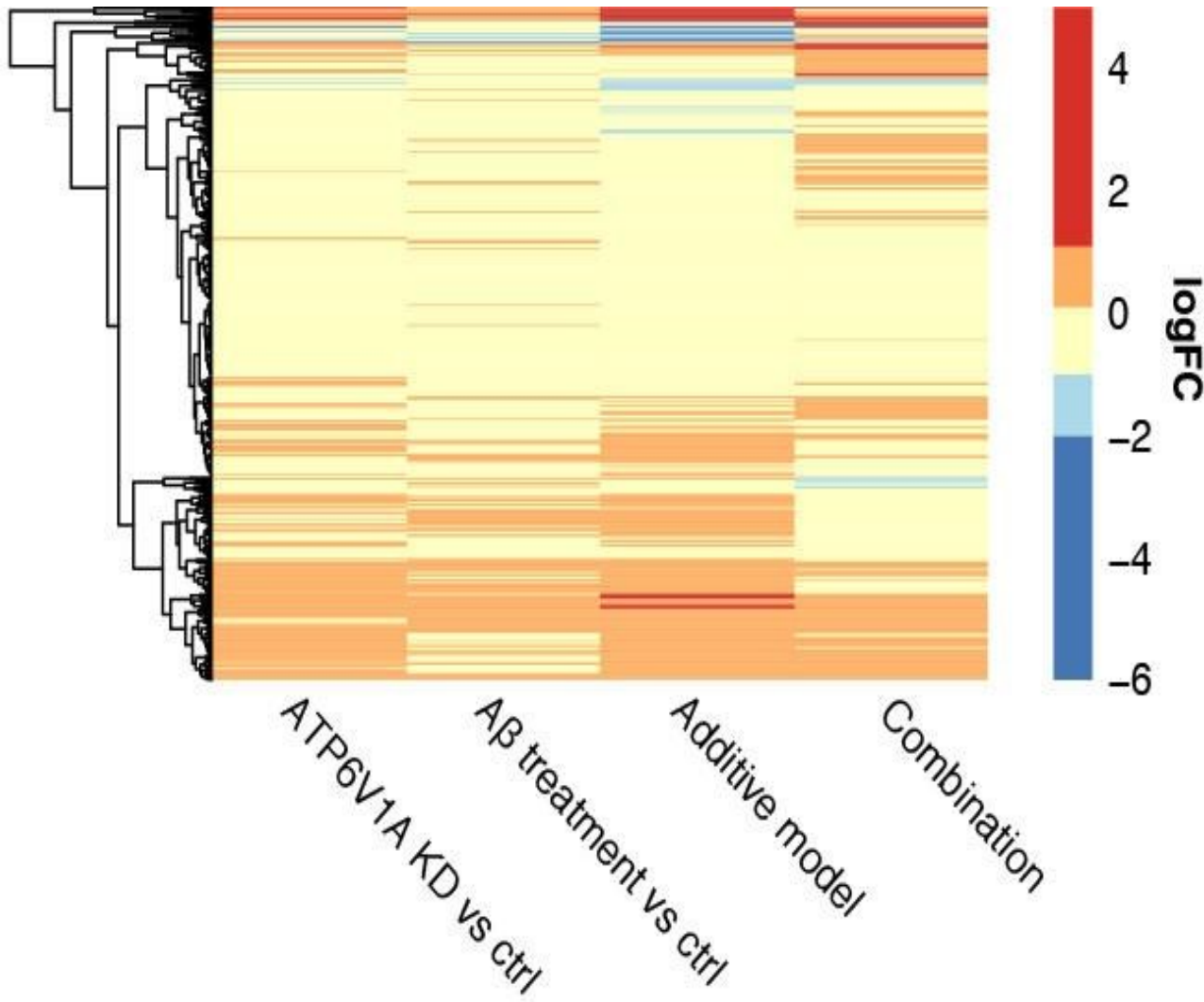


**Fig. S23. Hierarchical clustering of differential expression log2 fold changes (logFC) for all contrasts in NGN2-neurons treated with *ATP6V1A* KD and/or A $\beta$ , related to Figure 5.** Genes were pre-aggregated using k-means ( $k=500$ ). Color gradient represents logFC.

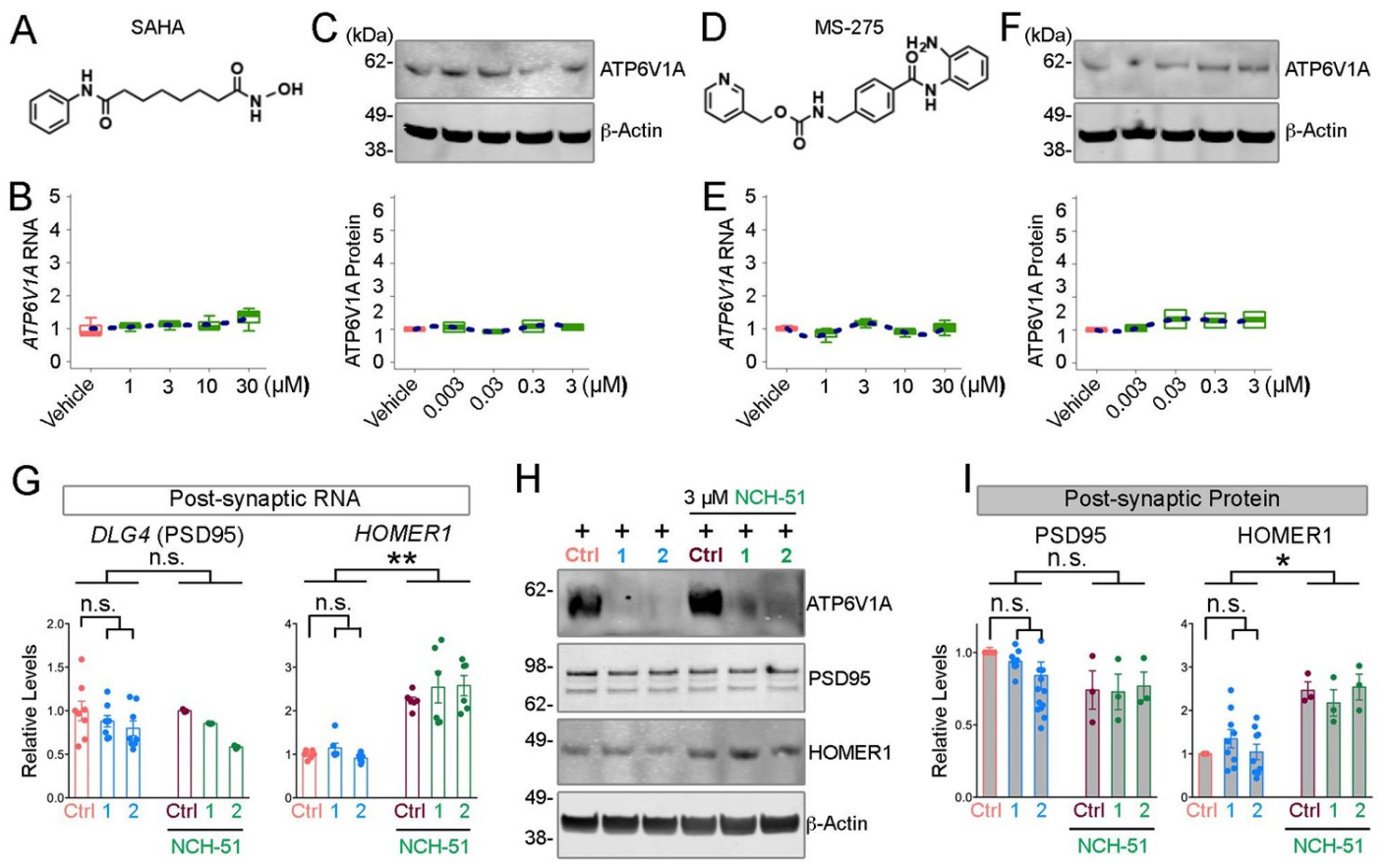
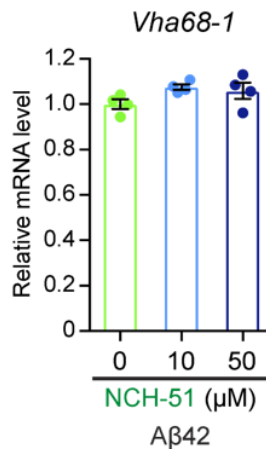
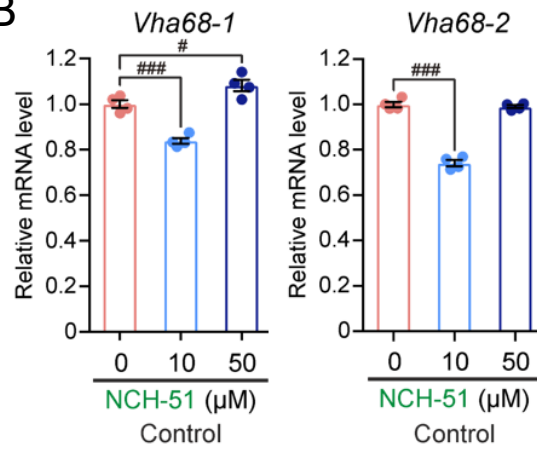


**Fig. S24. Effects of SAHA and MS-275 on *ATP6V1A* mRNA level and NCH-51 on postsynaptic expression in *NGN2*-neurons, related to Figure 6.** **A-F**, HDAC inhibitors SAHA and MS-275 have no effect on *ATP6V1A* levels. Chemical structures of SAHA (**A**) and MS-275 (**D**). Effects of SAHA (**B**) and MS-275 (**E**) at 1, 3, 10, 30  $\mu$ M on *ATP6V1A* mRNA levels 24-h after exposure. Effects of SAHA (**C**) and MS-275 (**F**) at 0.003, 0.03, 0.3, 3  $\mu$ M on *ATP6V1A* protein level 48-h after exposure, analyzed by western blot.  $\beta$ -Actin is a loading control. A blue dotted line is curve fitted for the set of data points. **G**, qRT-PCR analysis of *ATP6V1A* and the postsynaptic *PSD95* and *HOMER1* mRNA expression in *NGN2*-neurons in the absence and presence of 3  $\mu$ M NCH-51. n = 3-8 replicates. **H-I**, Representative western blot and quantitative analysis (n = 3-10 replicates) of *ATP6V1A*, *PSD95* and *HOMER1* protein.  $\beta$ -Actin is a loading control. ANOVA; \*p < 0.05; \*\*p < 0.01; \*\*\*p < 0.001; n.s., no significance; Error bars represent SE.

A



B



C

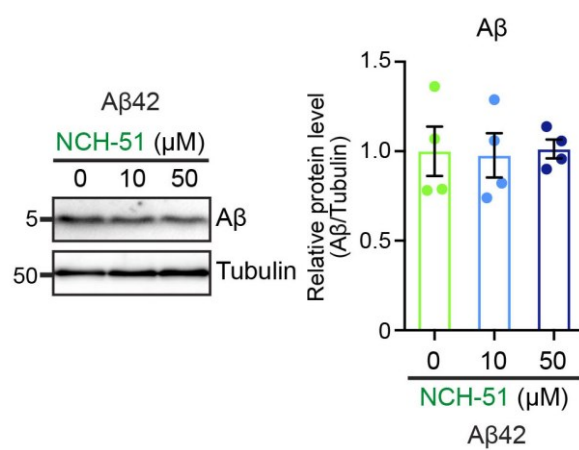


**Fig. S25. A novel compound, NCH-51 suppresses neurodegeneration in A $\beta$ 42 flies, related to Figure 6.** **A**, Administration of NCH-51 did not increase mRNA levels of *Vha68-1* in A $\beta$ 42 flies. **B**, mRNA levels of *Vha68-1* and *Vha68-2* in control flies fed with NCH-51 were analyzed by qRT-PCR. n = 4, #p < 0.05, ###p < 0.001 by one-way ANOVA with Dunnett's post hoc test. **C**, Administration of NCH-51 did not affect A $\beta$ 42 levels in fly brains. A $\beta$ 42 peptides from fly heads were analyzed by western blotting with anti-A $\beta$  antibody. n = 4. The genotypes of the flies were (A $\beta$ 42): *elav-GAL4/Y*; UAS-A $\beta$ 42 /+ and (Control): *elav-GAL4/Y*.

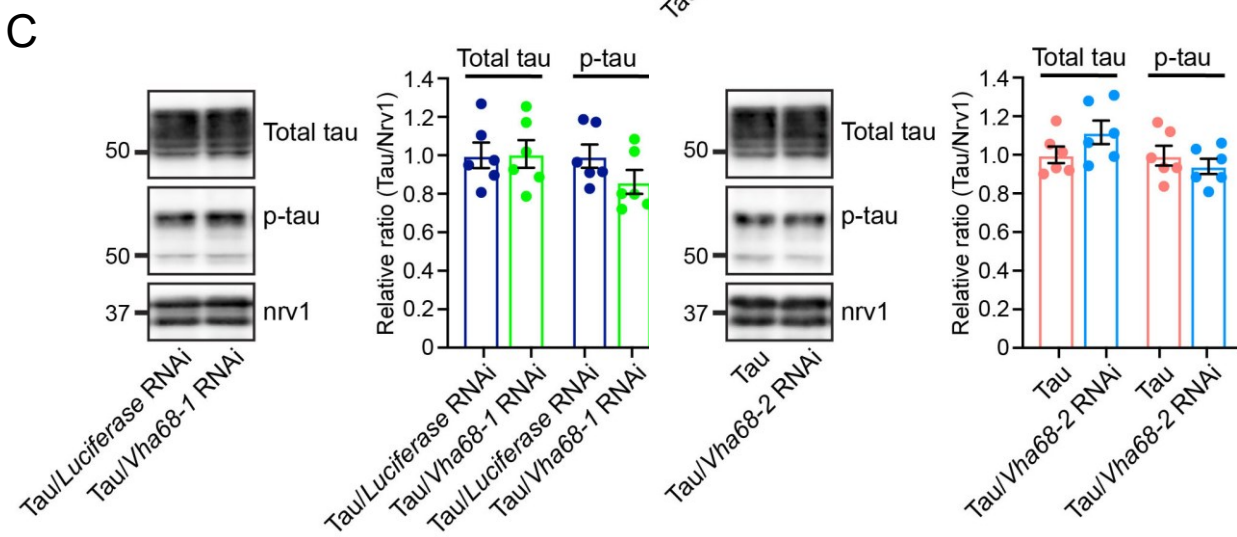
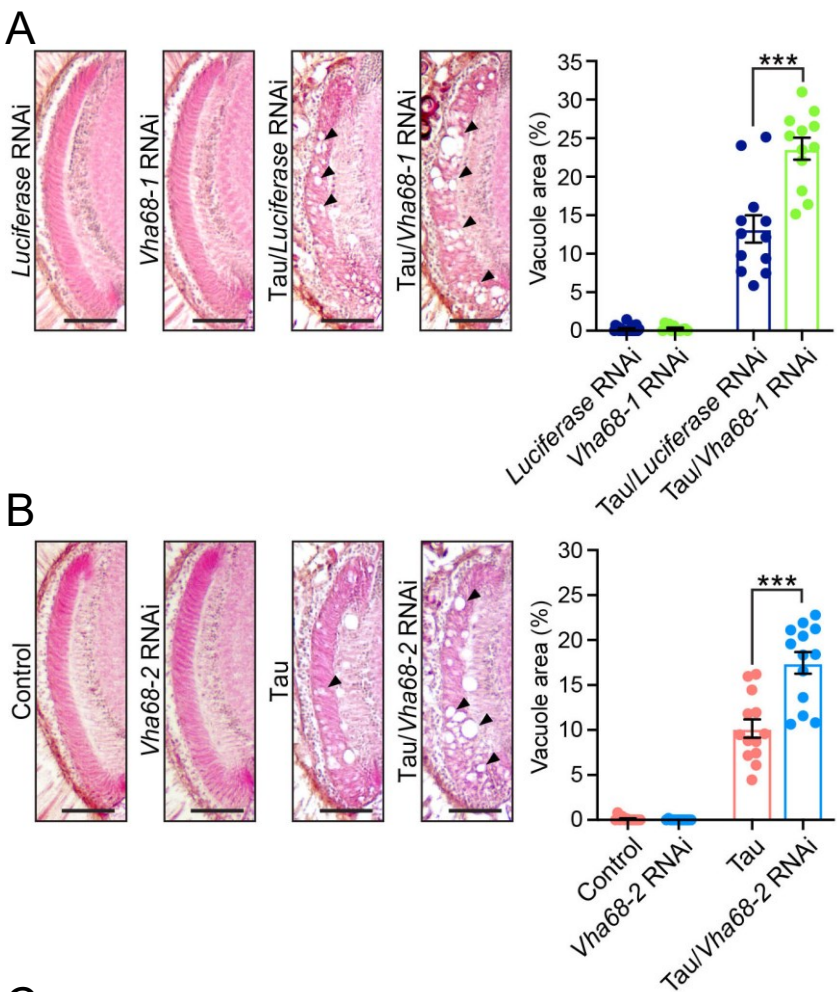


**Fig. S26. Knockdown of *Vha68-1* or *Vha68-2* exacerbates axon degeneration caused by overexpression of human tau, related to STAR Methods.** Knockdown of *Vha68-1* (A) or *Vha68-2* (B) in fly eyes exacerbated axon degeneration in the lamina caused by ectopic overexpression of human tau. Representative images show the lamina in paraffin-embedded head section with hematoxylin and eosin (HE) staining from 7-day-old flies. Scale bars: 50  $\mu$ m. Percentages of vacuole areas in the lamina (indicated by arrowheads in the images) are shown. n = 12 hemispheres, \*\*\*p < 0.001 by Student's t-test. (C) Knockdown of *Vha68-1* or *Vha68-2* did not alter either the total or phosphorylation levels of tau. Fly heads expressing tau alone (Tau) or co-expressing tau and RNAi targeting for *Vha68-1* or *Vha68-2* subjected to western blotting with anti-tau or anti-phospho tau (AT8, pS202/T205) antibodies. Nervana (nrn1), a fly ortholog of ATPase Na<sup>+</sup>/K<sup>+</sup> transporting subunit  $\beta$  1, was used as the loading control. n = 6. The genotypes of the flies were (*Luciferase RNAi*): +/Y; GMR-GAL4/UAS-*Luciferase RNAi*, (*Vha68-1 RNAi*): +/Y; GMR-GAL4/UAS-*Vha68-1 RNAi*, (*Tau/Luciferase RNAi*): +/Y; GMR-GAL4, UAS-tau/*Luciferase RNAi*, (*Tau/Vha68-1 RNAi*): +/Y; GMR-GAL4, UAS-tau/UAS-*Vha68-1 RNAi*, (Control): +/Y; GMR-GAL4/+, (*Vha68-2 RNAi*): +/Y; GMR-GAL4/++; UAS-*Vha68-2 RNAi*/+, (*Tau*): +/Y; GMR-GAL4, UAS-tau/+ and (*Tau/Vha68-2 RNAi*): +/Y; GMR-GAL4, UAS-tau/++; UAS-*Vha68-2 RNAi*/+.

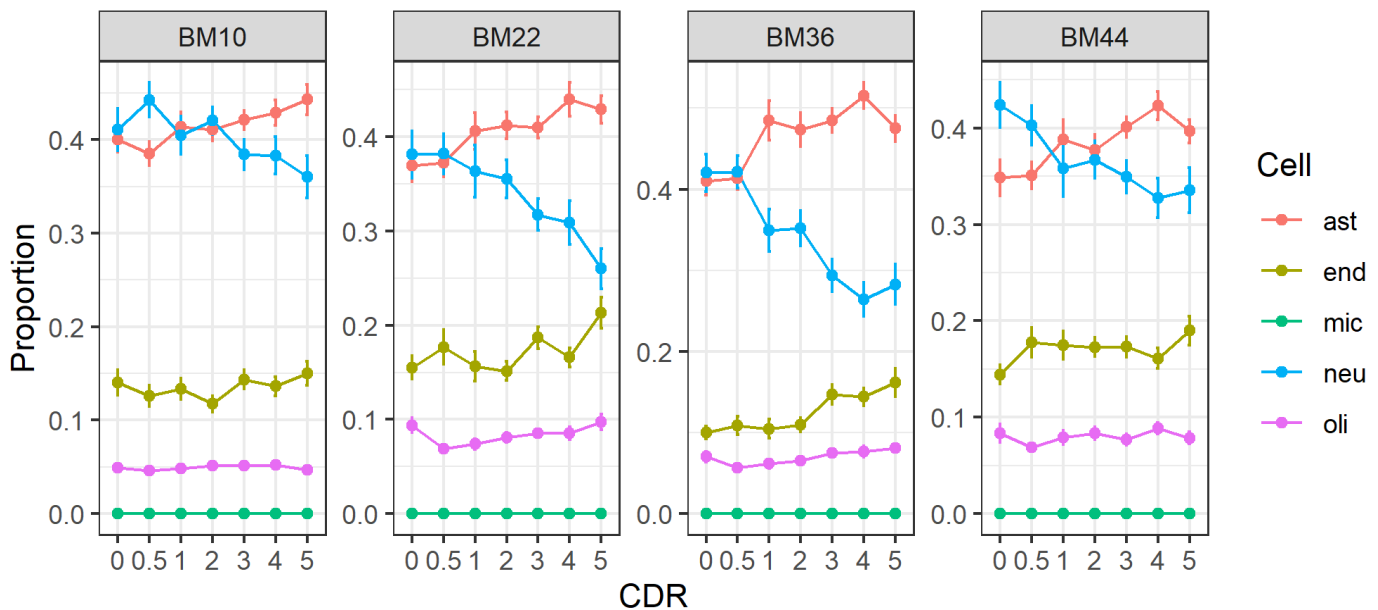


**Fig. S27. Distribution of cell type frequency estimates stratified by CDR, related to STAR Methods.** Error bar denotes standard error. Ast, astrocyte; end, endothelial; mic, microglia; neu, neurons; oli, oligodendrocytes. The proportion of microglia cells was not estimable, likely due to the low sensitivity in estimating cells with low abundance.